universität wien

DISSERTATION / DOCTORAL THESIS

Titel der Dissertation /Title of the Doctoral Thesis

„Versatile and robust Yb:fiber lasers for single and dual-comb applications“

verfasst von / submitted by

Dipl.-Ing. Jakob Fellinger, BSc

angestrebter akademischer Grad / in partial fulfilment of the requirements for the degree of

Doktor der Naturwissenschaften (Dr. rer. nat.)

Wien, 2020 / Vienna 2020

Studienkennzahl lt. Studienblatt / degree programme code as it appears on the student record sheet:	A 796 605 411
Dissertationsgebiet lt. Studienblatt / field of study as it appears on the student record sheet:	Physik
Betreut von / Supervisor:	Ass.-Prof. Dipl.-Phys. Dr. Oliver H. Heckl

Versatile and robust Yb:fiber lasers for single and dual-comb applications

DOCTORAL THESIS

Jakob Fellinger

Christian Doppler Laboratory for Mid-IR Spectroscopy and Semiconductor Optics, Faculty Center for Nano Structure Research, Faculty of Physics, University of Vienna, 1090 Vienna, Austria

supervised by Ass.-Prof. Dipl.-Phys. Dr. Oliver H. Heckl

Preface

This thesis is written as a cumulative dissertation and **is based on the following publications:**

[1] **J. Fellinger**, G. Winkler, A. S. Mayer, L. R. Steidle, and O. H. Heckl, "Tunable dual-color operation of Yb:fiber laser via mechanical spectral subdivision," Opt. Express, vol. 27, no. 4, pp. 5478-5486, 2019.

[2] A. S. Mayer, W. Grosinger, **J. Fellinger**, G. Winkler, L. W. Perner, S. Droste, S. H. Salman, C. Li, C. M. Heyl, I. Hartl, and O. H. Heckl, "Flexible all-PM NALM Yb:fiber laser design for frequency comb applications: operation regimes and their noise properties,"Opt. Express, vol. 28, no. 13, pp. 18946-18968, 2020.

[3] **J. Fellinger**, A. S. Mayer, G. Winkler, W. Grosinger, G.-W. Truong, S. Droste, C. Li, C. M. Heyl, I. Hartl, and O. H. Heckl, "Tunable dual-comb from an all-polarization-maintaining single-cavity dual-color Yb:fiber laser," Opt. Express, vol. 27, no. 20, pp. 28062-28074, 2019.

The thesis is structured as follows:

- In Chapter 1, I discuss the motivation behind the experiments presented in this thesis and summarize the basic theoretical concepts necessary to understand the field of mode-locked fiber lasers and frequency combs.
- In Chapters 2, 3 and 4, the publications that emerged during the time of my Ph.D. studies are reprinted. Each chapter starts with a short preface explaining the context in which these experiments were performed. Additionally, I provide supplementary material that was not published in the papers.
- In Chapter 5, I summarize the results, discuss the present work from an overall perspective and give an outlook on further research questions and possible experimental setups to answer those questions.

Abstract

Optical frequency combs, which were originally invented as a high-precision measuring instrument for optical frequencies, have recently also become an indispensable part of optical spectroscopy. However, stepping from the laboratory into field applications represents a major challenge. The highly sensitive light sources used for frequency comb spectroscopy usually react dramatically to real environmental influences such as vibrations or temperature fluctuations.

This thesis describes the generation of robust optical frequency combs based on all-polarization maintaining (PM) fiber lasers and how to optimize them for stability and noise performance. We present the development of an all-PM Ytterbium-doped fiber laser mode-locked using a nonlinear amplifying loop mirror (NALM) in reflection, combined with an nonreciprocal phase bias - also called "figure-9" laser. The use of PM fibers offers higher stability and robustness against environmental perturbations; hence this laser type is a promising candidate for field applications. In very recent years, several different implementations of figure-9 lasers have been reported. However, a detailed analysis of the noise performance and how to operate the laser to obtain the lowest free-running noise has been pending. In order to close this gap, we have developed a particularly versatile figure-9 laser version, that allowed us to characterize the noise behavior as a function of different mode-locking regimes. We give a detailed description of how to optimize the laser in terms of intensity noise and timing jitter as well as how to obtain a narrow linewidth of the free-running comb offset frequency. The laser setup presented here offers a free-running comb offset linewidth of 9.75 kHz at 1 s integration time, which is, to the best of our knowledge, the narrowest linewidth reported so far for this laser type.

As a second topic, we present a novel method to generate two frequency combs out of a single laser cavity with the goal to perform so-called dual-comb spectroscopy - a spectroscopy technique that combines broad spectral coverage and fast acquisition times and shows particular promise for applications outside of the laboratory environment. The novel method presented here consists of implementing a flexible mechanical spectral filter inside the laser, enabling the generation of two pulse trains with slightly different colors and repetition rates out of one single fiber laser. This flexible approach holds two key advantages: the possibility to tune the difference in repetition rates as well as the spectral separation of the two pulse trains.

By merging the stability and robustness of the figure-9 laser design with the tunable mechanical spectral filtering method, we realized an all-PM single-cavity dual-color laser whose functionality is demonstrated in a first proof-of-principle dual-comb experiment.

Kurzfassung

Optische Frequenzkämme, die ursprünglich als hochpräzises Messinstrument für optische Frequenzen erfunden wurden, sind seit kurzem auch ein unverzichtbarer Bestandteil der optischen Spektroskopie. Der Schritt vom Labor hin zu Feldanwendungen stellt jedoch eine große Herausforderung dar. Die für die Frequenzkammspektroskopie verwendeten hochempfindlichen Lichtquellen reagieren normalerweise dramatisch auf reale Umwelteinflüsse wie Vibrationen oder Temperaturschwankungen.

Diese Arbeit beschreibt die Erzeugung robuster optischer Frequenzkämme auf der Basis polarisationerhaltender Faserlaser und deren Optimierung hinsichtlich Stabilität und Rauschverhalten. Wir präsentieren die Entwicklung eines polarisationserhaltenden Ytterbium-dotierten Faserlasers, modengekoppelt unter Verwendung eines nichtlinearen Verstärkungsschleifenspiegels in Reflexion in Kombination mit einem nichtreziproken Phasenschub - auch bekannt als "figure-9"Laser. Die Verwendung polarisationserhaltender Fasern bietet eine höhere Stabilität und Robustheit gegenüber Umweltstörungen. Daher ist dieser Lasertyp ein vielversprechender Kandidat für Feldanwendungen. In den letzten Jahren wurden verschiedene Implementierungen von figure-9 Lasern präsentiert. Eine detaillierte Analyse des Rauschverhaltens und sowie der Betriebsbedingungen des Lasers, die das niedrigste passive Rauschen hervorrufen, stand bisher jedoch noch aus. Um diese Lücke zu schließen, haben wir eine besonders vielseitige Version eines figure-9 Lasers entwickelt, mit der wir das Rauschverhalten als Funktion verschiedener Modenkopplungsregime charakterisieren können. Wir beschreiben im Detail, wie der Laser hinsichtlich Intensitäts- und Phasenrauschen optimiert werden kann und wie eine enge Linienbreite der freilaufenden Kammversatzfrequenz erhalten werden kann. Der hier vorgestellte Laseraufbau bietet eine freilaufende Kammversatzlinienbreite von 9,75 kHz bei 1 s Integrationszeit, was nach unserem besten Wissen die engste Linienbreite ist, die bisher für diesen Lasertyp angegeben wurde.

Als zweites Thema stellen wir eine neuartige Methode zur Erzeugung zweier Frequenzkämmen aus einem einzigen Laserresonator vor, mit dem Ziel, sogenannte Doppelkammspektroskopie durchzuführen - eine Spektroskopietechnik, die eine breite spektrale Abdeckung und schnelle Messzeiten kombiniert und daher für Anwendungen außerhalb der Laborumgebung besonders vielversprechend ist. Das hier vorgestellte neuartige Verfahren besteht darin, einen flexiblen mechanischen Spektralfilter im Laser zu implementieren, der die Erzeugung von zwei Pulszügen

mit leicht unterschiedlichen Farben und Wiederholungsraten aus einem einzelnen Faserlaser ermöglicht. Dieser flexible Ansatz bietet zwei wesentliche Vorteile: die Möglichkeit, den Unterschied in den Wiederholungsraten sowie die spektrale Trennung der beiden Pulszüge abzustimmen.

Durch das Kombinieren der Stabilität und Robustheit des figure-9 Laserdesigns mit der durchstimmbaren mechanischen Spektralfiltermethode wurde ein polarisationserhaltender Zweifarbenlaser mit einem einzigen Laserresonator realisiert, dessen Funktionalität in einem ersten Doppelkammversuch zum Nachweis des Prinzips demonstriert wurde.

Contents

Chapter 1

Introduction

"That is what I do. I drink, and I know things"

Tyrion Lannister, Game of Thrones

1.1 Motivation

Since the invention of optical frequency combs (OFCs) [4, 5], OFCs have become an integral tool for various fields of research. Developed initially for counting the cycles of optical atomic clocks, they became an indispensable light source for optical spectroscopic applications [6]. Due to their broad spectral coverage and high brightness, OFCs offer enormous potential for atom and molecule detection [7].

Our society's rapid development confronts us with new challenges in areas such as environmental science and health care. The improvement of state-of-the-art spectroscopy will give us new tools for environmental monitoring and trace gas analysis in order to face these new challenges. All components of spectroscopic experiments have to meet the highest demands to analyze complex gas mixtures to detect and identify pollutants in the air or bio-markers in breath gas.

In particular for measurements that involve complex gas mixtures with an unknown composition, the measurement technique needs to provide both a large spectral coverage, high brightness of the light source, as well as a high resolution. Since OFCs have a spectral structure that consists of a multitude of equally spaced narrow laser lines, they are particularly suited to fulfill these requirements.

Ultimately, the spectral resolution that can be achieved in spectroscopic experiments will be limited by the stability of the OFC. Developing ultra-stable OFCs is an ongoing challenge. A significant limitation for most state-of-the-art high-precision OFCs is that they require a temperature-stabilized and vibration-isolated environment. Such an environment is usually only available in high-end optical laboratories.

One of the most promising approaches to overcome these difficulties is to build frequency combs based on mode-locked (pulsed) fiber lasers. Due to their robustness, fiber lasers offer enormous potential for spectroscopy outside the labo-

ratory [8]. Nowadays, fiber lasers have already been sent to space and operated under microgravity [9].

This thesis is a contribution to the ongoing effort of developing and analyzing a specific fiber laser design that shows particularly promising performance regarding its robustness and stability - the so-called "figure-9" laser design.

Beyond the stability of the light source, the resolution of the detection assembly is another limiting factor. Various methods to resolve optical spectra have been reported [10–14]. For most of the reported spectral measurement methods, a compromise must be made between acquisition time, resolution, and spectral coverage. One versatile method is dual-comb (DC) spectroscopy [15]. DC spectroscopy enables fast data acquisition over broadband spectra with high resolution. An additional advantage is that there is no need for any complex spectrometer assembly; a simple photodiode is sufficient to measure the spectrum. The drawback of DC spectroscopy is that it requires a complex light source: dual-comb spectroscopy is based on two OFCs. The two lasers must be stabilized to each other to obtain mutual coherence between the two combs, which can quickly become a complex and difficult task.

A promising simplification is the so-called single-cavity dual-comb [16]. Instead of using two independent OFCs, a single laser resonator is manipulated to emit two OFCs. Since the two combs emerge from the same cavity, they can be mutually coherent without any active stabilization. The intrinsic stability of single-cavity dual-comb offers enormous potential for spectroscopic applications [17–19]. In this thesis, a novel method to generate a single-cavity a dual-color laser via a tunable mechanical spectral filter is introduced and the method is shown to be compatible with the robust figure-9 laser design.

In the following theoretical introduction, the fundamentals of OFCs are outlined. Starting from light-matter interaction, I present the most important aspects of light propagation inside a fiber laser cavity and how they can be exploited for the generation of ultrashort pulses, i.e., for mode-locking. Moreover, I explain how mode-locked lasers are related to frequency combs. Finally, an overview of the dual-comb principle is presented. This introduction covers the most basic concepts that are necessary to understand the publications presented in chapter 2-4.

1.2 Light-matter interactions

The interaction of light with dielectric materials is the basis for most of the work presented in this thesis.

The wave equation for electromagnetic waves can be used to describe the re-

sponse of dielectric materials to an optical wave. The wave equation inside a dielectric material can be derived form the Maxwell equations and (using the Einstein sum convention) is given by

$$\partial^j \partial^i E^i - \frac{1}{c^2} \partial_t^2 E^j = \mu_0 \partial_t^2 P^j, \tag{1.1}$$

where E^i is the electric field, P^j is the dielectric polarization density, c is the speed of light in vacuum and μ_0 is the vacuum permeability. The polarization density P^j can be expressed as a power series using the corresponding electric susceptibility tensor χ, i.e.

$$P^j = \varepsilon_0 (\chi_{(1)}^{jk} E^k + \chi_{(2)}^{jkl} E^k E^l + \chi_{(3)}^{jklm} E^k E^l E^m + ...), \tag{1.2}$$

where ε_0 is the vacuum permittivity.

1.2.1 Linear optics

The linear response of a material to an electric field is described by the complex refractive index $\underline{n}$ where

$$\underline{n}^2 = 1 + \chi_{(1)}. \tag{1.3}$$

The imaginary part of $\underline{n}$ corresponds to the absorption inside the medium while the real part is the refractive index $n = c/c_m$, where c is the speed of light in vacuum and c_m is the speed of light in the material. The refractive index n is frequency dependent. The frequency dependence of n is called chromatic dispersion.

Chromatic dispersion causes light waves of different frequencies to propagate through a dielectric medium at different velocities. The wavelength-dependent refractive index can be calculated by using the Sellmeier equation. The Sellmeier equation is an empirically developed formula based on the Kramers-Kronig-relation [20]. Our lasers are operating at a wavelength around 1 µm. In this wavelength region, the most common material for optical fibers is fused silica. The Sellmeier equation for the wavelength-dependent refractive index of fused silica is given by [21]:

$$n(\lambda) = \sqrt{\frac{0.6961663\lambda^2}{\lambda^2 - 0.0684043^2} + \frac{0.4079426\lambda^2}{\lambda^2 - 0.1162414^2} + \frac{0.8974794\lambda^2}{\lambda^2 - 9.896161^2} + 1} \tag{1.4}$$

The function of Eqn. 1.4 is plotted in Fig 1.1.

Most optical fibers are made of glasses (such as fused silica), and thus have an amorphous material structure. Hence, for a symmetric fiber core structure the refractive index of a standard fiber does not depend on the direction of the field

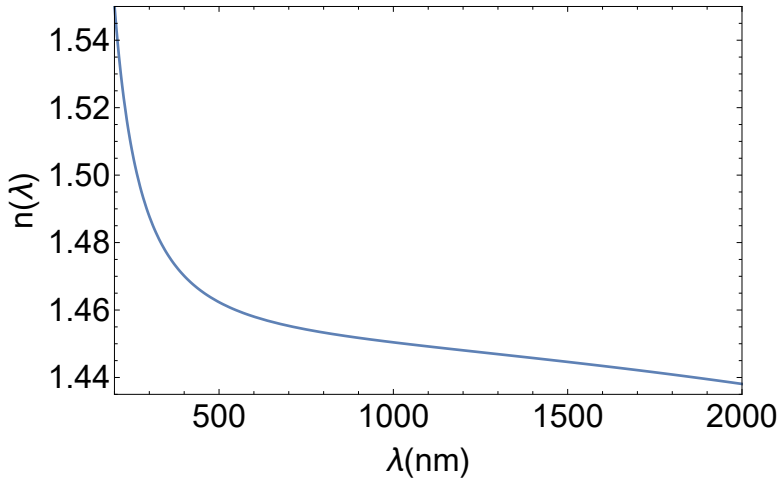

Figure 1.1 – Wavelength-dependent refractive index of fused silica calculated using Eqn. 1.4.

oscillations (called the "polarization") of the light field. However, for anisotropic crystalline materials, the refractive index is different along the different crystal axes and will thus depend on the polarization of the light; this effect is called birefringence [22].

Polarization optics

Birefringence can be exploited to manipulate the polarization of light using so-called wave plates or to preserve the polarization state inside so-called polarization-maintaining optical fibers. In order to understand the working principle of the lasers presented in this thesis, it is essential to be familiar with the concept of wave plates and polarization-maintaining fibers.

wave plates [23]: Transmissive optical elements which are commonly used to manipulate the polarization state of a laser beam. They feature a so-called fast axis, along which light propagates with a faster phase velocity than along the perpendicular slow axis. Both axes are furthermore perpendicular to the beam direction. Due to the different phase velocity for the different axes, wave plates can be exploited to generate a phase shift between the light polarization components propagating along the different axes. This phase shift can be calculated as

$$\Delta\phi = \frac{2\pi}{\lambda} d(n_{\text{slow}} - n_{\text{fast}}), \tag{1.5}$$

where λ is the wavelength of the light, d is the thickness of the plate and n_{slow} and n_{fast} are the refractive indices of the slow and the fast axis respectively.

If the thickness is chosen such that $\Delta\phi = \pi/2$ for the desired wavelength, the wave plate is termed "half-wave plate", while for $\Delta\phi = \pi/4$, it is called a "quarter-wave plate".

polarization-maintaining (PM) fiber [24]: Optical glass fibers with a symmetric core are in principle isotropic. However, mechanical stress such as torsion or bending can induce birefringence in the fiber. This can cause random phase shifts and thus scrambling of the polarization of the light propagating inside the fiber. However, by introducing a large amount of intended birefringence between two perpendicular axes inside the optical fiber (e.g. by introducing so-called "stress rods" on either side of the core), this effect can be controlled. Due to the intended birefringence, light propagating along the different axes have different phase velocities. The axis with the faster velocity is called the fast axis while the axis perpendicular to it is called the slow axis. In such a fiber, coupling of light between the fast and the slow axis is suppressed. Hence, if linearly polarized light is coupled into the fiber with the polarization being parallel either to the fast or the slow axis, the light will still exit the fiber perfectly linearly polarized even if the fiber is subjected to environmental perturbations.

1.2.2 Nonlinear optics

Considering the higher-order terms of the power series in Eq.1.2, different nonlinear effects can be derived. Nonlinear effects can be exploited to generate coherent radiation with a different frequency than the excitation wave; hence, nonlinear effects can be used for frequency conversion. In the following, I will give a short overview of the most important nonlinear effects. Please note that the following list is certainly not exhaustive, but rather focuses on the effects relevant for this thesis.

Second-order nonlinear effects

Second-order nonlinear effects are based on $\chi_{(2)}$-nonlinearities, which occur in media that lack inversion symmetry on the molecular level [25]. The following effects are based on $\chi_{(2)}$-nonlinearities:

Second harmonic generation is also called frequency doubling; it can be understood as a process where two pump photons with frequency ω_1 are virtually absorbed and one signal photon is generated with twice the frequency of the pump photon, i.e. $\omega_2 = 2\omega_1$, see Fig 1.2(a). In the experiments presented

in this thesis, second-harmonic generation is used for example to frequency-double light for f-to-$2f$ interferometry as will be described in chapter 3.

Sum frequency generation is quite similar to second harmonic generation; the only difference is that instead of two photons of a single pump wave, one photon of a pump wave with frequency ω_1 and one photon of a second pump wave with frequency ω_2 is virtually absorbed to generate light with the frequency $\omega_3 = \omega_1 + \omega_2$, see Fig 1.2(b).

Difference frequency generation/optical parametric amplification can be understood as a kind of a virtual lasing process. Pump light with the frequency ω_1 is virtually absorbed into a pump level. From the pump level, it decays into a lower energy level, emitting a photon with the energy $\omega_3 = \omega_1 - \omega_2$. From this level, it is decaying into the ground state, emitting light with ω_2 and thus amplifying the initial seed light with ω_2, see Fig. 1.2(c).

Optical parametric oscillation is based on parametric amplification in a nonlinear crystal in combination with resonant feedback. The crystal is pumped with a seed laser (ω_1). The pump beam is depleted in the crystal, generating a signal (ω_2) and an idler beam (ω_3) corresponding to the phase-matching conditions of the crystal. Either the idler or the signal or both are resonantly fed back to enhance the conversion process, see Fig 1.2(d).

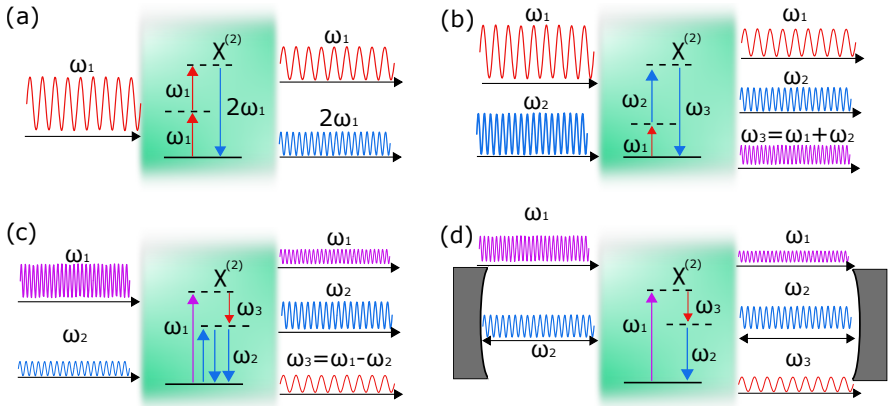

Figure 1.2 – Different second order nonlinear effects. (a) Frequency doubling, (b) sum frequency generation, (c) difference frequency generation respectively parametric amplification, and (d) the principle of an optical parametric oscillator.

Phase matching

Energy conservation determines which frequencies can be generated exploiting the parametric nonlinear effects introduced above. However, in order to achieve a significant energy transfer from one wave to another, momentum conservation also needs to be taken into account, which results in the phase-matching condition [26]: the wave vectors of input waves k_{input} triggering the nonlinear process must match the wave vectors of the output light k_{output} generated by the process. Phase matching is essential to get constructive interference of the light generated by the nonlinear process inside the nonlinear medium. The most efficient energy transfer occurs if the wave vector mismatch Δk [27] is zero. For collinear beams, this condition can be expressed as:

$$\Delta k = \sum_{n=1}^{N} k_{\text{input,n}} - \sum_{m=1}^{M} k_{\text{output,m}} = 0. \tag{1.6}$$

Second-order effects are important for wavelength conversion and are often used in laser diagnostics setups. However, they usually do not occur in optical fibers, since the latter consist of amorphous materials, where the $\chi_{(2)}$-response vanishes. The most dominant effects inside optical fibers are caused by third-order nonlinearities.

Third-order nonlinear effects

Third-order nonlinear effects are based on $\chi_{(3)}$-nonlinearities. These third-order effects are caused by different processes on the molecular and electronic level, which have different response times [27]. Parametric processes like the Kerr effect and four-wave mixing have a nearly instantaneous response, while Raman scattering has a delayed response.

The Kerr effect is a third-order nonlinear effect and leads to an intensity-(I)-dependent refractive index of the material

$$n(I) = n_1 + n_2 I, \tag{1.7}$$

where n_1 is the linear and n_2 the nonlinear refractive index

$$n_2 = \frac{3}{4\varepsilon_0 c n_1^2} \text{Re}(\chi_{(3)}) \tag{1.8}$$

The Kerr effect, in turn, can cause several different processes that are particularly relevant when working with pulsed lasers:

- **self-phase modulation (SPM)** Due to the time-dependent intensity profile of a laser pulse, the Kerr effect causes a time-dependent refractive index. This variation of the refractive index causes a phase delay. Since the laser intensity causes this phase delay, it is a nonlinear phase delay, i.e., a time-varying phase. A time-varying phase is nothing else than a new frequency. Therefore SPM can be exploited to generate new optical frequencies.
- **Kerr lensing** If we consider a laser beam with a certain transverse intensity profile, the Kerr effect will lead to a refractive index that varies across this intensity profile. The variation of the refractive index across the transverse mode profile is causing the same effect as a lens. The laser beam will be self-focused. Self-focusing is one of the major damaging processes caused by high-intensity light inside optical materials, especially inside optical waveguides.
- **cross-phase modulation (XPM)** is a special case of the Kerr effect, where two electric fields propagate inside a nonlinear medium and influence each other. The refractive index for one electric field now depends on the intensity of both fields

$$n^{p1}(I_1, I_2) = n_1^{p1} + n_2^{p1} I_1 + n_2^{p1} I_2, \text{ and } n^{p2}(I_1, I_2) = n_1^{p2} + n_2^{p2} I_1 + n_2^{p2} I_2 \tag{1.9}$$

- **four-wave mixing** is an additional parametric process. Let us consider two optical waves with frequency ω_1 and ω_2 ($\omega_1 > \omega_2$) propagating inside a medium with third-order nonlinearities. Due to the optical beating of the two waves, they will cause an intensity fluctuation with the difference frequency of $\omega_1 - \omega_2$. The refractive index modulation causes the generation of two new frequencies: $\omega_3 = \omega_2 - (\omega_1 - \omega_2)$ and $\omega_4 = \omega_1 + (\omega_1 - \omega_2)$.

Raman scattering Raman scattering is caused by the inelastic scattering of photons inside the nonlinear medium. Inelastic scattering means that a part of the photon energy excites optical phonons inside the nonlinear material. The inelastic scattering process generates photons with lower frequencies (longer wavelengths) than the original light.

The nonlinear effects presented in this section can be derived from the power series of the dielectric polarization density. For linear optics, the higher-order terms are neglected. However, for high intensities, this approximation is not appropriate anymore.

Let us consider a pulsed laser with a pulse repetition rate f_{rep} of 100 MHz, a pulse duration t_{p} given as full width at half maximum (FWHM) of 100 fs and an average output power P_{average} of 1 W. This gives us a pulse energy E_{p} of

$$E_{\mathrm{p}} = \frac{P_{\mathrm{average}}}{f_{\mathrm{rep}}}, \tag{1.10}$$

which amounts to ≈10 nJ given the values above. The energy is compressed to a time interval given by the pulse duration (100 fs in this example). Thus, the peak power P_{peak} of the laser pulse can be calculated as

$$P_{\mathrm{peak}} = g\frac{E_{\mathrm{p}}}{t_{\mathrm{p}}}, \tag{1.11}$$

where g is a form factor depending on the temporal shape of the pulse. For a Gaussian-shaped pulse ($g \approx 0.94.$), we get a peak power P_{peak} of 100 kW in our example. In conclusion, the peak power achieved with ultrashort pulses is 10^5 times stronger than for a continuous-wave (CW) laser featuring the same average power of 1 W. For such peak powers, nonlinear effects can no longer be neglected. Hence, third-order nonlinear effects have a significant influence both on the generation as well as the propagation of ultrashort pulses.

1.3 Pulsed lasers and their dynamics

Let us consider a single laser pulse, see Fig. 1.3(a). For this pulse, the time-dependent electric field $E(t)$ at a fixed position on the propagation axis z (for example at $z = 0$) can be written as the integral of an amplitude distribution $\tilde{A}(\omega)$, shown in Fig 1.3(b), over an infinite number of frequencies ω:

$$E(t) = \frac{1}{2\pi}\int_{-\infty}^{\infty} \tilde{E}(\omega)e^{i\omega t}\mathrm{d}\omega. \tag{1.12}$$

Since we integrate with infinite decimal steps $\Delta\omega$ around the center frequency ω_{c} of the amplitude distribution and $\omega_{\mathrm{c}} >> \Delta\omega$, we can substitute ω with $\omega_{\mathrm{c}} + \Delta\omega$. With this substitution Eqn. 1.12 can be rewritten as

$$E(t) = \frac{1}{2\pi}\int_{-\infty}^{\infty} \tilde{E}(\omega_{\mathrm{c}} + \Delta\omega)e^{i(\omega_{\mathrm{c}}+\Delta\omega)t}\mathrm{d}\Delta\omega = e^{i\omega_{\mathrm{c}}t}\frac{1}{2\pi}\int_{-\infty}^{\infty} \tilde{a}(\Delta\omega)e^{i\Delta\omega t}\mathrm{d}\Delta\omega, \tag{1.13}$$

with the spectral pulse shape $\tilde{a}(\Delta\omega) = \tilde{E}(\omega_{\mathrm{c}}+\Delta\omega)$. The inverse Fourier transform of $\tilde{a}(\Delta\omega)$ corresponds to the pulse envelope $a(t)$ in the time domain, i.e.

$$a(t) = \frac{1}{2\pi}\int_{-\infty}^{\infty} \tilde{a}(\Delta\omega)e^{i\Delta\omega t}\mathrm{d}\Delta\omega. \tag{1.14}$$

The electric field in the time domain can thus be expressed as

$$E(t) = a(t)e^{i\omega_c t}, \tag{1.15}$$

where the center frequency ω_c is also called the "carrier frequency" of the pulse.

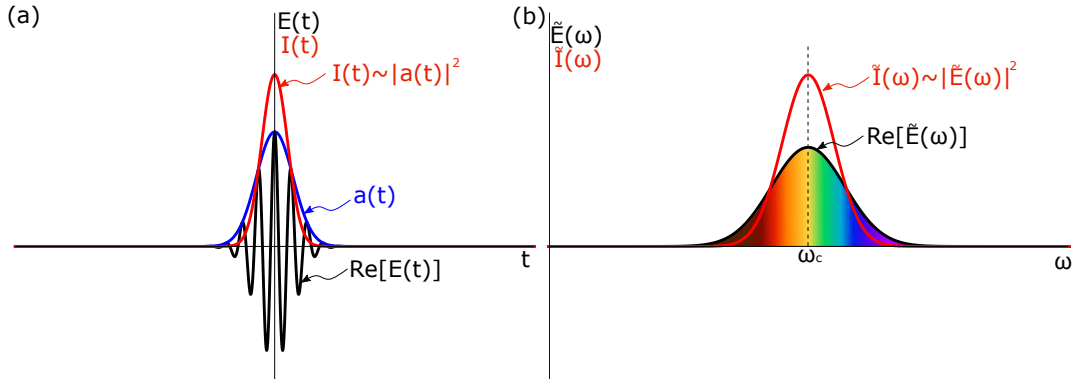

Figure 1.3 – Single optical pulse. (a) Time trace: the electric field underneath the envelope $a(t)$ oscillates with the carrier frequency ω_c. (b) Optical spectrum: the spectrum is given by an infinite number of frequencies with an envelope function.

In the following, I will give a short introduction to ultrashort pulse propagation and how different linear and nonlinear effects act on an ultra-short laser pulse.

1.3.1 Linear effects: dispersion

Dispersion is a linear effect; however, it has a strong influence on ultra-short optical pulses. The influence of dispersion on a pulse is easiest to calculate in the frequency domain, since the resulting field $\tilde{E}_{\text{out}}(\omega)$ can be obtained by simply multiplying the incoming electric field $\tilde{E}_{\text{in}}(\omega)$ with the transfer function $\tilde{h}(\omega)$, i.e.

$$\tilde{E}_{\text{out}}(\omega) = \tilde{h}(\omega)\tilde{E}_{\text{in}}(\omega), \tag{1.16}$$

where $\tilde{h}(\omega)$ originates form the solution of the Helmholtz-equation and is given by the frequency-dependent wave number k_{n} and the length of the dispersive medium L_{d}:

$$\tilde{h}(\omega) = e^{-ik_{\text{n}}(\omega)L_{\text{d}}} = e^{-i\phi(\omega)}, \tag{1.17}$$

The influence of this spectral phase shift $\phi(\omega) = k_{\text{n}}(\omega)L_{\text{d}}$ on the electric field $E(t)$ in the time domain can be calculated by Fourier transforming $E(t)$ to the frequency domain; applying the phase shift and subsequently Fourier transform the phase-shifted spectral field back to the time domain.

Since even for ultra-short light pulses, the spectral width $\Delta\omega$ of the laser pulse is orders of magnitudes smaller than the carrier frequency, it is common to Taylor-expand the change in spectral phase around the carrier frequency ω_c [28]:

$$\phi(\omega) = \phi_0 + \underbrace{\frac{\partial\phi(\omega)}{\partial\omega}}_{\phi_1}(\omega-\omega_c) + \frac{1}{2}\underbrace{\frac{\partial^2\phi(\omega)}{\partial\omega^2}}_{\phi_2}(\omega-\omega_c)^2 + \frac{1}{6}\underbrace{\frac{\partial^3\phi(\omega)}{\partial\omega^3}}_{\phi_3}(\omega-\omega_c)^3 + ... \quad (1.18)$$

In the following, the effect of the different orders of dispersion resulting from Eq.1.18 have been numerically calculated using a Gaussian pulse as an example. The initial pulse without any spectral phase can be seen in Fig. 1.4(a). The influence of ϕ_i on the pulse is the following:

$\boldsymbol{\phi_0}$: is a constant phase applied to the spectrum, in the time domain it leads to a phase shift of the carrier frequency, see Fig. 1.4(b).

$\boldsymbol{\phi_1}$: is called group delay or T_g and causes a linear phase shift of the spectrum. The linear phase shift leads to a shifted pulse in the time domain, see Fig. 1.4(c).

$\boldsymbol{\phi_2}$: is group delay dispersion (GDD) and causes a quadratic phase of the spectrum. The GDD generates a linear modulation on the carrier frequency and a broadening of the pulse envelope. The carrier frequency modulation in combination with the envelope broadening is also called chirp, see Fig. 1.4(d).

$\boldsymbol{\phi_3}$: generates a cubic phase on the spectrum and is called third-order dispersion (TOD). TOD is often neglected; however, it is important to keep in mind that TOD also has an influence on the pulse duration and the pulse shape, see Fig. 1.4(e). Dispersion orders higher than ϕ_3 can usually be legitimately neglected for the type of experiments presented in this thesis.

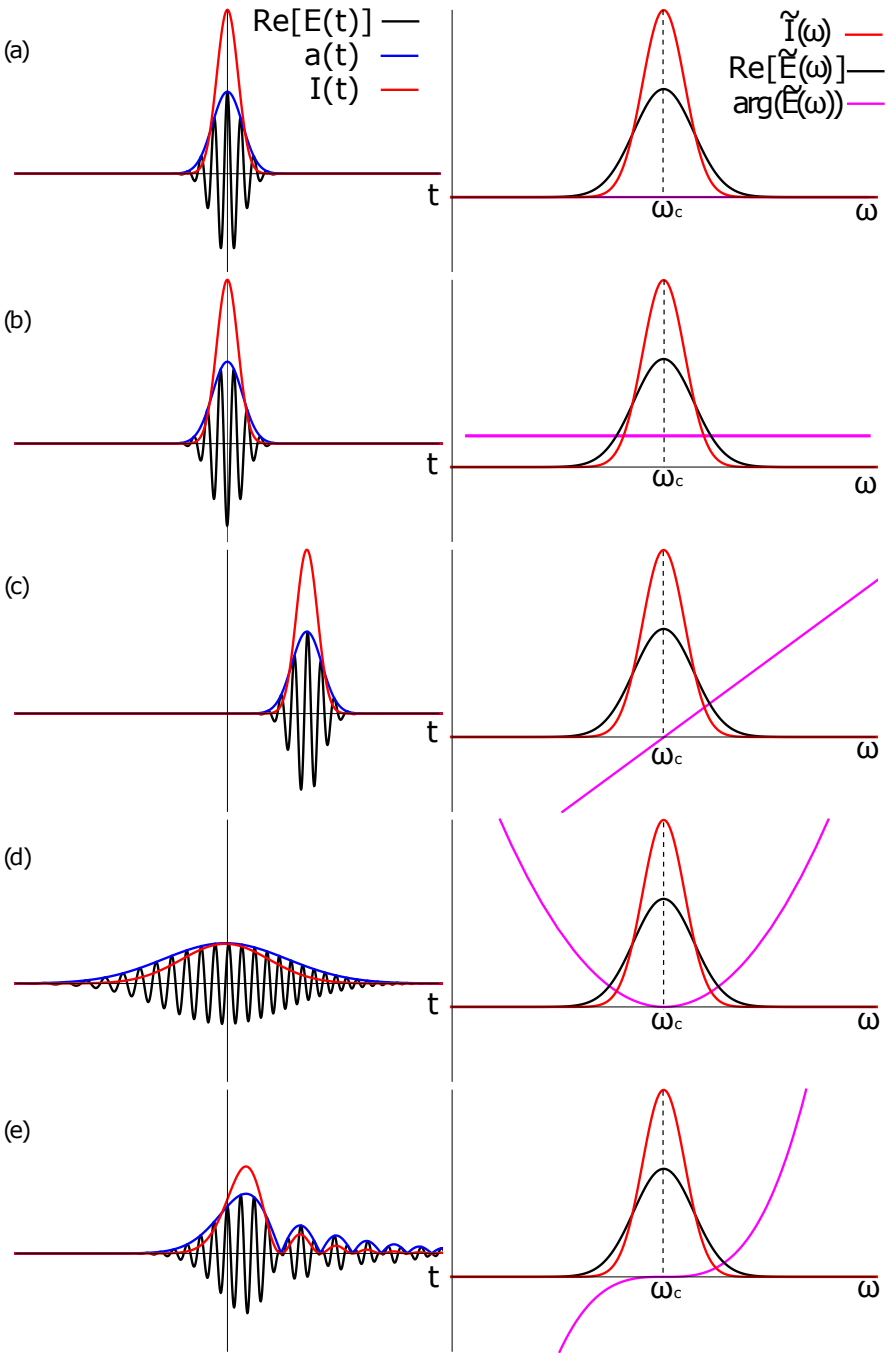

Figure 1.4 – Electric field of a Gaussian pulse in the time and frequency domain: (a) without any spectral phase, (b) with a constant spectral phase, (c) with a linear spectral phase, (d) with a quadratic spectral phase and (e) with a cubic spectral phase.

Depending on the sign of ϕ_2 the GDD is defined as [28] **normal dispersion** for:

$$\underbrace{\frac{\partial^2 \phi(\omega)}{\partial \omega^2}}_{\phi_2} > 0 \tag{1.19}$$

or as **anomalous dispersion** for:

$$\underbrace{\frac{\partial^2 \phi(\omega)}{\partial \omega^2}}_{\phi_2} < 0 \tag{1.20}$$

with the units

$$[\phi_2] = \mathrm{s}^2 \tag{1.21}$$

Please note that different definitions of dispersion are used in optics. The other parameter to define the second-order dispersion is the so-call dispersion parameter D_λ [28], which is defined as

$$D_\lambda = \frac{\partial T_g}{\partial \lambda} = -\frac{2\pi c}{\lambda^2} \frac{\partial^2 k_\mathrm{n}(\omega)}{\partial \omega^2} = -\frac{2\pi c L_\mathrm{d}}{\lambda^2} \frac{\partial^2 \phi(\omega)}{\partial \omega^2} \tag{1.22}$$

with the units

$$[D_\lambda] = \frac{\mathrm{ps}}{\mathrm{nm} \cdot \mathrm{km}}. \tag{1.23}$$

As can be seen in Eq. 1.22, D_λ and ϕ_2 have opposite sings. Care must thus be taken when talking about positive or negative dispersion. It is more common to talk about normal or anomalous dispersion.

Besides the material dispersion, the propagation of a laser pulse inside a waveguide, such as an optical fiber, causes two additional types of phases. For light with a limited transverse extension, the waveguide wave equation must be solved. The solution of the wave equation is light with a transverse mode profile. The simplest mode profile is the Gaussian mode [29]; however, there are more complex ones like e.g. the Hermit-Gaussian modes. Light with multiple transverse modes will have different propagation parameters for every mode. The different propagation parameters lead to a mode-dependent phase shift. However, since single-mode fibers are used in the setups presented in this thesis, i.e. fibers that only support the Gaussian mode for our operation wavelength, this type of dispersion is not relevant for the experiments discussed here.

The second type of dispersion is called waveguide dispersion. The frequency-dependent angle of total internal reflection causes waveguide dispersion. The wave equation for light propagating inside the fiber must be solved to calculate the waveguide dispersion of an optical fiber. The wave equation depends on the

fiber parameters such as the core diameter, the refractive index of the core, and the cladding. The exact values of parameters are usually not easily accessible. However, the wavelength-dependent dispersion of commercially available fibers is usually provided by the manufacturer.

The work presented in this thesis was carried out with fiber lasers operating around 1 µm. Figure 1.5 shows the GDD of a commercial PM980 silica single-mode fiber versus the material dispersion of silica. While the zero-crossing of the material dispersion for fused silica lies around 1.3 µm, the waveguide dispersion shifts the zero-crossing further to longer wavelengths. The shift can be increased by increasing the waveguide dispersion, for example, by making the fiber core smaller. For operation wavelength >1.4 µm, this effect can be exploited to manufacture fibers with normal or anomalous group delay dispersion. Fiber lasers based on Erbium-doped gain fibers operate around 1.5 µm. In Erbium fiber lasers, the GDD is usually managed by balancing fiber sections with normal and anomalous GDD.

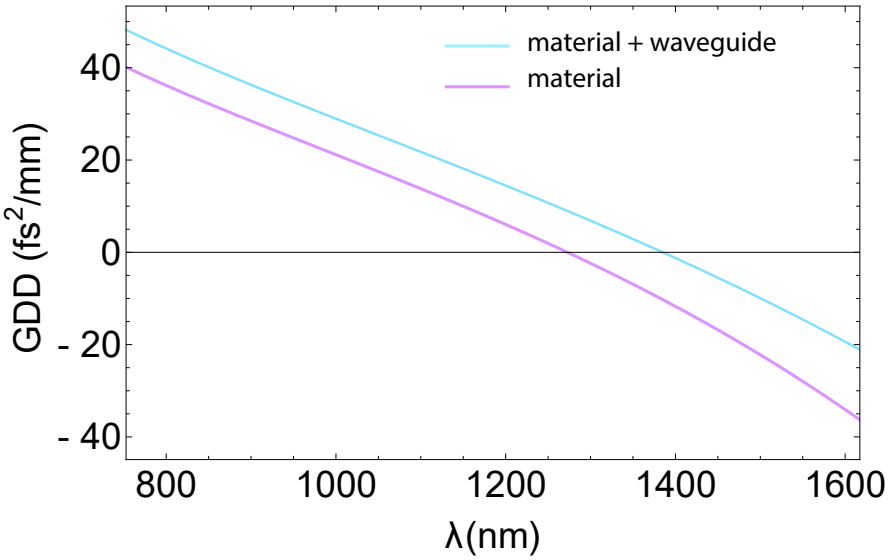

Figure 1.5 – Group delay dispersion of a Nufern PM980-XP single-mode fiber vs. the group delay of silica. The material+waveguide data set was provident by Thorlabs.

However, around 1 µm, manufacturing fibers with anomalous dispersion is difficult. One approach is to design so-called photonic crystal fibers (PCFs), which are fibers with a built-in microstructure [30]. Such fibers are usually expensive and difficult to splice. Hence, usually, other methods for GDD compensation must be used at this wavelength. A standard method is to exploit the wavelength-dependent refraction or diffraction angel by using a prism or diffraction gratings.

The lasers presented in this thesis contain grating compressors that consist

of two transmission diffraction gratings in double-pass configuration. The GDD caused by such an assembly is given by [31]:

$$\mathrm{GDD}_{\mathrm{grating}}(\lambda) = -\frac{\lambda^3 d}{\pi c^2 \Lambda_\mathrm{g}^2}\left(1-\left(\frac{\lambda}{\Lambda_\mathrm{g}}-\sin(\alpha)\right)^2\right)^{-\frac{3}{2}}, \tag{1.24}$$

where d denotes the grating separation, α is the angle of incidence and Λ_g is the grating period. The third-order dispersion of the grating compressor is given by:

$$\mathrm{TOD}_{\mathrm{grating}}(\lambda) = -\frac{\lambda^2}{2\pi c}\frac{\partial \mathrm{GDD}_{\mathrm{grating}}(\lambda)}{\partial \lambda}, \tag{1.25}$$

Note that the sign of the third-order dispersion of the grating compressor and the third-order dispersion of standard optical fibers around 1 µm are the same. This means that third-order dispersion is not compensated in the lasers presented here.

Dispersion and spectral filtering

Another effect of interest concerning dispersion is the combination of dispersion and spectrally dependent losses. According to Eq. 1.12, ultra-short pulses are formed by phase-coherently adding many sinusoidal waves. The relation between the temporal and the spectral domain is given by the Fourier transform. For a pulse without chirp (also called a bandwidth-limited pulse) the following applies: the shorter the pulse, the broader the spectrum. Hence, if we spectrally narrow a bandwidth-limited laser pulse due to spectral filtering, the minimum temporal duration of the pulse becomes longer, see Fig. 1.6. However, we also saw that we can temporally stretch a laser pulse due to dispersion. If we consider an extremely chirped (i.e. stretched) pulse and remove the frequencies forming the temporal wings of the pulse, the pulse may become temporally shorter, see Fig. 1.7. Therefore, spectral filtering can increase but also decrease the pulse duration depending on dispersion.

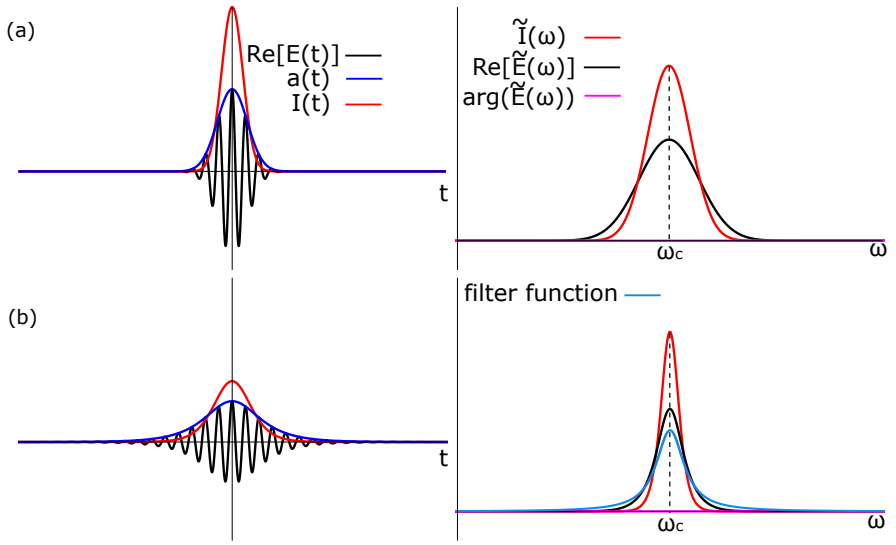

Figure 1.6 – Influence of spectral losses on a bandwidth-limited pulse. (a) Initial pulse in the time and spectral domain. (b) Pulse after applying a spectral filter function. The pulse duration will be increased due to the lower spectral bandwidth.

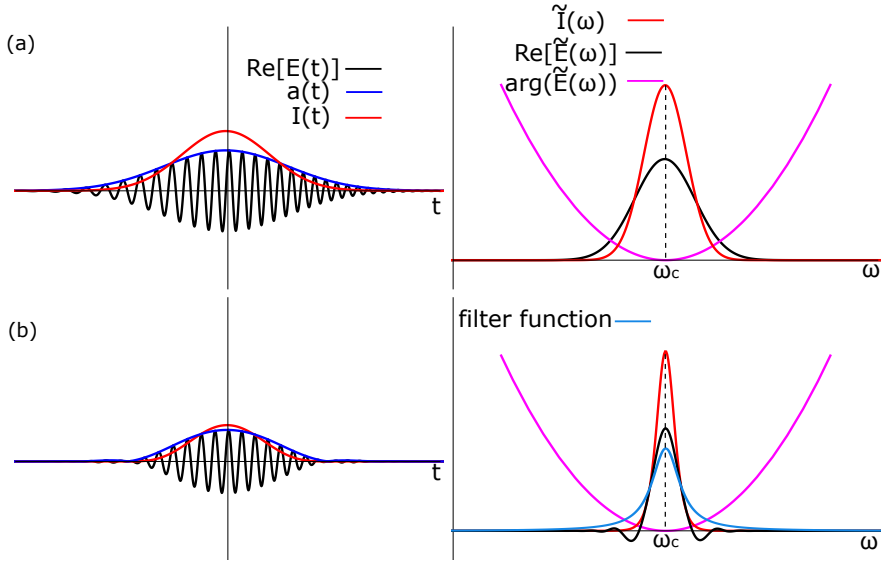

Figure 1.7 – Influence of spectral losses on a chirped pulse. (a) Initial pulse in the time and spectral domain. (b) Pulse after applying a spectral filter function. The pulse duration will be decreased since the spectral filter removes the frequencies forming the temporal wings of the pulse. In this calculation, phase changes due to Kramers-Kronig are neglected.

1.3.2 Nonlinear effects and gain

Besides dispersion and spectral losses, a laser pulse undergoes different effects while propagation inside passive nonlinear or active media.

Self-phase modulation

As discussed in section 1.2.2, SPM is caused by the Kerr effect. Due to the intensity-dependent refractive index n_2, SPM causes a phase shift of the pulse, which can be expressed as [32]:

$$E_{\mathrm{SPM}}(t) = E_0(t)e^{-i\frac{\omega_c n_2 L}{c}I(t)} = E_0(t)e^{-i\gamma_{\mathrm{nl}}P(t)} \text{ with } \gamma_{\mathrm{nl}} \equiv \frac{\omega_c n_2 L}{cA_{\mathrm{eff}}}, \tag{1.26}$$

where $P(t)$ is the power and L is the length of the nonlinear medium and A_{eff} is the effective transverse mode area of the beam. To analyze the influence of SPM

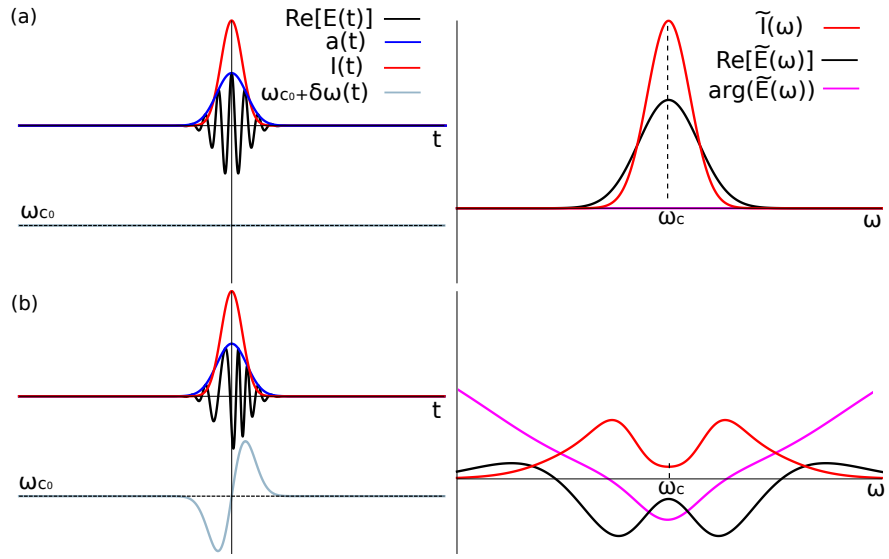

Figure 1.8 – Self-phase modulation acting on a bandwidth-limited pulse. (a) Initial pulse: the carrier frequency ω_c is not time-dependent. (b) Pulse after applying self-phase modulation: the change of the carrier frequency ω_c is given by $\delta\omega(t)$. In the spectral domain the pulse is broadened. The nonlinear broadening caused by SPM has a strong influence on the spectral phase of the pulse.

on an laser pulse, let us consider a Gaussian input pulse as plotted in Fig. 1.8(a) . SPM causes a time-dependent change of the instantaneous frequency of the optical laser pulse. For an unchirped, i.e. bandwidth-limited pulse, this time-dependent change of frequency spectrally broadens the initial pulse, see Fig. 1.8(b).

Saturable absorption

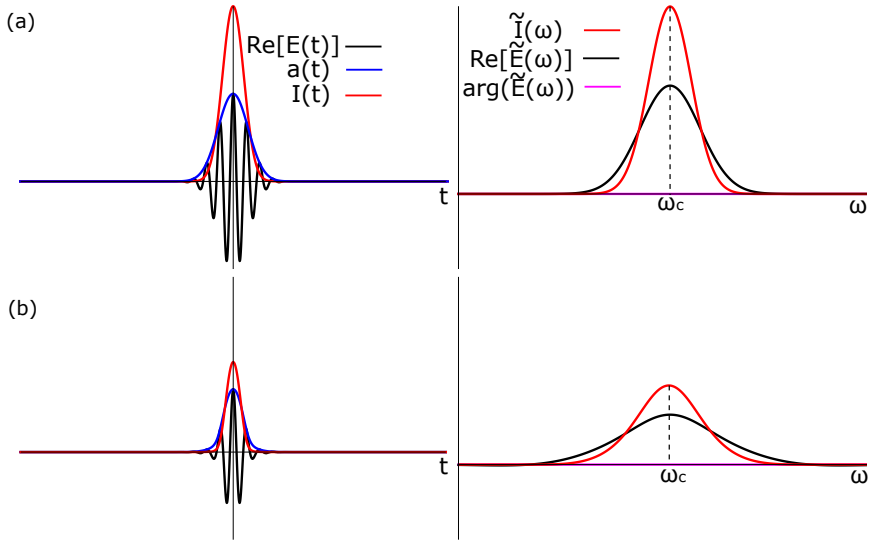

Figure 1.9 – Influence of a saturable absorber on a pulse: the fact that the wings of the pulse get attenuated more than the peak leads to temporal shortening of the pulse.

Besides SPM, another important nonlinear process occurring in mode-locked lasers is saturable absorption. A saturable absorber is an optical component whose absorption decreases when the intensity of the light increases. Saturable absorbers can be implemented with real absorption or via artificial absorption. Artificial absorption refers to an optical device that causes intensity-dependent losses by exploiting nonlinear effects such as self-phase modulation. In section 1.4, different saturable absorbers will be discussed in more detail.

The intensity-dependent absorption coefficient can be expressed by [27]:

$$\alpha(I) = \frac{\alpha_0}{1 + I(t)/I_{\text{sat}}}, \tag{1.27}$$

were $I(t)$ is the time-dependent intensity of the electric field, i.e. $I(t) = \frac{P(t)}{A_{\text{eff}}}$ were $P(t)$ is the optical power and A_{eff} is the effective area of the beam, I_{sat} is the saturation intensity of the absorber, and α_0 is the low-intensity absorption coefficient. Hence, the intensity of a laser pulse with the initial intensity profile $I_{\text{in}}(t)$ after interaction over a length L with a saturable absorber is given according to the Beer-Lambert law by:

$$I_{\text{mod}}(t) = I_{\text{in}}(t) e^{-\frac{\alpha_0}{1+I(t)/I_{\text{sat}}} L} = I_{\text{in}}(t) e^{-\frac{l_0}{1+I(t)/I_{\text{sat}}}}, \tag{1.28}$$

where $l_0 = \alpha_0 \cdot l$ are the low intensity losses. The influence of a saturable absorber on a laser pulse can be seen in Fig. 1.9. Note that in this calculation,

an instantaneous response of the absorber to the intensity profile, i.e. a "fast" saturable absorber, is assumed. The unmanipulated pulse in the temporal and spectral domain is shown in Fig.1.9(a). Due to the time-dependent losses of the saturable absorber the temporal wings of the pulse are suppressed; hence the pulse is temporally shortened. The shorter pulse Fig. 1.9(c) corresponds to a broader spectrum Fig. 1.9(d).

Gain

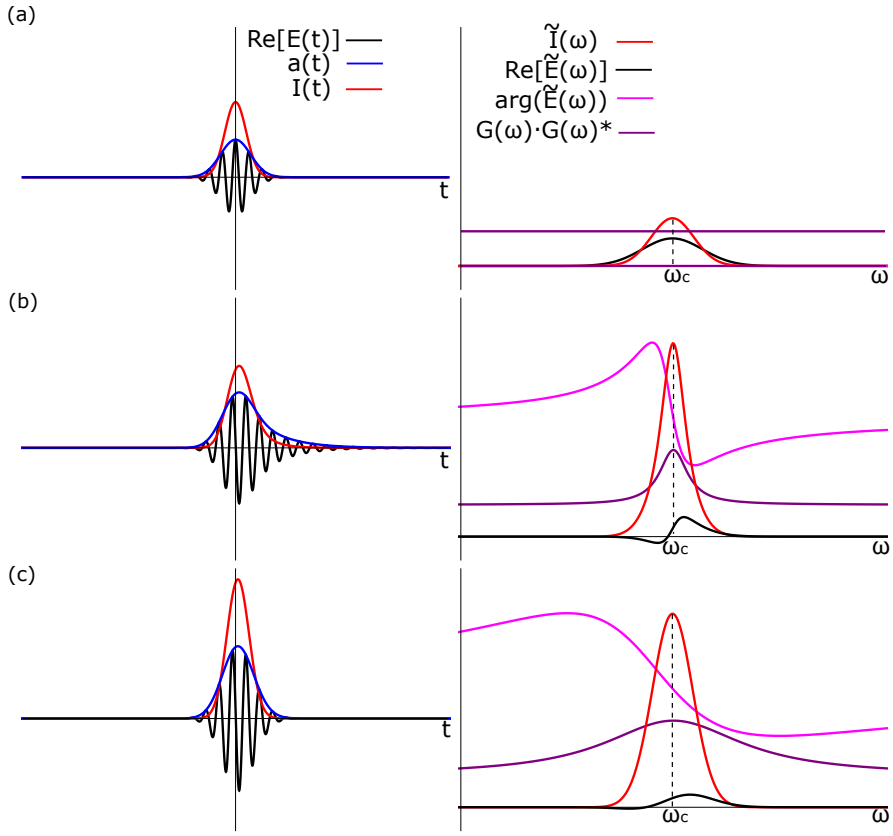

Figure 1.10 – Effect of two different gain profiles on a bandwidth-limited pulse. (a) Initial pulse. (b) Pulse after amplification with a spectrally narrow gain function, (c) pulse after amplification with a broader gain function.

The gain of a laser medium is usually frequency-dependent. Therefore, the influence of gain on a laser pulse is treated in the frequency domain. Let us consider a laser pulse with the electric field $\widetilde{E_0}(\omega)$ which passes through a laser gain medium. The frequency-dependent electric field after one pass through the gain medium $\widetilde{E_g}(\omega)$ will be given by [33]:

$$\widetilde{E_g}(\omega) = e^{-i\omega\Delta t} e^{G(\omega)} \widetilde{E_0}(\omega), \tag{1.29}$$

where $G(\omega)$ is the frequency-dependent gain and Δt is the time delay of the electric field caused by the gain medium. Let us consider a Lorentzian-shaped gain-profile. For this case, the gain function is given by [34, 35]:

$$G(\omega) = G_0 \left(\frac{1}{1 + i\frac{\omega - \omega_0}{\omega_\mathrm{L}}} \right) \tag{1.30}$$

where ω_0 is the position of the gain maximum and ω_L is the FWHM of the intensity gain ($G(\omega) \cdot G(\omega)^*$). The influence of gain on a laser pulse can be seen in Fig.1.10. For a narrow gain profile the pulses is spectral narrowed, hence it is stretched in the temporal domain. For a broadband gain function and low amplification, no such gain narrowing occurs. However, the pulse carrier-envelope-phase undergoes a slip and the pulse is temporally shifted due to the amplification.

1.3.3 Pulse formation and mode-locking

As described in the beginning of this section, laser pulses are formed by the superposition of single sinusoidal frequencies with a defined phase relation. To manipulate the laser resonator in order to enforce a fixed phase relation between these frequencies and thus to form optical pulses is called mode-locking.

The principle behind mode-locking is easy to understand. It is based on energy minimization: pulsed operation is usually ensured by adding a device that introduces high cavity losses for low peak power and small cavity losses for high peak power.

Let us consider a cavity involving a loss mechanism that suppresses resonant feedback for low intensities. Inside such a laser, a small power increment due to some individual waves randomly interfering constructively will be enhanced, since the cavity will offer more feedback for those fluctuations. Due to the higher feedback for constructive interference, more and more individual waves are forced to oscillate in phase, generating an even shorter, more intense pulse. The enhancement of the fluctuation, i.e. the pulse formation, will continue until a certain saturation point is reached, which will be given by the laser dynamics. There are three different main methods to modulate the cavity losses, i.e. to mode-lock a laser:

Active mode-locking is based on an externally driven device that modulates the cavity losses, for example, an acousto optical modulator.

Fourier domain mode locking is based on wavelength-swept light, which is similar to a pulse that is temporal broadened due to dispersion.

Passive mode-locking is based on a saturable absorbers. Saturable absorbers are passive devices that generate losses that can be saturated for high peak powers.

The achievable pulse duration varies strongly between the different mode-locking techniques. Typical pulse durations lie on the order of few tens of picoseconds using active mode-locking [36]. Lasers mode-locked based on Fourier domain mode-locking typically reach pulse durations on the order of 100 ps [37]. However, using passive mode-locking, pulse durations on the order of few femtoseconds can be achieved [34]. In the following, the discussion will be restricted to passively mode-locked lasers.

1.3.4 Passive mode-locked laser

Let us consider a laser resonator with dispersion, wavelength-dependent losses, self-phase modulation, saturable absorption losses and gain, see Fig. 1.11. A laser pulse oscillating in such a cavity will undergo all the effects introduced above.

However, to achieve stable pulsed operation, a steady-state must be found. Steady-state operation means that all influences on the pulse while propagating inside the cavity must cancel each other, i.e. the pulse must reproduce itself after one complete cavity round-trip.

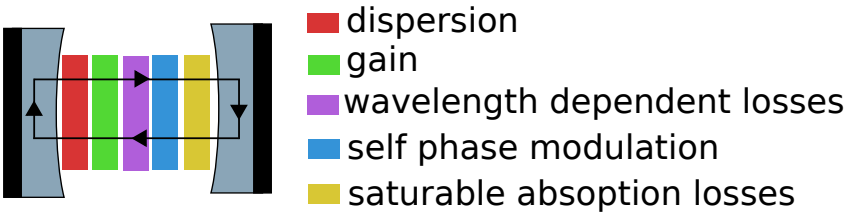

Figure 1.11 – Simple laser oscillator model.

The first analytical model for such a laser setup was developed by Haus et al. [35, 38–40]. This model, also called "master equation" is commonly used to investigate the laser dynamics inside mode-locked lasers [34, 41]. The master equation involves several approximations. One of the main simplification is the assumption of small temporal and spectral changes per resonator round-trip. This assumptions is in good agreement for soliton mode-locked lasers.

However, it has limited validity for lasers where the pulse undergoes large breathing effects while propagating inside the cavity. For such laser systems, numerical methods can be used to analyze the laser dynamics [42]. The analytical

and numerical analysis of mode-locked laser showed that the GDD is one of the main factors that influence the pulse dynamics in mode-locked lasers [34, 35].

For pulsed fiber lasers, different mode-locking states corresponding to different net interactivity GDD regimes have been reported so far, see Kim et al. [43] for an extensive review. The temporal and spectral evolution is plotted in Fig. 1.12 from [43]. In the following, I will summarize the properties of these different characteristic operation regimes.

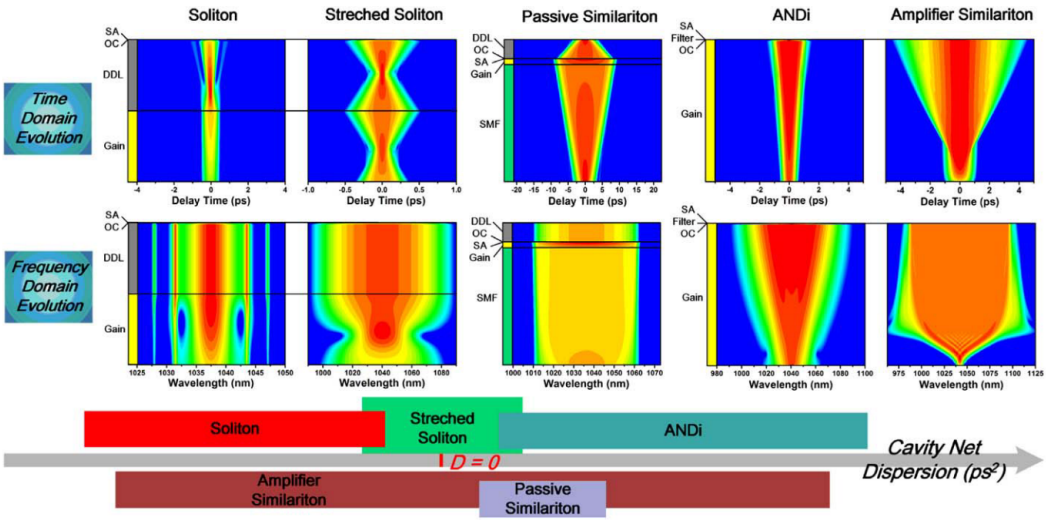

Figure 1.12 – The different pulse shaping mechanisms that can occur in fiber lasers and their temporal and spectral evolution (SA: saturable absorber, OC: output coupler, DDL: dispersive delay line, SMF: single-mode fiber). Reprinted with permission from the author Jungwon Kim and the Optical Society of America from [43]. © The Optical Society.

Soliton regime

For negative net cavity dispersion, the solution of the master equation is the so-called soliton [34, 35, 38, 40, 44]. Soliton pulse formation is given by a fragile balance between a linear chirp due to GDD and a nonlinear chirp caused by self-phase modulation. Ideal solitons propagate inside the laser resonator without changing their spectral shape or the pulse duration. Solitons can exhibit parasitic sidebands. The parasitic sidebands (Kelly sidebands) are generated by soliton perturbations, which are enhanced inside the laser resonator, see Fig. 1.12.

Stretched soliton regime

For stretched soliton pulse formation, all the nonlinear effects are not balancing each other anymore. Instead, the effects introduced at one point in the resonator are compensated at another point. For example, in an Yb:fiber laser, pulses experience normal dispersion in the fiber section of the laser cavity and are then compressed by introducing anomalous dispersion via a grating compressor. In such a setup, the pulse duration will increase in the fiber section and be shortened again by the compressor to reproduce itself after on round-trip. Such a pulse evolution is also called breathing, see Fig. 1.12. The temporal pulse width of stretched solitons inside the laser cavity can vary easily by a factor of 10. Balancing the intensity-driven SPM with the GDD is not necessary anymore. Therefore, stretched soliton pulses can carry much more energy than solitons [43]. The dispersion engineering of the cavity mainly influences the dynamics of the stretched soliton regime. The section of positive and negative dispersion must balance each other. Hence, the total intracavity dispersion must be close to zero for stretched soliton operation since the SPM effects do not have a large influence on the pulse dynamics.

Self-similar regime

For fibers with large fiber sections featuring normal dispersion, similariton pulse operation can occur. The chirp accumulated in the normal dispersion section is compensated via a dispersive delay line (DDL) providing anomalous dispersion. The spectral broadening is compensated by the amplification in a short gain fiber. The gain-narrowing is filtering the spectral bandwidth and allows for stable pulse operation [45].

All-normal dispersion regime

In the all-normal dispersion regime, the pulse dynamics inside the cavity is not dominated by dispersion anymore. In such a configuration, so-called dissipative solitons can be generated. Dissipative solitons are a fundamental extension of conventional soliton theory [46]. To obtain dissipative solitons, the balance between nonlinear effects and GDD is replaced by a new balance between nonlinearity, dispersion, gain, and loss [43]. However, the important concept is that dissipative solitons can exchange energy with their environment for self-stabilization, for example, by exciting phonons in the material. In this regime, an additional spectral filter, which modulates the spectral losses, has to be inserted into the laser cavity in order achieve a reproducible round-trip solution.

Chimera-mode-locking

For specific intracavity dispersion values, the pulses may experience pulse formation dynamics, which are characteristic of two different operation regimes. Therefore, the effects described above can usually not be separated. Such chimeric mode-locking states can occur especially in fiber lasers which are operating close to zero dispersion.

All the different dispersion regimes offer different operation parameters in terms of output power, spectral bandwidth, pulse duration, and noise. Therefore, a systematic study of the different operation regimes in a given laser is important to find the best operation point for the planned application.

1.4 Mode-locking techniques for fiber lasers

Besides the dispersion of the laser resonator, also the behavior of the saturable absorber has a significant influence on the laser dynamics, since it is usually responsible for the initiation and stabilization of the mode-locked operation. Various experimental implementations of real or artificial saturable absorbers have been reported in the literature. Choosing the type of saturable absorber will strongly affect the experimental realization of a mode-locked laser. This section will give a short overview of different implementations of saturable absorbers that are suitable for mode-locking fiber lasers and will discuss their advantages and disadvantages.

1.4.1 Semiconductor saturable absorber mirror

A semiconductor saturable absorber mirror (SESAM) [47, 48], as the name suggests, is a semiconductor mirror with an embedded saturable absorber. A significant drawback of SESAMs is that they can be prone to damage. It requires a careful absorber design and a careful choice of spot size, peak power, and thermal cooling to get long-term stable operation. The starting of mode-locked lasers typically happens via a Q-switching regime. Q-switching means that giant pulses inside the cavity are generated. They are caused by the high cavity losses for continuous-wave lasing, which suppress the feedback to the gain material. Hence, the gain material stores more energy than in a steady pulse state due to the decreased stimulated emission. Small fluctuations inside the cavity lead to a reduction of the cavity losses and to an increased feedback to the gain material. The stored energy is released, and a giant pulse is generated. The giant pulse generation occurs every time the laser is started. Every time the laser is turned on, the saturable absorber mirror may be slightly damaged by one of the Q-switching

pulses; as a consequence, degradation can happen. SESAMs are also not commercially available on stock, since the careful absorber design must be adapted to the laser resonator. However, other mode-locking methods offer the advantage of tunability of several absorber parameters.

1.4.2 Nonlinear polarization evolution

Due to the small beam diameter inside optical fibers, which is constant over the complete fiber length, several nonlinear effects can be exploited. One of the most common methods to achieve mode-locking in fiber lasers is the so-called nonlinear polarization evolution or sometimes also called nonlinear polarization rotation (NPR) technique [49–51]. NPR is based on the Kerr effect. Due to the high peak power in the optical fiber, a peak-power-dependent polarization rotation occurs. This evolution is mainly caused by SPM and arbitrary birefringence of the fiber. By using selective polarization elements inside the laser, mode-locking can be achieved. A typical setup of an NPR-fiber-laser can be seen in Fig.1.13(a). However, the standard NPR technique requires the use of non-PM fibers. These lasers are, therefore, very sensitive to environmental fluctuations. Furthermore, the mode-locking is depending on the birefringence inside the fiber section. This birefringence is depending on the geometric position of the fiber. Even the slightest changes of the fiber geometry (radius of curvature, twist, etc.) will change the mode-locking behavior. Care must be taken when planning such a laser setup. One of the main disadvantages is that, if the laser is turned off and on again, it is a difficult task to reproduce the exact mode-locking state. Fig. 1.13(b) shows the optical output spectrum of a home-built NPR-laser, which has been turned on and off ten times. Note that with great care, the initial mode-locking state can be reproduced. However, the laser is usually not self-starting.

1.4.3 Nonlinear loop mirrors

The nonlinear loop mirror (NOLM) [52] was invented to overcome the drawback of not being able to use polarization-maintaining fibers. A NOLM is based on a standard optical X-fiber-coupler where two ports are spliced together to form a fiber loop, see Fig. 1.14(a). Light sent into the loop at one port is split by the coupler with a splitting ratio given by the coupler. Now the light is propagating in clockwise and counterclockwise direction inside the fiber loop. If some light is coupled to the NOLM at port 1 and the peak power is large enough, nonlinear effects will occur. In particular, the Kerr effect will generate a peak power-dependent refractive index; hence, the light will experience a peak power-dependent optical

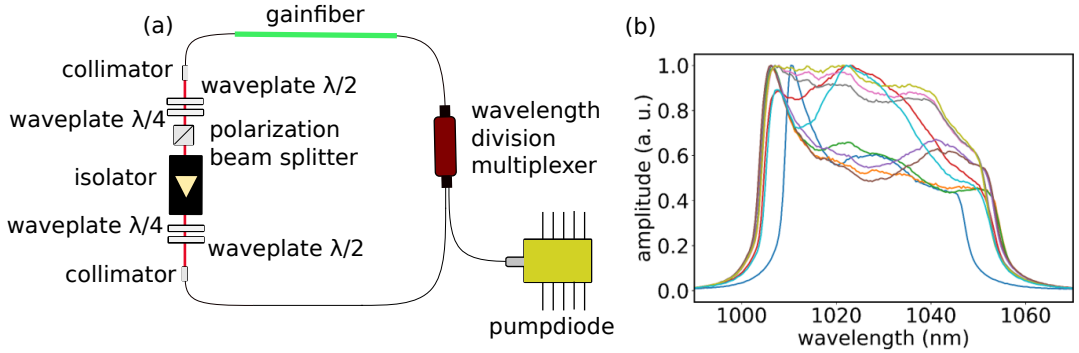

Figure 1.13 – (a) Schematic drawing of an NPR mode-locked laser. (b) The spectrum of an NPR mode-locked laser turned off and on again ten times.

path length. If we now consider for instance a splitting ratio of 60:40 between the clockwise and counterclockwise propagating light, a phase delay between the two propagation directions will occur. Depending on the phase shift between the two propagation directions, a section of light is coupled to port 2, while the rest is reflected to port 1. This peak power-dependent behavior of the NOLM can be exploited for mode-locking. The percentage of light coupled from port 1 to port 2 as a function of the nonlinear phase shift difference $\Delta\phi$ can be seen in Fig. 1.14(c).

The basic NOLM design has several disadvantages when used as a saturable absorber. High input peak power values are needed to generate a significant nonlinear phase shift, and the splitting ratio must not be 50:50 to obtain a different phase shift for the two propagation directions. However, with a non-50:50 splitting ratio, the contrast of the NOLM (maximum light transmitted from port 1 to port 2) can not be 100%, see Fig 1.14(c). The lack of contrast occurs since the two interfering waves do not have the same intensity; hence, they can not cancel each other completely, not even with a phase shift difference of π. For better

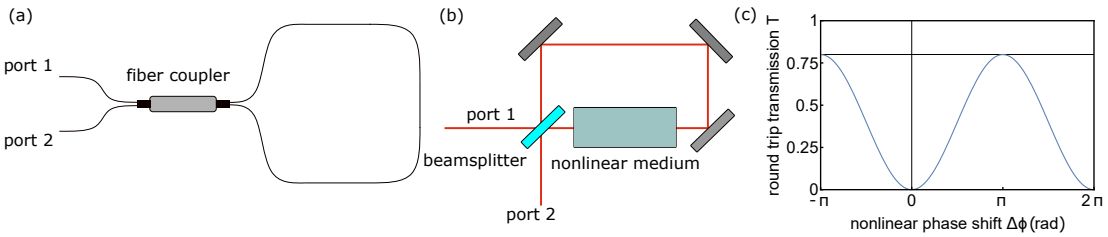

Figure 1.14 – (a) Schematic drawing of a nonlinear loop mirror (NOLM). (b) A free-space NOLM for better understating of the operation principle. (c) The transfer function of the NOLM, i.e. the ratio of light coupled from port 1 to port 2 as a function of the nonlinear phase shift difference between the two interfering waves.

understanding, a free-space version of the NOLM is shown in Fig. 1.14(b). It is an interferometer with a nonlinear medium, where both arms are short-circuited. In this configuration, it is more intuitive to see that due to the interference of the light depending on the nonlinear phase shift, light is either coupled to port 1 or port 2.
However, the problem of not having a 100% switching capability can be overcome by using a nonlinear amplifying loop mirror (NALM), as will be described in the following section.

1.4.4 Nonlinear amplifying loop mirrors

A NALM [53] is based on the same principle as a NOLM, but additionally contains an asymmetrically placed gain fiber. Figure 1.15(a) shows a sketch of a NALM setup. Due to the asymmetric amplification, the counterclockwise and clockwise propagating light experience different optical path lengths for different peak powers. A free-space version of a NALM can be seen in Fig 1.15(b). For the configuration shown in Fig.1.15(a) and (b), the clockwise propagating light travels a short distance before the amplification and a long distance after the gain medium. On the other hand, the counterclockwise propagating light travels a long distance before the amplification and a short distance after the amplification. Hence, even for a 50:50 splitting ratio, the counterclockwise and the clockwise propagating light experience different phase delays due to the asymmetric amplification. If we take a look at the maximum light that can be transmitted from port 1 to port 2, see Fig. 1.15(c) the NALM can achieve a contrast of 100%.

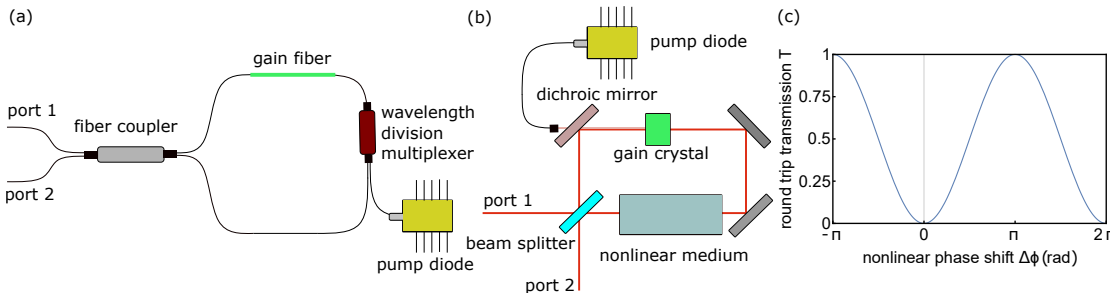

Figure 1.15 – (a) Schematic drawing of a NALM. (b)Free-space version of a NALM for better understating of the operation principle. (c) The transfer function of the NALM.

1.4.5 Figure-8 laser

The first laser mode-locked with a NALM was reported by Duling [54]. In addition to the NALM-loop, a second loop is formed by splicing together the remaining two ports of the fiber coupler. Due to their shape, these lasers have been termed figure-8 lasers. A schematic of the laser can be seen in Fig.1.16. The second loop usually consists of an additional fiber-coupler for coupling light out of the resonator and an optical isolator. The optical isolator ensures unidirectional operation. Let us consider a coupler with a 50/50 splitting ratio, and light coupled into the NALM via port 1. At low peak powers, no phase delay will occur and all light is reflected back to port 1. In this configuration, the isolator blocks all the light, and the laser resonator has 100% losses. Hence, no continuous-wave lasing is possible. However, at high peak powers, a phase shift between the clockwise and the counterclockwise propagating light will occur, and some of the light is coupled into the second loop via port 2. The fraction of light coupled into port 2 will be transmitted through the cavity. In the figure-8-configuration, port 2 is the so-called transmission port. The percentage of light coupled to the transmission port as a function of difference in nonlinear phase shift is the so-called transmission function of the laser.

The transmission function is plotted in Fig 1.16(b). For a zero nonlinear phase shift difference $\Delta\phi$, the cavity transmission is zero. For an increasing $\Delta\phi$, the transmission of the cavity is increasing, leading to higher peak power and a further increase of the difference in nonlinear phase shift until the maximum transmission is reached. Any further increase of $\Delta\phi$ decreases the power inside the cavity, hence decreasing $\Delta\phi$. Therefore, once the point of maximal cavity transmission is reached, it is self-sustaining, at least for small perturbations. The transfer function of figure-8 lasers starts at minimum transmission, which causes several problems. First of all, a π phase shift is needed to reach maximum transmission. Depending on the pulse parameters, such a large phase shift may not be reachable. Addi-

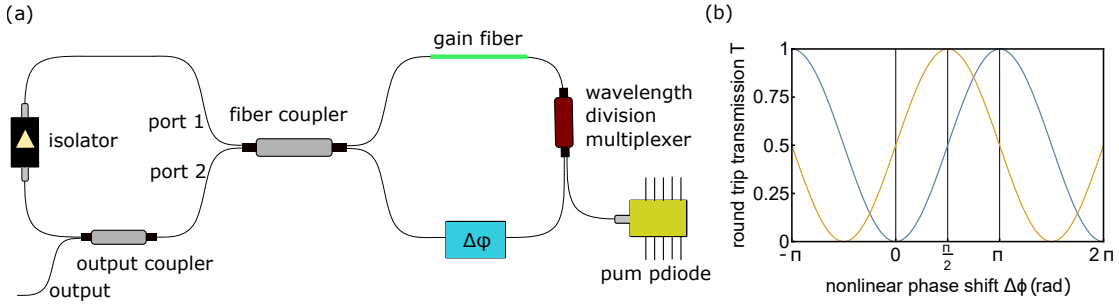

Figure 1.16 – (a) Schematic drawing of a figure-8 laser. (b) Transmission function of the figure-8 laser without (blue) and with (orange) a non-reciprocal phase bias.

tionally, the gradient of the transmission function around zero is zero; therefore, figure-8-lasers need large perturbations to initiate mode-locking. These perturbations are usually generated by an additional electro-optical-modulator inside the laser resonator or by over-pumping the laser with an extremely high amount of pump power.

By adding a non-reciprocal phase bias to the NALM section, the figure-8 laser can be made self-starting [55]. The non-reciprocal phase bias consists of two Faraday rotators and a wave plate. The wave plate defines the amount of phase shift. A quarter-wave plate, for example, generates a $\pi/2$ phase shift. To implement the non-reciprocal phase bias, a free-space section is added to the NALM loop. The most straight-forward method is the following (see Fig. 1.17): two collimators are spliced to the fiber tips. The slow axes of both fibers should be aligned horizontally. Since spontaneous amplified emission, which initially starts the lasing process, is not polarized, one of the fiber axes of the laser resonator should be blocked. For this purpose, a polarization beam splitter cubes can be placed in front of each collimator. Now, a Faraday rotator is introduced such that it rotates the polarization of the light by 45° in one direction, while the second rotator rotates it by 45° in the opposite direction. The wave plate is put between the two rotators. The wave plate should be aligned such that the polarization of the light propagating in one direction is parallel to the fast axis of the wave plate, while the polarization of the light travelling in the opposite direction is perpendicular to the fast axis. Due to the wave plate, an additional phase shift between the propagation directions is generated. This non-reciprocal phase bias shifts the transfer function, thus enabling to set a "start" phase offset. Due to this offset, a smaller amount of nonlinear phase shift is required to obtain mode-locking. Nevertheless, figure-8 laser have their limitations when it comes to increasing the repetition rate, since they consist of two fiber loops whose lengths are difficult to reduce arbitrarily. The figure-9 laser was invented to reach higher repetition rates.

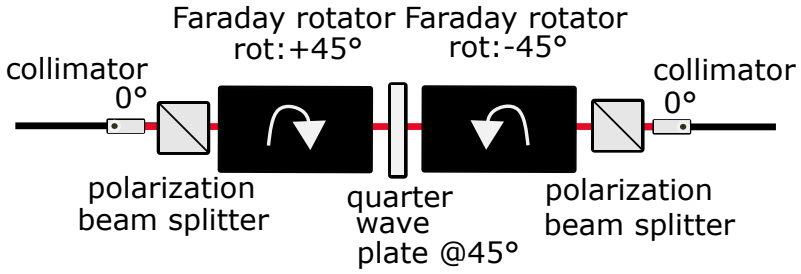

Figure 1.17 – (a) Schematic drawing of a phase bias assembly.

1.4.6 Figure-9 laser with a fixed-ratio fiber coupler

Figure-9 lasers [56] are based on a NALM. The difference between the figure-8 and the figure-9 laser is that instead of building an external fiber loop with port 1 and port 2, only port 1 is used to build the cavity. The light coupled out of port 1 is coupled back into the NALM by a mirror. The figure-9 configuration is thus more compact, see Fig.1.18(a). In this configuration, the cavity transfer function

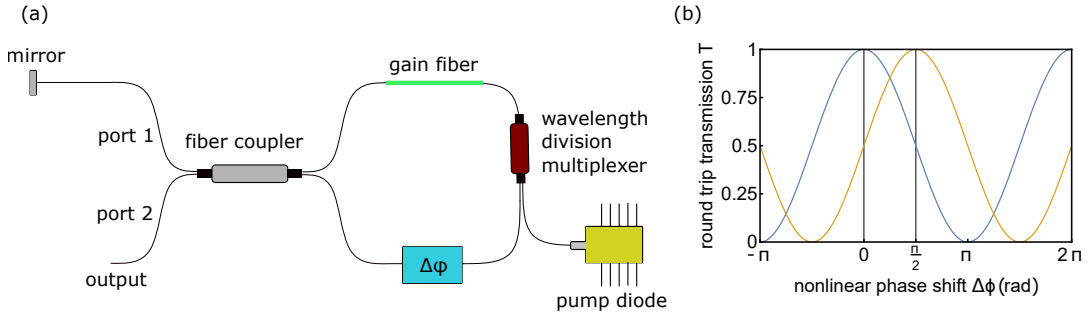

Figure 1.18 – (a) Schematic drawing of a figure-9 laser. (b) The transfer function of the figure-9 laser without (blue) and with (orange) a non-reciprocal phase bias for a 50/50 splitting ratio.

is defined as the light that is coupled from port 1 back to port 1. Light coupled from port 1 to port 2 will be coupled out of the cavity, hence generating cavity losses. If we now take a look at the transfer function of the figure-9 resonator, see Fig 1.18(b), we can see that for zero phase shift, the transmission is on its maximum. In such a configuration, the laser is lasing in continuous-wave operation. However, if an additional non-reciprocal phase bias is added to the NALM-loop, the transfer function can be shifted. The operation principle of the non-reciprocal phase bias for the figure-8 and the figure-9 laser is the same.

The transmission function of the laser is now given by the fixed phase shift of the wave plate and the fixed splitting ratio of the fiber-coupler. The only changeable parameter in this setup is the pump power. Therefore, the splitting ratio of of the fiber-coupler, the asymmetry of the loop and the non-reciprocal phase shift must be carefully designed for the targeted laser system to be able to achieve mode-locking. A more flexible solution was been reported by Hänsel et al in 2017 [57]. Instead of using a fiber coupler with a fixed splitting ratio, they used a polarization beam combiner.

1.4.7 Figure-9 laser with a polarization beam splitter

The polarization beam combiner/splitter splits light coming from the free-space section into a vertically and a horizontally polarized beam. Each of the beams is coupled into one of the NALM loop ports. The PM fiber tips of the NALM are rotated by 90° with respect to each other. At both ports, the light is coupled into the slow axis of the fiber. After one round-trip in the fiber loop, the light is again recombined by the polarization beam combiner and coupled back into the free-space section. This configuration leads to the following effect: the x-component of the electric field becomes the y-component and vice versa after one round-trip in the NALM, see Fig. 1.19. It is important to mention that this does not correspond

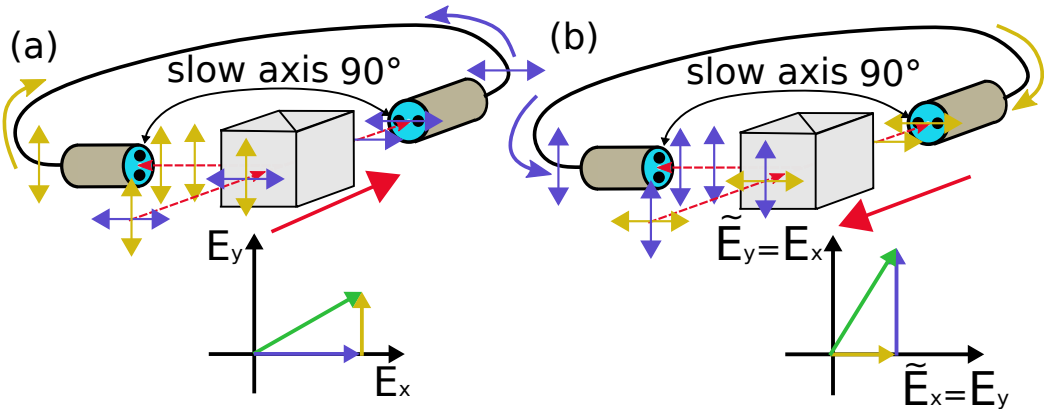

Figure 1.19 – (a) Electric field coupled into the fiber loop. (b) Electric field after one round-trip in the fiber loop. Due to the 90° angel, the axes of the incoming and the outgoing electric field are switched.

to a rotation but a switch of field components. In the free-space section, the light is sent through a Faraday rotator and an additional polarization beam splitter cube. The cavity is formed by reflecting the light back into the loop with an end mirror. Figure 1.20(a) shows the setup. The losses of the NALM are now not generated anymore by a classic interferometric behavior, but by polarization rotation. The phase shift of the NALM leads to an elliptical beam in the free-space section, and the polarization beam splitter cube generates the losses. Therefore, this laser can be seen as a combination of an NPR laser and an all-PM-NALM.

The major advantage compared to standard NPR lasers however is that the figure-9 laser is based on an all-PM design, which offers higher stability against environmental perturbations. The transmission function for the configuration shown in Fig 1.20(a) without a wave plate in the free-space section is the same as for the figure-8 laser without a non-reciprocal phase bias. Note that this is only true if the two polarization beam splitter cubes have the same orientation. If one of the

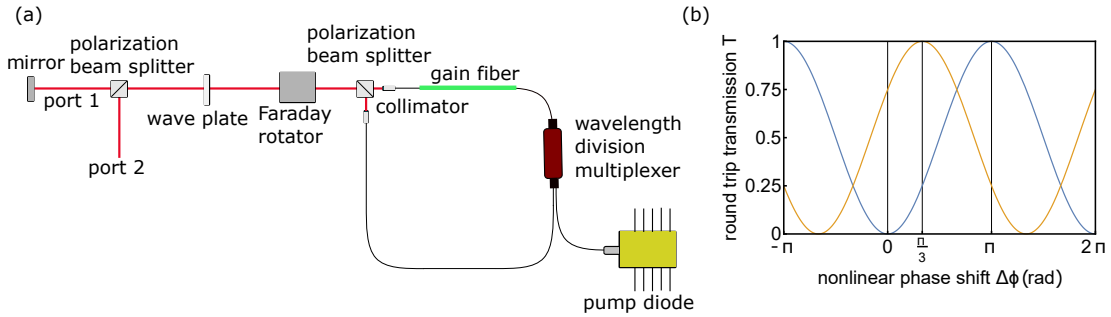

Figure 1.20 – Schematic drawing of a figure-9 laser with a polarization beam splitter. (b) Transmission function of the figure-9 laser without (blue) and with (orange) a non-reciprocal phase bias.

cubes is rotated by 45° with respect to the other one, the resulting transmission function will be the same than the one of the standard figure-9 laser featuring a fixed fiber splitter, i.e. starting with maximum transmission for $\Delta\phi = 0$.

However, for the configuration with the same orientation of the cubes the laser could theoretically mode-lock similarly to the figure-8 laser without any additional phase bias; however, high pump power or an initial modulation would be needed to mode-lock this laser. Therefore, an additional non-reciprocal phase bias is added.

The phase bias is introduced by adding a quarter- and a half-wave plate after the Faraday rotator. With these two wave plates the transmission function can be manipulated in many ways see, chapter 3. However, since this manipulation of the transmission function is not really intuitive, the cavity transmission function has been calculated using Jones matrices. A detailed discussion of these calculations will be presented in Chapter 3. The laser configuration presented in this section is the basis for the single- and dual-frequency combs presented in chapter 3 and 4

1.5 Optical frequency combs

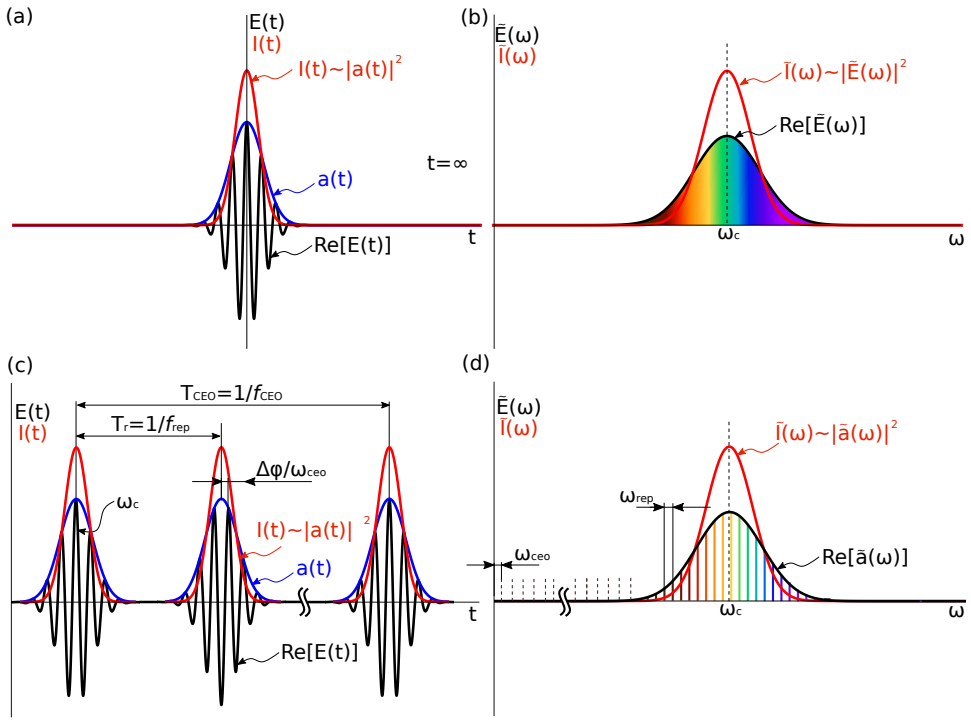

Figure 1.21 – Optical frequency comb principle. To generate a single clean and sharp laser pulse in the time domain (a), an infinite number of frequencies are needed in the spectral domain (b). If an infinite pulse train (c) is Fourier-transformed, the result is a comb-shaped spectrum (d). Please note: $\omega_{\mathrm{ceo}} = 2\pi f_{\mathrm{ceo}}$ and $\omega_{\mathrm{rep}} = 2\pi f_{\mathrm{rep}}$.

To understand the relation between mode-locked lasers and OFCs, let us reconsider a single laser pulse as described by Eq. 1.12, see Fig. 1.21(a),(c). The carrier wave $e^{i\omega_c t}$ propagates with the phase velocity v_{p}, while the envelope $a(t)$ of the time-dependent electric field propagates with the group velocity v_{g}, where

$$v_{\mathrm{g}} = \left(\frac{1}{v_{\mathrm{p}}} + \frac{dn(\omega)}{d\omega} \frac{\omega}{c} \right)^{-1} . \tag{1.31}$$

In a dispersion-less environment, $v_{\mathrm{p}} = v_{\mathrm{g}}$. The single pulse is formed by an infinite number of frequencies. However, the electric field of the mode-locked lasers presented in this thesis is generated by the in-phase oscillation of the modes inside the laser cavity. Hence, the electromagnetic field is not generated by a continuous frequency spectrum, but by modes separated by the fundamental resonator frequency f_{rep}, which is given by

$$f_{\mathrm{rep}} = \frac{c}{L_{\mathrm{o}}(n(\lambda_{\mathrm{c}}))}, \tag{1.32}$$

where c is the speed of light and $L_o(n(\omega_c))$ is the cavity round-trip length depending on the refractive index and the center wavelength λ_c.

The resulting electric field in the time domain in this case does not corresponds to a single laser pulse, but to an infinite number of pulses, i.e. a pulse train. The pulses are separated in time by the cavity round-trip time T_r, which is given by $T_r = 1/f_{rep}$. For $v_g = v_p$, the pulse train can be described as as a convolution of the single-pulse field with a sum of delta-functions:

$$E(t) = a(t)e^{i\omega_c t} * \sum_{m=-\infty}^{\infty} \delta(t - mT_r). \tag{1.33}$$

However, if we consider the dispersion inside a real laser cavity ($v_g \neq v_p$), a phase offset $\Delta\Phi_{CEO}$ will occur between the carrier frequency and the pulse envelope, see Fig.1.21(b). This carrier-envelope offset (CEO) phase is given by

$$\Delta\Phi_{CEO} = \omega_c L_r \left(\frac{1}{v_p} - \frac{1}{v_g} \right), \tag{1.34}$$

where L_r is the cavity round-trip length. It is important to understand that $\Delta\Phi_{CEO}$ is caused by first-order dispersion, i.e. the difference between v_p and v_p. Furthermore, $\Delta\Phi_{CEO}$ is also influenced by a change of the cavity length in the case of non-zero dispersion. The rate at which the CEO phase changes per round-trip is given by the carrier-envelope offset frequency f_{ceo} [58]:

$$f_{ceo} = \frac{\Delta\Phi_{CEO} \mod (2\pi)}{2\pi} f_{rep}. \tag{1.35}$$

Thus, for $v_g \neq v_p$, the electric field of the pulse train can be re-written as

$$E(t) = a(t)e^{i(\omega_c t + 2\pi f_{CEO} t)} * \sum_{m=-\infty}^{\infty} \delta(t - mT_r). \tag{1.36}$$

The Fourier-transform of this pulse train corresponds to

$$\tilde{E}(\omega) = \tilde{a}(\omega - \omega_c)\frac{1}{2\pi} \sum_{m=-\infty}^{\infty} \delta(\omega - m2\pi f_{rep} - 2\pi f_{ceo}). \tag{1.37}$$

which is the comb-like spectrum that can be seen in Fig.1.21(d). Since every comb line f_n can be written as

$$f_n = f_{ceo} + n f_{rep} \tag{1.38}$$

where n is an integer number, the position of each frequency lines can be fixed by stabilizing f_{rep} and f_{ceo}.

The ability to perform simultaneous spectral measurements over a large bandwidth using all these comb lines simultaneously is one reason why optical frequency combs are so valuable for spectroscopy.

1.6 Noise of optical frequency combs

In section 1.5, we considered the output of a mode-locked laser to be a perfect pulse train and the spectrum of such a perfect pulse train to consist of delta functions. However, real lasers suffer from perturbations and fluctuations influencing the pulse train parameters. Figure 1.22 from [59] gives a good overview of the different noise sources in a mode-locked laser and how they influence the pulse train parameters and the corresponding accessible measurement values.

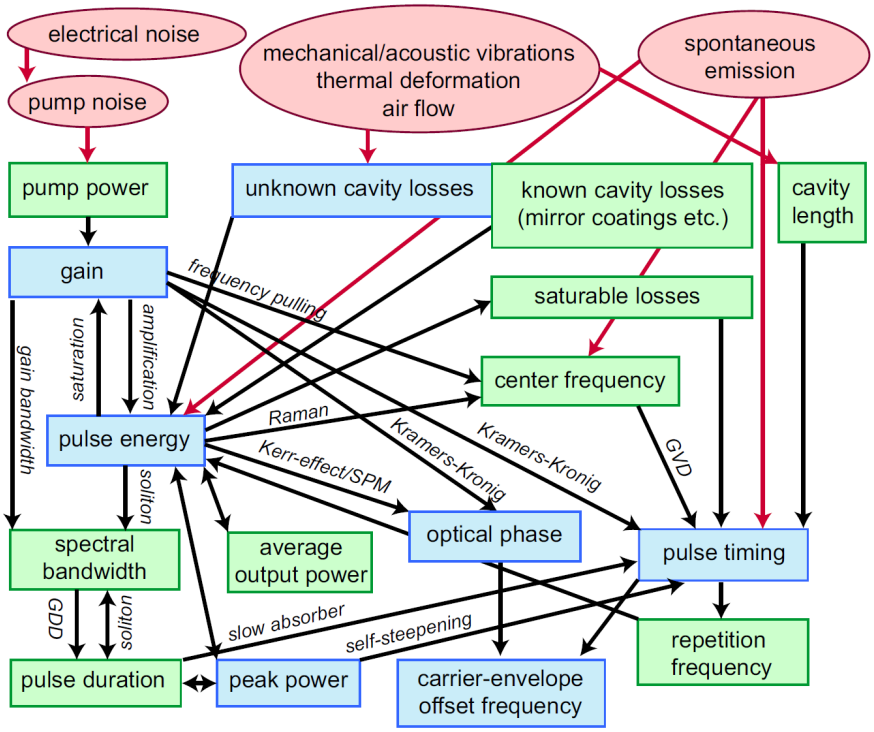

Figure 1.22 – Influence of different noise sources (red) on the hidden (blue) and directly measurable (green) pulse parameters. Reprinted, with permission, from Aline Mayer [59].

1.6.1 Noise and the optical spectrum

Let us assume that the noise perturbs the pulse train, but does not break it up, i.e. that the spectral comb structure is still maintained. In this case, the comb lines are no perfect delta functions anymore, but will fluctuate in time, i.e.

$$f_{\mathrm{n}}(T) = f_{\mathrm{ceo}}(T) + n f_{\mathrm{rep}}(T), \tag{1.39}$$

where T is a time much slower than the cavity round-trip time. According to Eq. 1.39, the noise of the individual comb lines is given by the line number n and

the fluctuations of both f_{rep} and f_{ceo}.

Hence, a perturbation δX of the laser parameter X (i.e. pump power, cavity length, cavity losses etc.) will result in a fluctuation of the comb lines that can be expressed as [60]

$$\delta f_{\mathrm{n}} = \delta X \frac{\mathrm{d}f_{\mathrm{ceo}}}{\mathrm{d}X} + n\delta X \frac{\mathrm{d}f_{\mathrm{rep}}}{\mathrm{d}X}. \tag{1.40}$$

Depending on the magnitude and sign of the fluctuations of f_{ceo} and f_{rep}, there will be one comb line for which these fluctuations cancel out, i.e. where $\delta f_{\mathrm{n}} = 0$. This so-called "fixed point" is given by $f_{\mathrm{n}} = n_{\mathrm{fix}} f_{\mathrm{rep}} + f_{\mathrm{ceo}}$ and n_{fix} can be calculated as

$$n_{\mathrm{fix}} = -\frac{\frac{\mathrm{d}f_{\mathrm{ceo}}}{\mathrm{d}X}}{\frac{\mathrm{d}f_{\mathrm{rep}}}{\mathrm{d}X}}. \tag{1.41}$$

The fixed point may lie within the optical laser output spectrum or even at the carrier frequency, but does not necessarily need to. As a simple example, let us consider a perturbation which only influences f_{rep}: such a perturbation would lead to $n_{\mathrm{fix}} = 0$ and hence the fix-point would be exactly at f_{ceo}. On the other hand, if the perturbation only influences f_{ceo}, then $n_{\mathrm{fix}} = \infty$. However, most perturbations usually have an influence on f_{ceo} as well as on f_{rep}. The impact of the different noise sources summarized in Fig. 1.22 and their corresponding fix points can be analytically derived, for a detailed review see Newbury et al. [60].

1.6.2 Noise and the radio frequency spectrum

The noise of the individual-comb lines can be directly measured by beating the OFC with a stabilized continues-wave laser. We saw above that the noise of the comb lines is given by the noise of f_{ceo} as well as of f_{rep}, which are both radio frequency signals. If the OFC is impinging on a fast photodiode, the optical pulse train will be converted into a radio frequency signal. Therefore, the noise performance of the OFC can also be characterized by measuring the noise properties of f_{rep} by analyzing the electric pulse train and measuring the f_{ceo} frequency using an f-to-$2f$ interferometer. A detailed explanation of how noise manifests itself in the radio frequency spectrum and how it can be measured can be found in [59]. In the following, I will summarize the most important aspects. The duration of the pulses generated in passively mode-locked lasers can easily reach sub-100 fs plus duration. Since these pulses are much shorter than the response time of photodiode, the electronic signal will be given by the response of the photodiode. If the time between the pulses is sufficiently large compared to the photodiode response

time, the pulse train $I_{\mathrm{p}}(t)$ can be expressed as a train of delta functions:

$$I_{\mathrm{p}}(t) = P_{\mathrm{av}} T_{\mathrm{r}} \sum_{n=-\infty}^{\infty} \delta(t - nT_{\mathrm{r}}), \tag{1.42}$$

where P_{av} is the average power and T_{r} is the cavity round-trip time (see Fig.1.23(a)). For an ideal photodiode, the current is proportional to $I(t)$. For noise measurements the photodiode signal is usually analyzed using a signal-source or a radio-frequency analyzer. These measurement devices measure the power spectral density $S_{xx}(f)$, which is given by:

$$S_{xx}(f) = \left| \tilde{I}_{\mathrm{p}}(f) \right|^2 . \tag{1.43}$$

hence [59]:

$$S_{xx}(f) = P_{\mathrm{av}}^2 \sum_{n=-\infty}^{\infty} \delta(f - nf_{\mathrm{rep}}), \tag{1.44}$$

the latter is plotted in Fig.1.23(b).

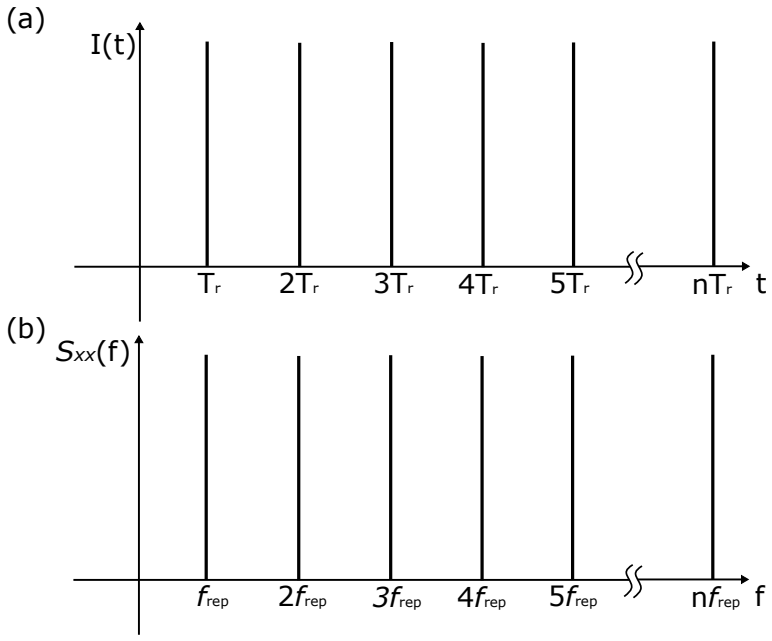

Figure 1.23 – Schematic plot of a pulse train. (a) Intensity in the time domain, and (b) power spectral density in the frequency domain.

Timing jitter

If the time between the pulses is not equidistant, but fluctuates with $\Delta T(t)$, the pulse train is said to suffer from timing jitter. In such a case, the intensity of the

pulse train is given by:

$$I_{\mathrm{p}}(t) = P_{\mathrm{av}} T_{\mathrm{r}} \sum_{n=-\infty}^{\infty} \delta(t - nT_{\mathrm{r}} - \Delta T(t)). \tag{1.45}$$

The corresponding time signal can be seen in Fig. 1.24(a). By making the assumption that $T_r >> \Delta T(t)$, the power spectral density of the disturbed pulse train can be calculated by [59]:

$$S_{\Delta T(t)}(f) = P_{\mathrm{av}}^2 \sum_{n=-\infty}^{\infty} \left(\delta(f - nf_{\mathrm{rep}}) + n^2 4\pi^2 f_{\mathrm{rep}}^2 [\Delta \tilde{T}(f - nf_{\mathrm{rep}})]^2 \right), \tag{1.46}$$

where $\Delta \tilde{T}(f)$ is the Fourier transform of $\Delta T(t)$. Timing jitter is adding sidebands whose magnitudes increase with the square of the mode order n (see Fig. 1.24(b)).

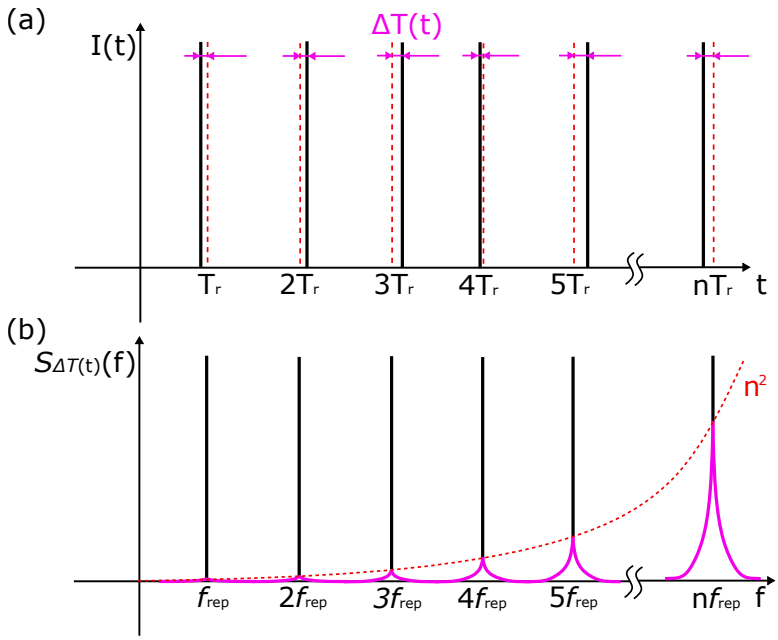

Figure 1.24 – Schematic plot of a pulse train with timing jitter. (a) Intensity in the time domain: the red doted lines corresponds to an unperturbed pulse train; however, due to timing jitter the pulse fluctuate randomly around the ideal position. (b) Power spectral density in the frequency domain. The timing jitter generates side-bands which increase with the square of the mode number.

Intensity noise

Let us consider a pulse train with a variation of power $N(t)$ from pulse to pulse. The intensity of the pulse train will correspond to:

$$I_{\mathrm{p}}(t) = P_{\mathrm{av}} T_{\mathrm{r}} (1 + N(t)) \sum_{n=-\infty}^{\infty} \delta(t - nT_{\mathrm{r}}), \tag{1.47}$$

see Fig. 1.25(a). The power spectral density $S_{xx}(f)$ is then given by [59]:

$$S_{N(t)}(f) = P_{\mathrm{av}}^2 \sum_{n=-\infty}^{\infty} \left(\delta(f - nf_{\mathrm{rep}}) + [\tilde{N}(f - nf_{\mathrm{rep}})]^2 \right), \tag{1.48}$$

where $\tilde{N}(f)$ is the Fourier transform of $N(t)$. The broadening due to amplitude noise affects all spectral radio frequency modes in an equal manner (see Fig.1.23(b)).

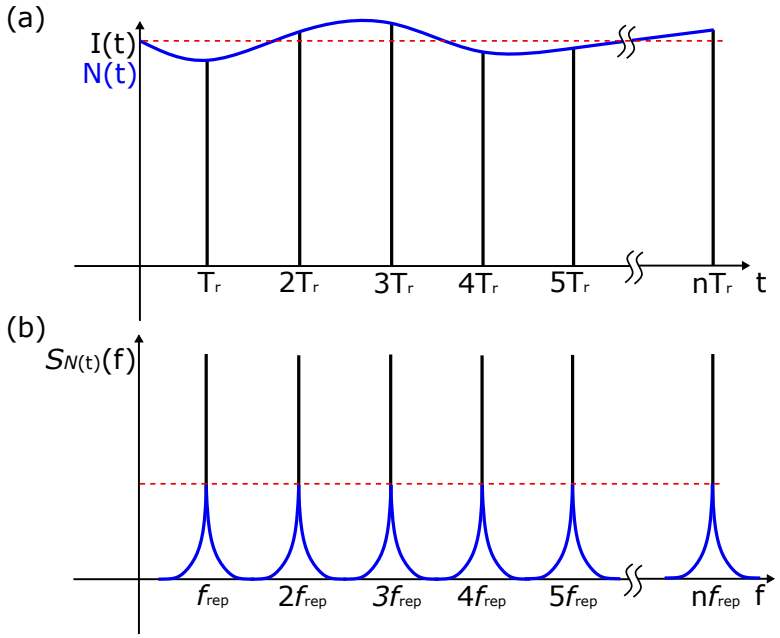

Figure 1.25 – Schematic plot of a pulse train with power fluctuations. (a) Intensity in the time domain: The red doted lines corresponds to an unperturbed pulse train; however, due to amplitude noise the amplitudes of the pulses fluctuate randomly around the average value. (b) Power spectral density in the frequency domain. The power fluctuations generate sidebands which have the same magnitude for all modes.

Stabilizing an optical frequency comb

Stabilizing an optical frequency comb is a challenging task, even though one has to stabilize only the two parameters f_{rep} and f_{ceo}.

The repetition rate f_{rep} is usually stabilized by acting on the cavity length. Equation 1.38 shows that for a comb line f_n in the optical frequency range (100s THz) and a repetition rate in the radio frequency range (MHz-GHz) leads to a value of $n \approx 10^6$. Therefore, any noise on the repetition rate f_{rep} translates into noise on the optical lines via a large multiplicative factor. As a consequence, the stabilization of f_{rep} is very crucial.

The f_{ceo}, on the other hand, enters Eq. 1.38 as an offset and is therefore directly influencing the linewidth of the individual DC lines. Nevertheless, stabilizing the f_{ceo} is an even more complex and difficult task, since it is a not easily accessible parameter. To measure the f_{ceo}, usually so-called self-referencing [4, 5, 61] based on an f-to-f interferometer [62] is used.

The operation principle of an f-to-f interferometer is shown in Fig.1.26.

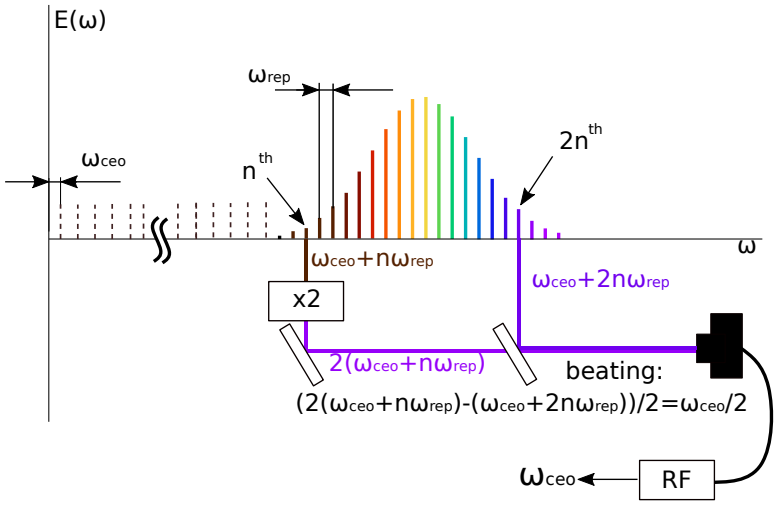

Figure 1.26 – Operation principle of an f-to-$2f$ interferometer.
Please note: $\omega_{\mathrm{ceo}} = 2\pi f_{\mathrm{ceo}}$ and $\omega_{\mathrm{rep}} = 2\pi f_{\mathrm{rep}}$.

The OFC must contain a frequency component f and a frequency component $2f$ perform f-$2f$ interferometry. A comb that fulfills this condition is called octave-spanning OFC. This type of OFC is usually achieved via nonlinear spectral broadening of the initial comb. A section of the light of the OFC with frequency $f = f_{\mathrm{ceo}} + nf_{\mathrm{rep}}$ is frequency-doubled to get $f_{\mathrm{d}} = 2f_{\mathrm{ceo}} + 2nf_{\mathrm{rep}}$ and brought into optical beating with a section of the OFC at twice the frequency $2f = f_{\mathrm{ceo}} + 2nf_{\mathrm{rep}}$. The beating signal of the frequencies corresponds to the f_{ceo}. Details on the experimental implementation of such a setup will be shown in section 3.8 as supplementary material to publication 2.

1.7 Measuring optical spectra with comb tooth resolution

The stability of the frequency comb teeth is the final limitation for the resolution that can be achieved in a spectroscopic experiment involving frequency combs. However, to exploit the full resolution potential of a stabilized frequency comb, the spectral measurement method used in the experiment needs to be able to resolve the individual comb lines. Measuring spectra with a broad spectral coverage at high resolution is a difficult task. Several methods suitable for resolving OFC spectra with comb tooth resolution have been reported so far.

1.7.1 Fourier transform spectrometer

A Fourier transform spectrometer (FTS) is a powerful tool for spectroscopic measurements [10]. The operation principle is based on a Michelson interferometer. A sketch can be seen in Fig. 1.27. Light from a light source is split into two arms by a beam splitter and reflected back by two end mirrors. The reflected light is spatially combined again and sent on a photodiode. One of the end mirrors is mounted on a translation stage. The resolution of the FTS depends on the travel range of the end mirror. To understand the relationship between travel range and resolution, let us consider a monochromatic plane electromagnetic wave coupled into the FTS. The scanning end mirror now delays one arm against the other. The signal on the photodiode is now a convolution of the plane wave with itself. The measured result will be a sinusoidal signal. Let us now consider two input waves with slightly different frequencies. To fully resolve the two waves, the mirror must scan long enough to reach the point where one of the wave reaches its maximum amplitude while the second one reaches its minimum amplitude. Therefore, the resolution is given by the traveling range of the mirror. The resolution f_{min} is given by

$$f_{\mathrm{min}} = \frac{c}{2d}, \tag{1.49}$$

where c is the speed of light. Assuming that we would want to get a resolution of around 10 kHz, which is on the order of a stabilized OFC linewidth, the scanning range of such an FTS would have to be around 15 km. However, by using an OFC instead of a continuous-wave laser, these requirements can be significantly be reduced. By matching the scanning range of the FTS to half of the cavity round-trip length of the laser resonator, the linewidth function of the FTS has a zero crossing exactly at the position of the comb repetition rates [13]. As a result, all points measured correspond to the correct amplitude function of the

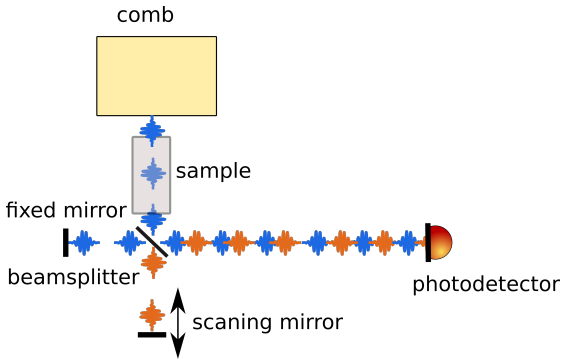

Figure 1.27 – Principle of a Fourier transform spectrometer.

OFC. The resolution in this scenario is not limited by the resolution of the FTS, but by the linewidth of the optical OFC, since the position of the OFC teeth may be scanned arbitrarily. For an OFC with a repetition rate of 100 MHz and a linewidth of 10 kHz, a scanning range of only 1.5 m is needed to achieve a resolution of 10 kHz. The combination of OFCs and FTS is a powerful tool for spectroscopy. However, although a traveling range of 1.5 m is achievable within a laboratory environment, such a setup is rather bulky and thus not particularly suitable for spectroscopic field applications. An additional drawback is the long measurement time caused by the limited scanning speed of the mechanical stage. Furthermore, to get a sufficient signal-to-noise ratio, several sweeps are usually necessary, which extends the measurement time.

1.7.2 Dual-comb spectroscopy

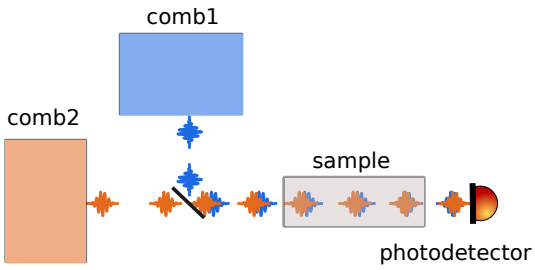

Figure 1.28 – Operation principle of dual-comb spectroscopy.

Dual-comb (DC) spectroscopy [14] is a powerful method to measure optical spectra with high resolution and fast acquisition times over a large optical bandwidth. The operation principle can be seen in Fig. 1.29. Instead of a single OFC, two OFCs with slightly different repetition rates are used. Due to the different repetition rates of the two pulse trains, the pulse trains are mutually scanning each

other. The scanning is similar to the working principle of an FTS, but without any moving delay stage. The scanning duration t_s is given by the difference in repetition rate Δf_{rep},

$$t_s = \frac{1}{\Delta f_{rep}}. \tag{1.50}$$

When the two OFCs are spectrally and spatially overlapping and sent onto a photodiode, the scanning leads to an interferogram. The spectral information can then be retrieved from this time trace via Fourier transform analysis. The principle can also be understood by looking at the frequency domain. Figure 1.29 shows two combs with a slightly different repetition rate. The comb modes next

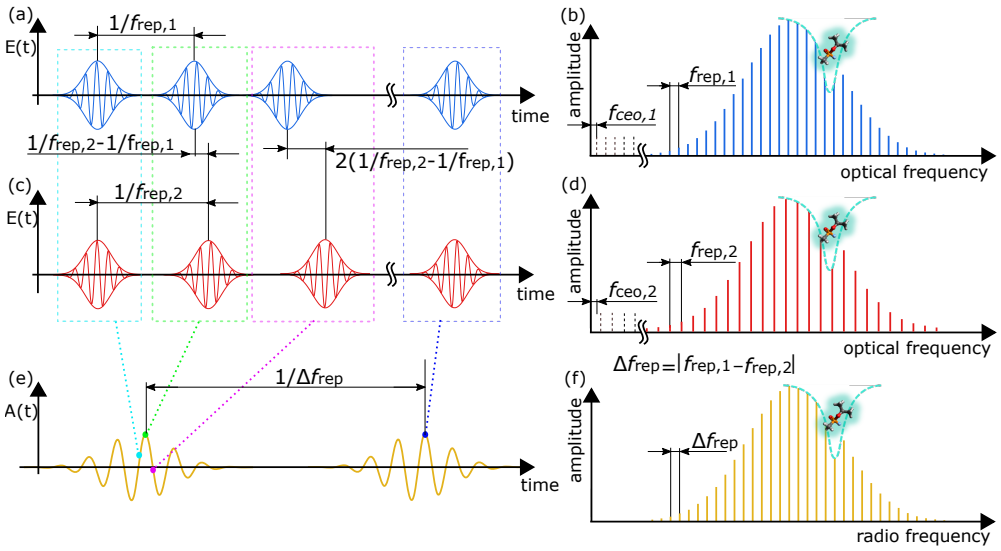

Figure 1.29 – Principle of DCS. Schematic of two OFCs at different repetition rates. The corresponding time-domain interferogram occurs periodically with $1/\Delta f_{rep}$. A (fast) Fourier transform (FFT) of this time-domain interferogram corresponds to the down-converted RF-comb.

to each other start to beat with each other, generating a so-called down-converted OFC in the radio-frequency range, see fig 1.30. The beating frequency is given by the Δf_{rep}. This one-to-one mapping from the optical frequency range down to the radio frequency range, where frequencies are much more easy to measure, is the great advantage of DC spectroscopy. However, two problems are still remaining. The first one is that the down-converted spectrum does not carry information about the center wavelength of the two optical combs, so the spectral position has to be calibrated, for example, by some known absorption lines. The second one is that not only the comb lines next to each other are beating with each other; every line is beating with every line, generating multiple down-converted

radio-frequency combs. If the spectral overlap of the two optical combs is too large compared to the repetition rate and the difference in repetition rates, the different down-converted combs start to grow into each other (optical aliasing), see Fig.1.30. The non-aliasing bandwidth $\Delta\nu$ is given by

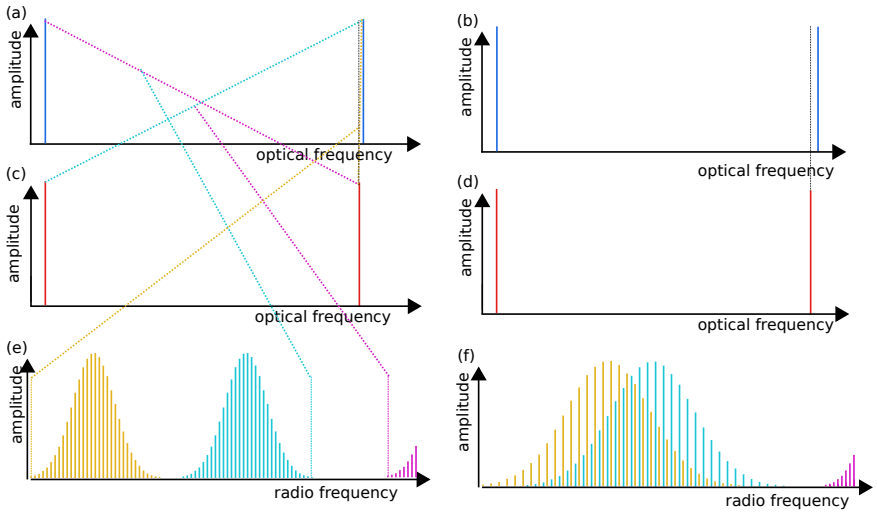

Figure 1.30 – Schematic of the down-conversion of the optical comb lines to the radio frequency comb lines due to optical beating: without (a), and with (b) optical aliasing.

$$\Delta\nu = \frac{f_{\mathrm{rep}}^2}{2\Delta f_{\mathrm{rep}}}. \tag{1.51}$$

The two OFCs have to be stabilized to each other to get mutual coherence. This stabilization can become a complex and difficult task. One very promising method is the use of a single cavity DC, i.e. where both optical OFC emerge from the same laser cavity. Common-mode noise cancellation due to the shared cavity can lead to mutual coherence between the two combs even without any external feedback loops, enabling spectroscopy with free-running optical combs [16, 18].

Chapter 2

Tunable dual-color operation of Yb:fiber laser via mechanical spectral subdivision

"The world will know that free men stood against a tyrant, that few stood against many and, before this battle is over, that even a god-king can bleed"

Leonidas, 300

The publication presented in this chapter was authored by:

JAKOB FELLINGER[1] (laser design, experimental setup, measurements, data evaluation)

GEORG WINKLER[1] (simulations and experimental measurements)

ALINE S. MAYER[1] (experimental measurements)

LAURIN R. STEIDLE[1] (measurements of the laser spectrum)

OLIVER H. HECKL[1] (supervision)

[1] Christian Doppler Laboratory for Mid-IR Spectroscopy and Semiconductor Optics, Faculty Center for Nano Structure Research, Faculty of Physics, University of Vienna, Vienna, Austria

and was published in Optics Express on 13 February 2019.
DOI: https://doi.org/10.1364/OE.27.005478

Preface to publication No. 1

The publication presented in this chapter is based on a self-made NPR mode-locked fiber laser. Since NPR is a well-documented and well-established mode-locking technique for fiber lasers, we took into consideration different NPR-based laser designs as a potential basis for our frequency comb systems during the first part of this PhD project. In order to gain a deeper understanding of the laser dynamics involved in these designs, we performed so-called Knox measurements to characterize the net cavity dispersion.

The Knox measurement scheme is based on a slit that is placed inside the laser resonator at a position where the light is spatially dispersed, see Fig. 2.1(a). This slit is blocking a part of the spectrum and can therefore be used to force the laser to operate at different center wavelengths by laterally translating the slit. The wavelength-dependent pulse repetition rate is recorded and used to calculate the net cavity dispersion. During these measurements, we developed the idea to exchange the slit by a beam block: instead of blocking the "wings" of the spectrum, the center is now prevented from lasing (Fig. 2.1(b) and Fig. 2.2). Thus, the two spectral sections separated by the narrow beam block can start to lase independently. Subsequently, we managed to mode-lock the two independent spectral regions, hence generating two pulse trains out of a single laser cavity. Due to the non-zero intracavity group delay, the two different pulse trains have different repetition rates, which is a prerequisite for the generation of a single-cavity dual-comb based on a dual-color laser.

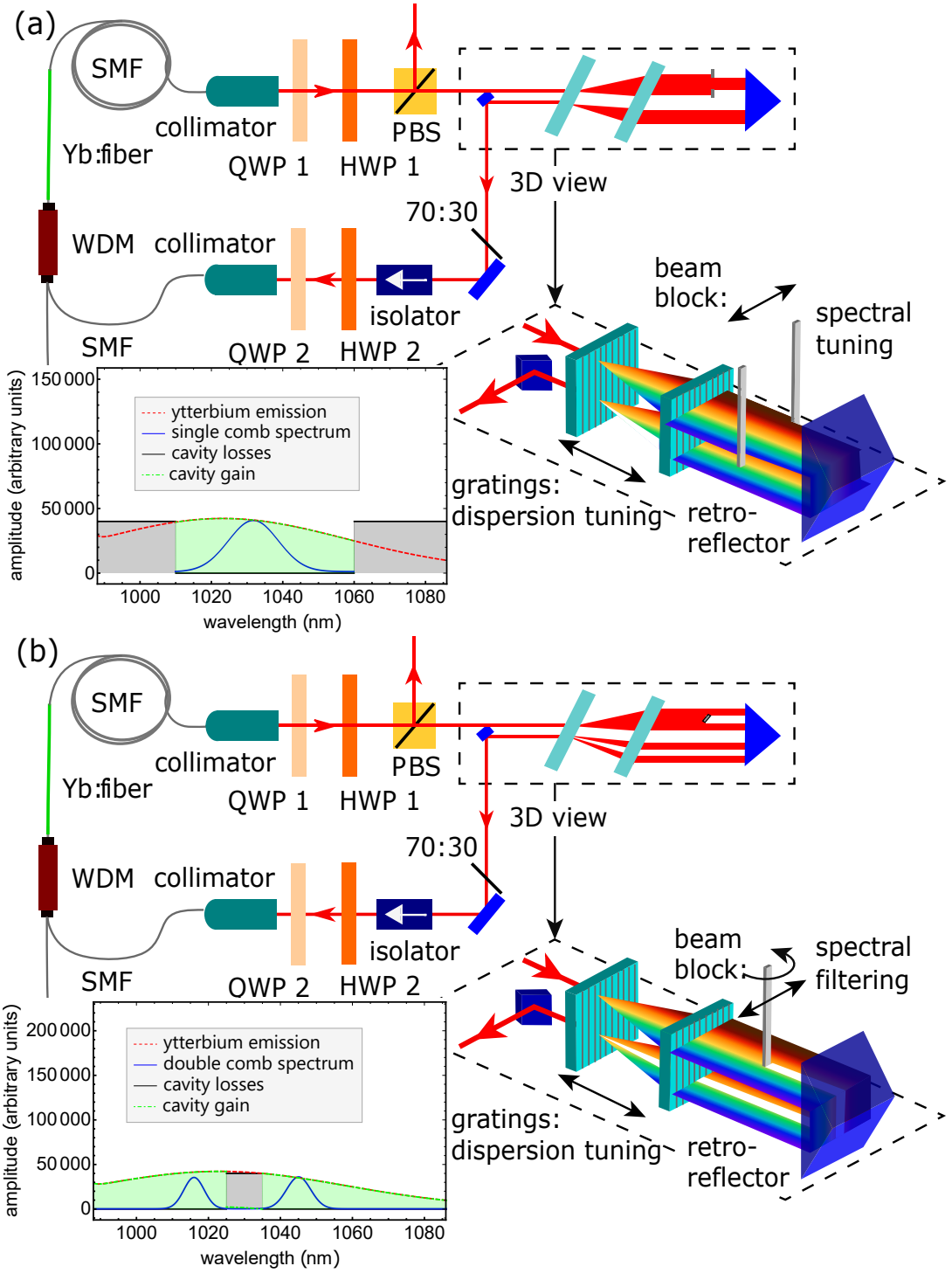

Figure 2.1 – (a) The Knox measurement concept: a movable slit is blocking the wings of the spectral distribution and is used to tune the center wavelength of the pulse. (b) Tunable mechanical filter used to induce dual-color operation: instead of suppressing the spectral wings, the center of the spectrum is now blocked.

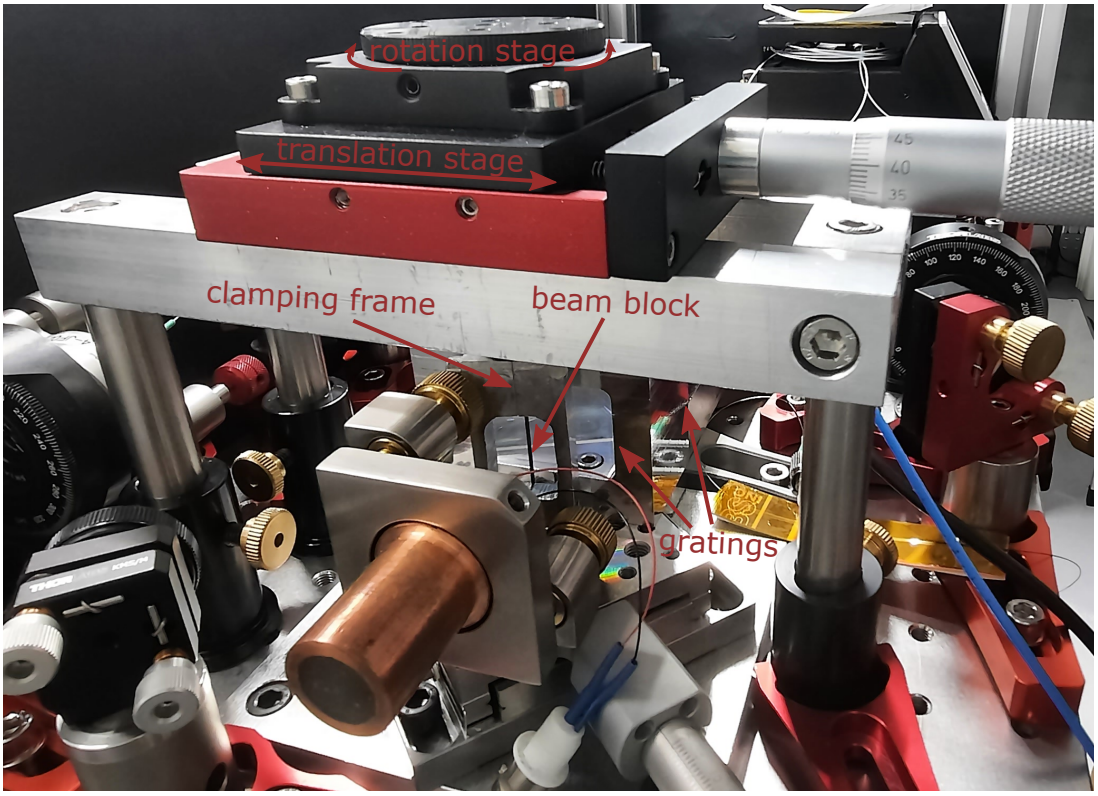

Figure 2.2 – The tunable mechanical spectral filter was implemented by clamping a thin aluminum beam block foil (Thorlabs BKF12 foil) in an aluminum frame. The frame was attached to a rotation stage, which in turn was mounted on a translation stage.

Publication No. 1: Tunable dual-color operation of Yb:fiber laser via mechanical spectral subdivision

Abstract: We present a versatile method to generate a dual-color laser from a single fiber laser cavity by spectral subdivision using a tunable mechanical filter. As a proof-of-principle, we implement the concept in a NPR-mode-locked ytterbium (Yb)-fiber laser. The division into two independent spectral regions is achieved by inserting a narrow blade-shaped beam block into the free-space grating compressor section of the cavity, where the spectrum is spatially dispersed. By mode-locking both spectral regions, two pulse trains with different repetition rates around 23 MHz are generated. Each pulse train has a FWHM of 10 nm. The method presented here enables tuning of the difference in repetition rate as well as the spectral separation of the two independent pulse trains. The difference in repetition rates originates from intracavity dispersion and can be tuned over a large range (650 Hz-3 kHz in this setup) by changing the length of the grating compressor. By changing the effective width of the beam block the spectral separation can be dynamically adjusted. This approach's simplicity holds great promises for the development of single-cavity dual-comb lasers featuring tunable sampling rates.

2.1 Introduction

Since the early 1990s passively mode-locked fiber lasers have become an essential part of laser systems used for industrial, medical, and research applications [63]. A large selection of fiber components is now commercially available, facilitating the rapid evolution of research on fiber lasers and the expansion of their applications. One of the most recent developments is passively mode-locked dual-color and dual-comb fiber lasers. These devices combine the robustness of fiber laser technology with the high passive mutual coherence that is achieved due to common mode noise suppression when both combs are generated within the same cavity. Such systems are ideal for applications such as DC spectroscopy; a versatile technique combining the advantages of conventional broadband spectroscopy and tunable

laser spectroscopy [15]. DC spectroscopy eliminates the need for complicated and expensive detector assemblies such as virtually imaged phase arrays [11] or Fourier transform spectrometers [10], since the optical spectra are down-converted to the radio-frequency range and can hence be detected using simple photodiodes and a radio frequency (RF) analyzer. DC systems traditionally consist of two separate mode-locked lasers delivering pulse trains with slightly different pulse repetition rates. In the spectral domain, those pulse trains correspond to two frequency combs with slightly different comb line spacing, which leads to the generation of a beating comb in the RF range. In order to ensure mutual coherence between the two optical combs, the lasers need to be actively stabilized to each other, which can quickly become a complex and cumbersome task. Much effort has been spent to reduce the complexity of DC setups, for example by phase-locking the two frequency combs to an external cavity diode laser [64] and using adaptive sampling techniques [65–68].

One of the most promising approaches to significantly simplify DC setups is the generation of two pulse trains using a single laser cavity. The passive mutual coherence leads to common-mode noise cancellation in the down converted RF-comb [69], which represents a clear advantage over actively locked systems [18]. Examples of such single-cavity DC schemes involve the separation of the pulse trains by direction of travel [16, 70] polarization [71, 72] or branched optical paths using a birefringent crystal [18, 69] and most recently dual-color fiber lasers [17, 73, 74]. Due to their robustness, all-fiber single cavity dual-color/dual-comb lasers are promising candidates to enable spectroscopic measurements outside the laboratory, thus making them the subject of ongoing studies. In the last few years, many different ways to implement a dual-color fiber laser were reported [75–78]. Zhao et al. described a carbon nanotube mode-locked dual-color erbium doped fiber laser [77]. In their case, dual-color operation was induced by using polarization dependent filtering and wavelength dependent birefringence while exploiting the gain profile of erbium doped fibers, which exhibits two spectrally separated peaks under certain pumping conditions. The approach used by Zhao et al. to generate a dual-comb out of a dual-color laser was to split the two pulse trains outside of the laser cavity, then to amplify them, broaden them inside a nonlinear fiber to generate a spectral overlap and spatially overlap them again, hence obtaining a fully coherent down-converted comb [17]. Subsequently, Liao et al. have presented a thulium-doped dual-color dual-comb laser extending this technique deeper into the mid-infrared spectral region [73]. The thulium laser was mode-locked using a nonlinear NALM. Dual-wavelength operation was implemented by using the artificial gain filter effect induced by the NALM. Spectral overlap was generated

similarly to [17] by nonlinear broadening outside of the cavity [73]. More recently, a further step towards a system for fieldable spectroscopy has been taken by Li et al. [79]. They developed an all-polarization-maintaining dual-wavelength mode-locked erbium fiber laser, where dual-wavelength operation was ensured using a Sagnac loop filter. All dual-color laser schemes mentioned above were designed for specific types of laser oscillators. A more general way to generate a dual-color laser is the implementation of spectral filtering in the laser cavity by using fiber Bragg gratings with different transmission wavelengths. Reported results achieved with this technique reached up to triple-wavelength operation centered around 1550 nm with a FWHM of about 0.5 nm with a repetition rate < 7 MHz [80]. Although this method seems very promising, the spectral coverage as well as the repetition rate would have to be increased in order to be useful for dual-comb spectroscopy. To get a broader FWHM and a higher repetition rate, the spectral filtering would have to be perfectly matched to the mode-locking dynamics of the laser cavity.

In this work, we present a particularly flexible solution to generate a dual-color laser out of a single laser cavity using a mechanical spectral filter. Mechanical spectral filtering as a method to generate dual-color lasers was first implemented in the early 1990s [81] in titanium sapphire lasers, which have an extremely broad gain bandwidth (450 nm). Knox et al. [82] furthermore used the spatial dispersion in the grating compressor to measure the intra-cavity dispersion by introducing a slit as a spectral filter and forcing the laser to operate in various narrow wavelength bands.

Here, we implement the concept of mechanical filtering in a fiber laser and show its potential to generate a single cavity dual-color laser. The method offers two key features: dynamical adjustment of the spectral separation between the two pulse trains and tuning of the difference in repetition rates. To the best of our knowledge, these features have not been available in previously reported single-cavity dual-color laser schemes. The spectral filtering technique is demonstrated here in a NPE-mode-locked ytterbium (Yb) fiber laser. The outlined technique is however independent of polarization evolution dynamics in the laser and can potentially be implemented in a large variety of different mode-locked lasers, especially also in polarization-maintaining fiber lasers. Our method does not rely on exploiting specific transmission peaks in the laser gain profile and is also independent from other mode-locking dynamics.

2.2 Experimental setup

We have implemented our mechanical filtering concept using a blade-shaped beam block in a NPE-mode-locked Yb-fiber laser. The physics of NPE-mode-locking is well understood and has many implementations; we refer to Chong et al. [83] for an extensive review. The basic principle consists of exploiting intensity-dependent polarization changes inside a non-polarization-maintaining fiber. By manipulating the polarization of the intra-cavity light using wave plates and a polarizer, the laser is set up in a state in which low peak power light (continuous-wave operation) experiences higher losses than high peak power light (pulsed operation), leading to stable ultrafast laser pulse generation. We have built a laser similar to the approach described in [84], consisting of a free-space and fiber section (Fig. 2.3). The fiber section of the laser consists of a wavelength division multiplexer (WDM) for coupling the pump light into the cavity, a 30 cm-long ytterbium-doped gain fiber (LIEKKI Yb1200-4/125) and 8 m of non-PM single mode fiber (SMF) (Thorlabs SM980-5.8-125) enabling the nonlinear polarization evolution. The calculated group delay dispersion caused by the fiber section of the cavity amounts to $\approx 0.16\,\mathrm{ps}^2$. The light is coupled to the free-space section with two collimators. We ensured full control over the polarization by using a quarter-waveplate (QWP) and a half-wave plate (HWP) in front of the collimators and by inserting a polarization beam splitter cube (PBS), which acts as the primary output coupler of the laser (output A in Fig. 2.3).

A Faraday isolator ensures unidirectional operation. A transmission grating compressor is used for dispersion compensation (Wasatch Photonics Gratings, 800 l/mm, angle of incidence 24.3° @ 1030 nm). Inside the grating compressor, the spectral components of the intra-cavity light are spatially dispersed (see Fig. 2.3). We block a narrow part of the spectrum by introducing a small razor blade into the collimated beam section of the grating compressor, thus dividing the spectrum into two broadband regions. We show that it is possible to independently mode-lock the laser within these two spectral regions, hence creating two mode-locked lasers at slightly different repetition rates. Due to the spatial distribution of the spectral components, it is straightforward to manipulate the spectrum by simply translating the beam block. In addition to the position, also the width of the spectral filter can be tuned by rotating the razor blade. The effective width of the beam block can be tuned in this manner from 0.2 mm and 1.5 mm.

The laser operates with a repetition rate around 23 MHz. This rather low repetition rate allows us to maintain sufficient peak power for simultaneous mode-locking of the two different pulse trains. Starting dual-color operation at a higher repeti-

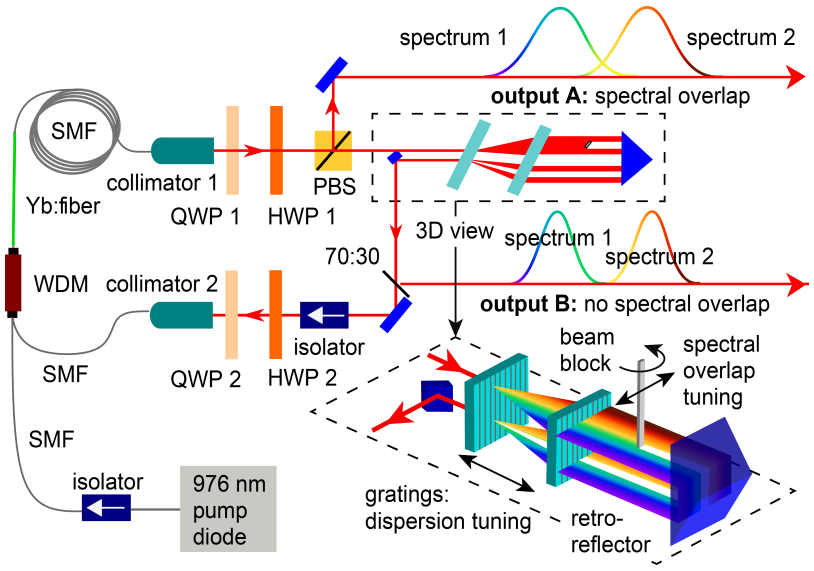

Figure 2.3 – Setup of the single-laser source dual-color cavity. Due to the mechanical spectral filter the laser oscillator emits two pulse trains with different repetition rates and center wavelengths. The optical spectra of the two pulse trains coupled out at the PBS are broadened by self-phase modulation in the fiber portion of the laser cavity.

tion rate would require more than the currently available 300 mW of pump power. However, once started, dual-wavelength operation in the current configuration can be sustained with 80 −100 mW of pump power. Since the gain maximum is situated around 1030 nm, any spectral overlap generated in this spectral region by self-phase modulation prior to the gain fiber will be strongly amplified, leading to competitive behavior between the two spectrally separated pulse trains. To avoid this issue, we kept the length of the single mode fiber between collimator 2 and the WDM (see Fig. 2.3) as short as possible. Adjustment of the wave plates [84] as well as the spectral filter allowed us to achieve independent and simultaneous mode-locking of both spectral regions.

2.3 Results

In Fig. 2.4, we show the optical and the RF spectrum of the light coupled out of the cavity. The optical spectra shown in Fig. 2.4(a) were recorded using a Fourier-transform infrared spectrometer with a resolution of 0.3 nm. The spectra were measured at two different locations in the setup (see Fig. 2.3): the solid line corresponds to output A (after the single mode fiber), while the dashed spectrum was measured at output B, i.e. directly after the spectral filter. At output B, the p-polarized light is coupled out using a pellicle beam splitter (Thorlabs BP145B3).

The pellicle has a reflectivity that increases from 22% at 1010 nm to 31% at 1050 nm. The remaining light then propagates through the Faraday isolator as well as a HWP and QWP, changing the polarization state of the light from linear (p-polarized) to elliptical before the gain fiber. At output A, the light exits the cavity via a polarizing beam splitter, with an output coupling rate that depends on the exact settings of the wave plates. Compared to the spectrum obtained at output B, the FWHM of the spectrum recorded at output A is broadened by 3 nm and 2 nm for the short-(red) and long (black)-wavelength section respectively. The broadening is induced by self-phase modulation occurring in the fiber section of the cavity.

Figure 2.4(b) shows an RF measurement obtained by simultaneously focusing both pulse trains onto a photodiode. The two repetition rate signals are 1.25 kHz apart in this example (see Fig. 2.6 for tuning results) and show strong signal-to-noise ratio of > 80 dB at 3 Hz resolution bandwidth. In order to verify that each spectral region corresponds to an independent, cleanly mode-locked pulse train, we used an additional grating to spatially separate the two spectral regions outside of the laser cavity (see Fig 2.4(c)). Figure 2.4(d) and (e) show the repetition rates of the single pulse trains and their respective harmonics. The measurement was done with a fast (5 GHz) photodiode.

In Fig. 2.5 we show the temporal drift of the two repetition rates and their difference over 30 min of continuous dual-color mode-locking operation. Note that the system is completely free-running and is neither boxed nor optimized for mechanically stability. The data was recorded using a microwave spectrum analyzer set to 1 Hz resolution bandwidth.

Previously demonstrated single cavity dual-color lasers featured a fixed difference Δf_{rep} between the two pulse repetition rates, which is usually defined by the laser design and cannot be tuned. In our case however, changing the grating spacing (and thus the amount of dispersion) allows us to tune the difference in the repetition rate from 3 kHz down to 650 Hz (Fig. 2.6). The cavity end mirror is mounted on the same stage as the second grating. Changing the grating separation therefore also has an influence on the repetition rates $f_{\mathrm{rep},1}$ and $f_{\mathrm{rep},2}$. Decreasing the grating separation leads to an increase of the repetition rate and to an increase of Δf_{rep}, as it is expected when working in a regime where the net total cavity GDD is positive.

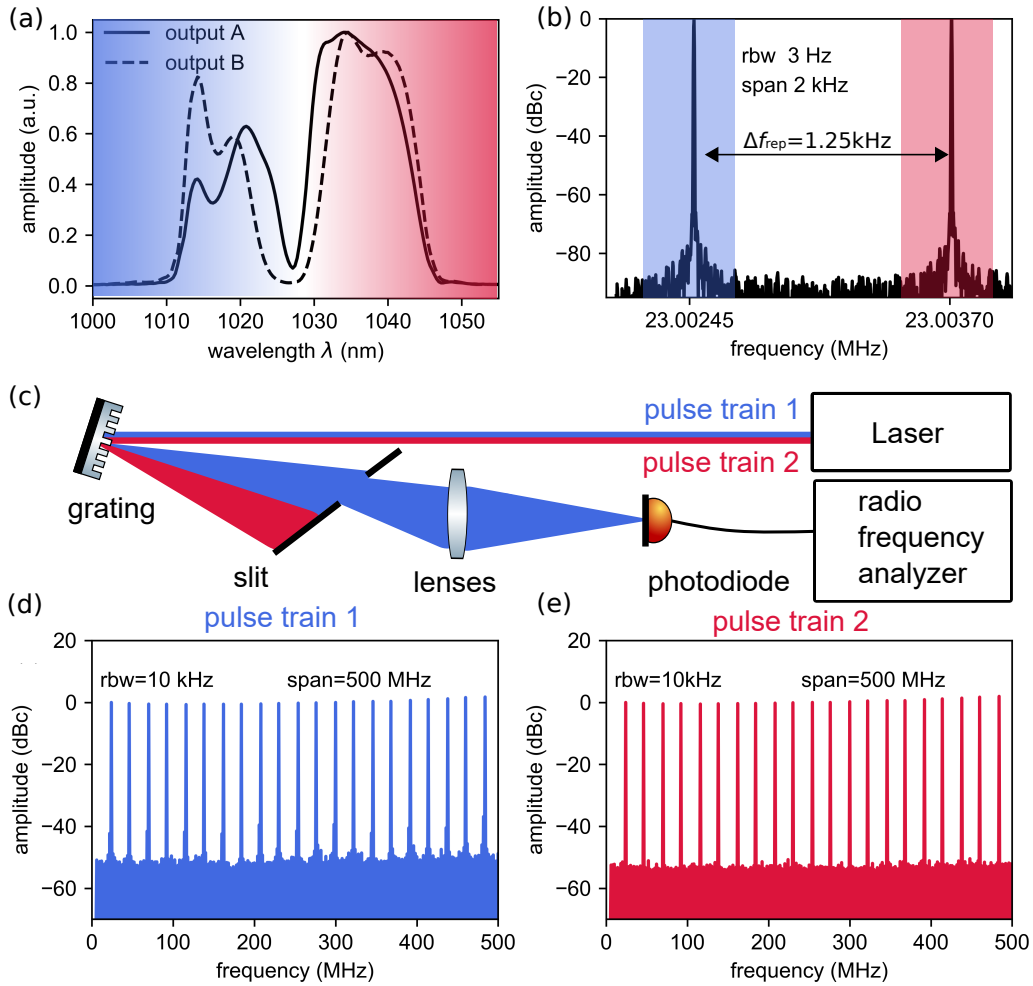

Figure 2.4 – Optical and radio-frequency spectra of the dual-color laser. (a) The dashed line shows the spectrum directly after spectral filtering (output B, see Fig. 2.3), the solid line shows the spectrum exiting the cavity via the polarizing beam splitter (output A, see Fig. 2.3). (b) Radio frequency spectrum around the repetition rates with a span of 2 kHz and a resolution bandwidth (rbw) of 3 Hz. The strong signal (> 80 dB) and absence of side-peaks indicate clean mode-locking for both pulse trains. (c) Schematic sketch for measuring the single pulse trains independently from each other by spectrally separating the two pulse trains using a grating after the cavity output and focusing each pulse train individually on the photodiode while blocking the other one. (d),(e) 500 MHz span showing the repetition rate of the single pulse trains and their respective harmonics.

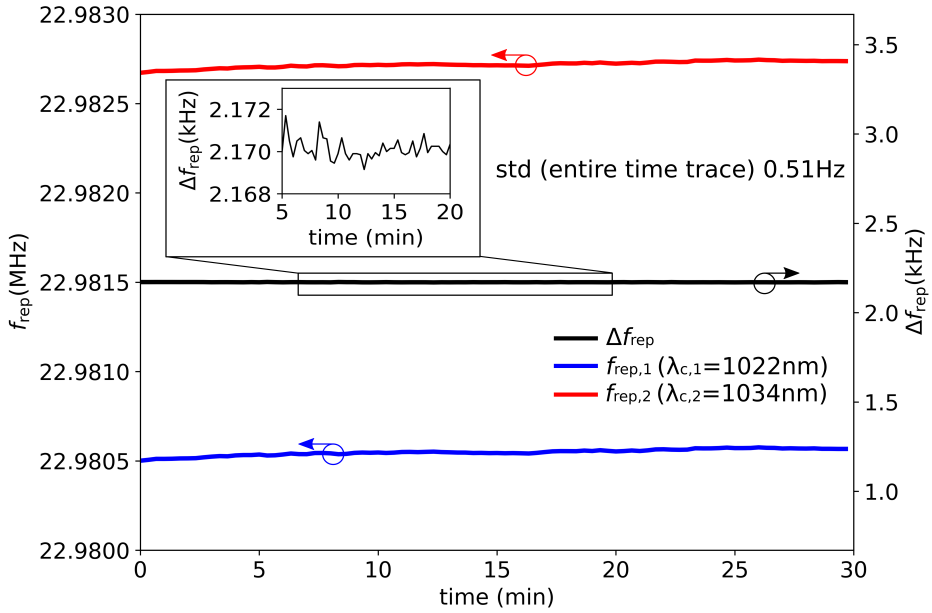

Figure 2.5 – Temporal drift of Δf_{rep}, $f_{\mathrm{rep},1}$ and $f_{\mathrm{rep},2}$ over 30 min. The measurement was recorded with a microwave spectrum analyzer set to a frequency resolution of 1 Hz (1 read-out every 20 s).

The tuning range of the grating separation was limited by the travel range of the translation stage used (± 12.5 mm around the nominal separation of 45 mm) corresponding to an intra cavity dispersion change of ± 41 600 fs^2 around a nominal value of +41 800 fs^2 (total GDD fiber + grating), meaning the complete tuning was done without crossing the zero-dispersion point.

Furthermore, by rotating the beam block, which is equivalent to changing its thickness, we were able to vary the width of the spectral cut between the two individually mode-locked spectra, see Fig. 2.7. Although the grating separation is kept constant, we observe a slight change in Δf_{rep} of 120 Hz between the configuration with the narrowest blade width (Fig. 2.7, blue curve) and the widest (Fig.2.7, red curve) caused by the central wavelength shifts. Ultimately, the spectral tuning is limited by the bandwidth of the gain medium, in our case the Yb:fiber, whose emission and absorption spectra have been included in Fig.2.7 for comparison.

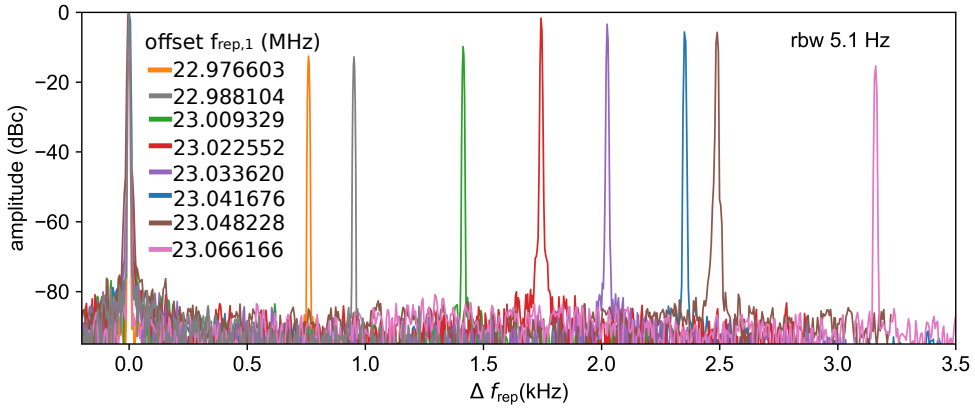

Figure 2.6 – Tuning of $\Delta f_{\mathrm{rep}} = f_{\mathrm{rep},1} - f_{\mathrm{rep},2}$ by changing the grating separation, with $f_{\mathrm{rep},1}$ being set to zero in all data sets for straight-forward comparison. The offset values corresponding to the values of $f_{\mathrm{rep},1}$ for each configuration are listed in the legend.

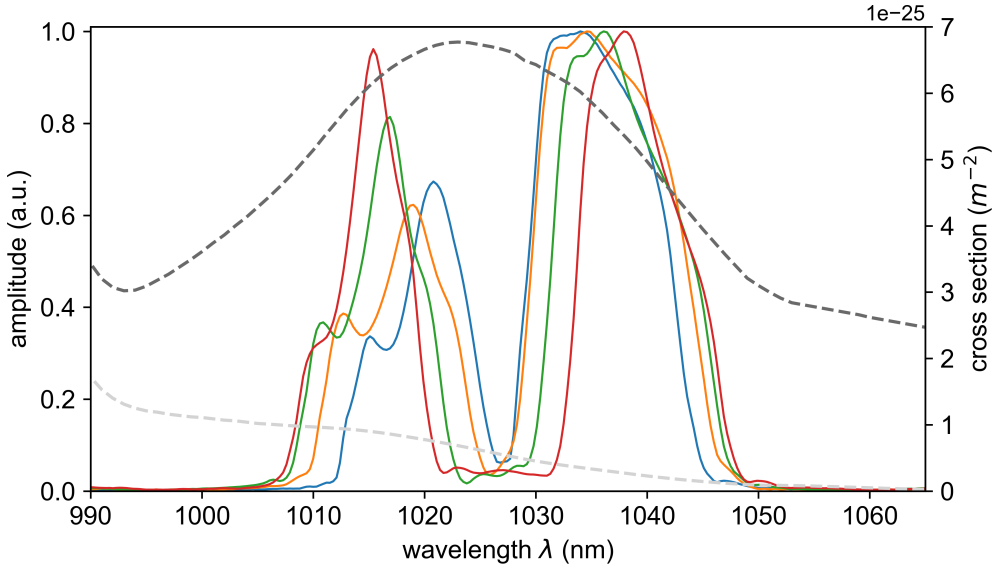

Figure 2.7 – Tuning of the spectral separation by rotation of the razor blade, which corresponds to changing the effective width of the beam block from 0.2 mm to 1.5 mm.

2.4 Prospects for dual-comb generation

The intra-cavity broadening due to self-phase modulation mentioned in the previous paragraph may be usable to generate a dual-color dual-comb without any external spectral broadening. However, to achieve an aliasing-free down-converted radio frequency comb, the spectral overlap $\Delta\nu$ needs to be chosen in order to fulfill the following condition [14]:

$$\Delta\nu = \frac{f_{\mathrm{rep},1}^2}{2\Delta f_{\mathrm{rep}}}. \tag{2.1}$$

With a nominal repetition rate $f_{\mathrm{rep},1}$ around 23 MHz, a difference between the two repetition rates of $\Delta f_{\mathrm{rep}} = 1\,\mathrm{kHz}$ and a center wavelength of 1025 nm, the non-aliasing dual-comb spectral bandwidth is calculated to be currently about 0.26 THz, corresponding to only 1 nm at a center wavelength of 1025 nm. By increasing the nominal repetition rate (which implies supplying more pump power) this issue can be avoided.

Furthermore, nonlinear interactions between the two pulse trains can occur inside the fiber-part of the cavity. This type of intra-cavity dynamics has been studied recently using dispersive Fourier transform technique in a dual-color soliton mode-locked erbium fiber laser [85]. The intra-cavity pulse collision may cause a spurious signal in the recorded dual-comb interferogram. However, this signal can be separated from the center burst using a delay stage as described by Liao et al. [73].

2.5 Conclusion and outlook

We have demonstrated a versatile and easily implementable method to generate a dual-color mode-locked laser from a single fiber laser cavity. By manipulating the cavity losses for the center part of the gain spectrum using a mechanical spectral filter, we obtained two pulse trains with slightly different repetition rates originating from the same laser cavity. In our experiment, the spectral filtering was implemented in a NPE laser cavity by introducing a beam block in the collimated beam section of the grating compressor. By changing the grating spacing, the difference of the repetition rates could be tuned in the range of 650 Hz to 3 kHz. Although a NPE laser was used in this demonstration, the polarization evolution is not part of the dual-color laser generation process (in contrast to other schemes using the polarization as a selection criteria to generate two pulse trains [17, 73, 77]). The spectral filtering itself may be extended to lasers

without a grating or prism compressor by using fiber Bragg gratings or dielectric coatings. Hence, we believe that the method presented here can be extended to basically any kind of passively mode-locked fiber laser, including state-of-the-art all-polarization-maintaining configurations, provided that the gain bandwidth is large enough to support two spectrally distinct pulses. The demonstrated scheme is not limited to any specific wavelength region; in particular, it is applicable to the mid-infrared, where compact dual-comb setups for molecular spectroscopy are strongly desired for many applications.

Funding

Austrian Federal Ministry of Science, Research and Economy and the National Foundation for Research, Technology and Development.

Acknowledgment
The authors would like to acknowledge Gar-Wing Truong and Garrett Cole for fruitful discussions and helpful comments on the manuscript.

Chapter 3

Flexible all-PM NALM Yb:fiber laser design for frequency comb applications: operation regimes and their noise properties

"Dear Lord, I don't even know where to begin!"

Katherine Johnson, Hidden Figures

The publication presented in this chapter was authored by:

ALINE S. MAYER[1] (noise measurements and data evaluation, transmission function calculations, CEO detection)

WILFRID GROSINGER[1] (Knox measurements and laser characterisation)

JAKOB FELLINGER[1] (laser development, noise measurements, transmission function calculations, supervision of Wilfrid Grosinger)

GEORG WINKLER[1] (experimental measurements)

LUKAS W. PERNER[1] (numerical line-width calculations)

STEFAN DROSTE[2] (laser development)

SARPER H. SALMAN[2] (laser development)

CHEN LI[2] (laser development)

CHRISTOPH M. HEYL[2,3] (supervision)

INGMAR HARTL[2] (supervision)

OLIVER H. HECKL[1] (supervision)

[1] Christian Doppler Laboratory for Mid-IR Spectroscopy and Semiconductor Optics, Faculty Center for Nano Structure Research, Faculty of Physics, University of Vienna, Vienna, Austria

[2] Deutsches Elektronen-Synchrotron DESY, 22607 Hamburg, Germany

[3] Helmholtz-Institute Jena, 07743 Jena, Germany

and was published in Optics Express on 10 June 2020.
DOI: https://doi.org/10.1364/OE.394543

Preface to publication No. 2

Since NPR mode-locking is based on the nonlinear polarization evolution of light inside the optical fiber, the latter is usually not polarization-maintaining. The fact that the fibers do not maintain the polarization makes this type of laser susceptible to environmental perturbations. If any environmental condition slightly changes, the laser will change its operation behavior and might even stop modelocking. Getting the laser to modelock again with the same performance is not straightforward. This is even more true when it comes to the dual-color operation regime where the right operation conditions must be fulfilled for two separate pulse trains. On normal summer days, we happend to observe temperature fluctuations of 3°C in our laboratory. Since the reproducibility of the NPR laser performance is compromised under such circumstances, we decided to re-evaluate our choice of modelocking technique in order to surpass this roadblock. A major increase in robustness can be achieved by the use of polarization-maintaining fibers. In collaboration with the photonic science-department of the German Electron Synchrotron (DESY) under Ingmar Hartl's supervision, we thus decided to take a closer look at a recently proposed PM-fiber laser design termed "figure-9" laser [57]. The results of this endeavor are presented in the following paper.

Publication No. 2: Flexible all-PM NALM Yb:fiber laser design for frequency comb applications: operation regimes and their noise properties

Abstract: We present a flexible all-polarization-maintaining mode-locked Yb:fiber laser based on a nonlinear NALM. In addition to providing detailed design considerations, we discuss the different operation regimes accessible by this versatile laser architecture and experimentally analyze five representative mode-locking states. These five states were obtained in a 78-MHz configuration at different intracavity GDD values ranging from anomalous ($-0.035\,\mathrm{ps}^2$) to normal ($+0.015\,\mathrm{ps}^2$). We put a particular focus on the characterization of the intensity noise as well as the free-running linewidth of the carrier-envelope-offset (CEO) frequency as a function of the different operation regimes. We observe that operation points far from the spontaneous emission peak of Yb ($\approx$1030 nm) and close to zero intracavity dispersion can be found, where the influence of pump noise is strongly suppressed. For such an operation point, we show that a CEO linewidth of less than 10-kHz at 1 s integration can be obtained without any active stabilization.

3.1 Introduction

Over the past years, the performance of low-noise mode-locked fiber lasers has undergone tremendous progress [43, 63]. The growing number of applications of mode-locked lasers in various fields of science is fueling the development of affordable sources that are robust, reliable and can be operated hands-off by people who are not necessarily specialized in laser science. Fiber lasers offer many advantages in that respect: for common gain media such as ytterbium (Yb)- and erbium (Er)-doped glass fibers, pump light from low-cost 976/980-nm-semiconductor diode lasers can be delivered to the gain fiber through all-fiber components, thus avoiding pump misalignment. The large surface-to-volume ratio of optical fibers eases thermal management and even long oscillator cavities can be spooled to fit onto

very small footprints. However, the robustness and reliability is also affected by the type of mode-locking mechanism used. In particular, lasers based on non-polarization-maintaining (non-PM) fibers tend to be very sensitive to environmental perturbations such as temperature changes, humidity or mechanical stress. Nevertheless, mode-locking based on NPR [49–51] in such fibers has been one of the most common techniques to achieve pulsed operation, as it is simple to implement with off-the-shelf optical components and allows for a large flexibility in cavity design.

The use of PM fibers significantly increase the robustness against environmental effects. In order to achieve mode-locking based on NPE with PM fibers, techniques such as cross-splicing have been successfully demonstrated [86–90]. Real saturable absorbers can also be used to mode-lock lasers based on PM fibers: examples include semiconductor SESAM [47, 48], graphene [91, 92], carbon nanotubes (CNT) [93–95], or topological insulators [96, 97]. However, the complexity of designing and fabricating such saturable absorber structures and their tendency to degrade over time often hinders their wide-spread implementation.

Another way of achieving mode-locking in PM fibers consists of using a nonlinear optical loop mirror (NOLM) [52] or nonlinear amplifying loop mirror (NALM) [53]: these devices are based on the superposition of two waves counter-propagating in a fiber loop that can be formed by connecting the output ports of a conventional fiber coupler. The transmission/reflection of the loop mirror depends on the difference in nonlinear phase shift $\Delta\phi_{\mathrm{nl}}$ between the two counter-propagating pulses. Since the nonlinear phase shift is intensity-dependent, these devices can act as saturable absorbers and thus support mode-locking if the NOLM/NALM is implemented such that the total laser cavity round-trip losses drop as soon as $\Delta\phi_{\mathrm{nl}}$ deviates from zero. In a NOLM, the difference in phase shift can be generated by simply having a non-50:50 splitting ratio at its entrance. In a NALM, $\Delta\phi_{\mathrm{nl}}$ is additionally determined by an amplifying fiber asymmetrically placed inside the loop. The ends of the PM fibers used for the NOLM/NALM can be connected to form a so-called "figure-8 laser" [98–101]. Although mode-locking is possible, achieving self-starting operation is difficult in a standard figure-8 configuration [100, 102], since small deviations of $\Delta\phi_{\mathrm{nl}}$ from zero only lead to small changes in the cavity losses. To solve this challenge, one can introduce a non-reciprocal phase bias [55] in order to have a steeper slope of the loss curve around $\Delta\phi_{\mathrm{nl}} = 0$. The phase bias can be generated by a combination of wave plates and Faraday rotators used in transmission or arranged in the form of a compact reflection module [103]. Recently, it has been shown that an intrinsic phase bias can also be generated by using a 3x3 fiber coupler (instead of 2x2) [104]. Although using a phase bias solves

the self-starting issue, the figure-8 configuration still suffers from other drawbacks: it is difficult to scale towards higher repetition rates (i.e. shorter fiber lengths) and lacks an end-mirror that would allow for repetition rate stabilization with a simple piezo actuator.

Thus, a modification of this scheme has recently been proposed [56, 57], where the NALM is implemented in reflection (i.e. containing a straight arm with a mirror at its end). Due to the straight arm, the scheme has been named "figure-9 laser" and has been demonstrated both with a NALM-entrance featuring a fixed splitting ratio [56, 105, 106], as well as using a variable splitting configuration [57]. The concept was applied to lasers based on Yb-, Er-, as well as thulium-holmium (Tm/Ho)-doped gain fibers [57]. Repetition rates as high as 700 MHz have been demonstrated in an Yb-fiber laser using this type of architecture [107], although a non-PM gain fiber had to be used in this case since a PM-fiber with sufficient doping was not commercially available. Nevertheless, due to the strong bending of the short piece of gain fiber, the authors report almost PM-behavior and thus robust operation. The all-PM figure–9 principle has also shown to be compatible with power scaling: using a large mode area (LMA) Yb:fiber, an average output power of 2 W at 72-MHz repetition rate has been reported [108].

Due to their robustness as well as their reliable and reproducible self-starting behavior, all-PM NALM lasers have rapidly turned into ideal candidates for a large variety of applications where "hands-off" mode-locked lasers are desirable [9]. In particular, they have raised considerable interest as sources of low-noise optical frequency combs: full frequency comb stabilization (i.e. stabilization of both the carrier-envelope offset frequency f_{ceo} and comb repetition rate f_{rep}) has been shown in Er-based configurations [56, 109], whereas f_{ceo}-stabilization has also been reported in an Yb-based system [110, 111]. Furthermore, even all-PM NALM-based dual-comb configurations have been demonstrated, where the two pulse trains are generated within the same laser cavity [3, 73, 79]. In our own work on an all-PM NALM dual-comb system [3], we made the interesting observation that these two pulse trains could actually each run in different intracavity dispersion regimes simultaneously.

These promising results prove that the concept of all-PM NALM is very versatile. However, they also reveal the current lack of a systematic overview of the large parameter space that can be accessed already with a single-comb system.

Here, we will provide practical guidelines for the design and operation of an all-PM NALM mode-locked laser based on Yb in particular and will discuss how to leverage the degrees of freedom to find low-noise operation points.

The paper is organized as follows: In section 3.2, we will discuss detailed cavity

design considerations that simultaneously allow for reliability and flexibility. In section 3.3, we present in-situ cavity dispersion measurements to map the operation regions of the laser. In section 3.4, we show five representative mode-locking (ML) states obtained in our 78-MHz Yb:fiber configuration, before comparing their free-running comb noise properties (amplitude noise, timing jitter and linewidth of the offset frequency) in section 3.5 and 3.6. We will show that operation points far from the spontaneous emission peak of Yb situated at ≈1030 nm and close to zero intracavity dispersion can be found, where the influence of pump noise is strongly suppressed. In such a regime, we show that the free-running CEO linewidth can be lower than 10 kHz at 1 s integration time. The sub-10-kHz linewidth presented here rivals the performance reported for non-monolithic solid-state lasers with comparable repetition rates [112]; sub-1-kHz free-running CEO linewidths have so far only been reported for an ultra-low noise fully monolithic 1-GHz solid-state laser [113].

3.2 Laser setup and mode-locking principle

3.2.1 Laser setup

The laser used for our experimental study is depicted schematically in Fig. 3.1(a) and a detailed list of its components can be found in Table 3.1. The cavity consists of a PM NALM fiber part comprising the Yb-doped gain fiber and a free-space linear section consisting of polarization optics and a grating compressor. The geometrical length of the free-space part from the tip of the collimator lens to the silver end mirror amounts to ≈21 cm. The ends of the PM single-mode fiber forming the NALM-loop are twisted by 90° and directly attached to a birefringent beam combiner element, which also contains an integrated collimation lens (see Table 3.1 for details). Light exiting the collimator passes through a 45°-Faraday rotator, a quarter-wave plate (fast axis angle θ_q) and a half-wave plate (θ_h) before impinging on a beam splitter cube (PBC). The transmitted light (p-polarized after the PBC) is rotated by a second half-wave plate (θ_o) and subsequently sent through a grating pair. A flat silver mirror is placed after the grating pair to end the free-space section and reflect the light back into the fiber loop.

Table 3.1 – List of components used for the 78-MHz all-PM NALM Yb:fiber laser.

Component	**Description**
Gain fiber	41.5 cm PM Yb-doped single-mode silica fiber (CorActive Yb-401-PM)
Pump diode	976 nm, Fiber-Bragg-Grating (FBG)-stabilized, max. 900 mW (Thorlabs BL976-PAG900)
Pump/Temperature controller	Thorlabs CLD1015, temperature set to 25.0°C
Pump isolator	Operation range: 976 ± 10 nm, PM 980 fiber, fast axis blocked, max. average optical power 2 W (AFR HPMI-976-02-N-B-QF-1-C)
Wavelengtah division multiplexer (WDM)	Pass band 980 ± 10 nm reflection band 1060 ± 40 nm,, max. optical power (cw): 3W (AFR PMFWDM-9806-N-B-Q)
Single mode PM fiber	Corning PANDA PM980
Beam combiner with integrated collimation lens	Specified operation range: 1030 ± 10 nm polarization aligned to slow axis at both ports, specified output beam waist position (from lens tip): 100-150 mm, collimated beam diameter ($1/e^2$): 0.9 mm, max. optical power (cw) 3W (AFR Semi-PBCC-03-09-N-B-Q)
Faraday rotator	Rotation @ 1030 nm: 45° ± 0.5° rotator (EOT HP-05-R-1030)
Waveplates	$\lambda/2$: Thorlabs WPH05M-1030, $\lambda/4$: Thorlabs WPH05M-1030
Polarizing beamsplitter cube (PBC)	Operation range: 900-1300 nm, Thorlabs PBS103
Gratings	1000 lines/mm, angle of incidence (Littrow) 31.3°, diffraction efficiency for s-and p >94%, (LightSmyth T-1000-1040-3212-94)
End mirror	Silver mirror (Thorlabs PF10-03-P01)

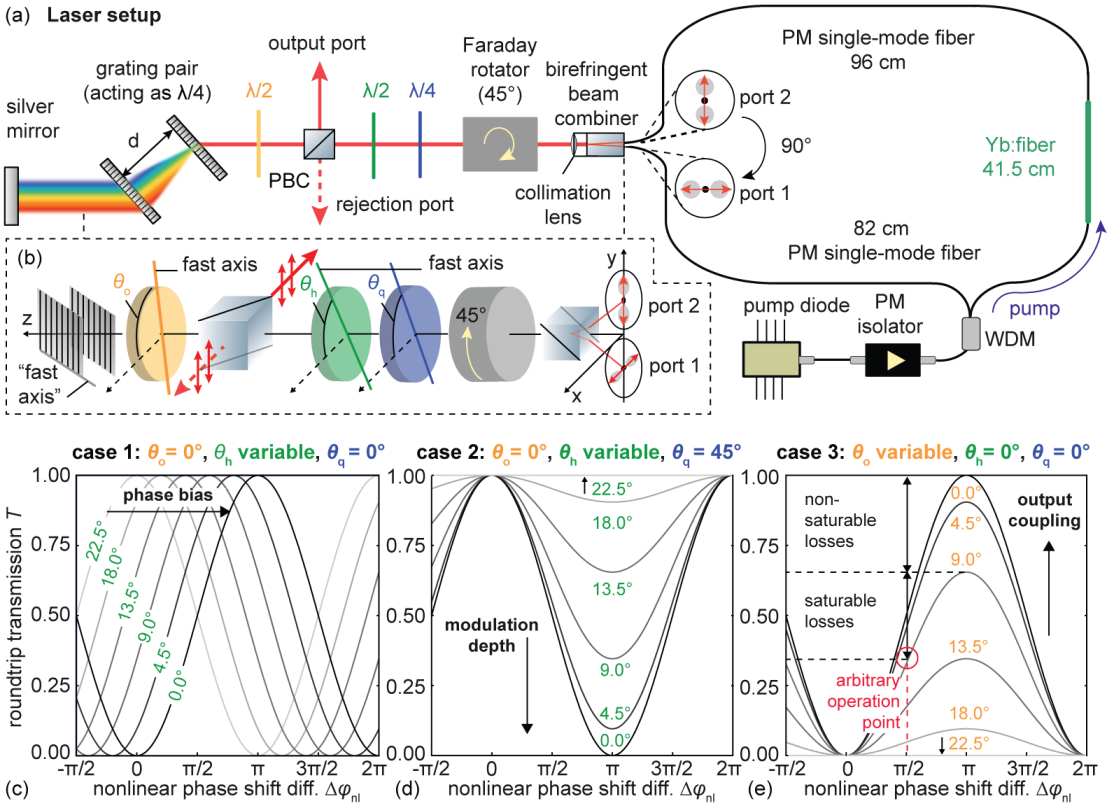

Figure 3.1 – (a) All-PM laser setup featuring a NALM-fiber loop and a free-space section for dispersion control and flexible phase bias/modulation depth/output tuning. (b) Orientation of the polarization-controlling elements in three-dimensional space. (c)-(e) Roundtrip cavity transmission function $\mathcal{T}$ as a function of the nonlinear phase shift difference $\Delta\phi_{\mathrm{nl}} := \phi_{\mathrm{nl},1} - \phi_{\mathrm{nl},2}$, where $\phi_{\mathrm{nl},1}$ is the nonlinear phase accumulated by wave 1 (port 1→ port 2) and $\phi_{\mathrm{nl},2}$ by wave 2 (port 2→ port 1). Three exemplary wave plate settings are depicted: (c) Case 1 (θ_{q}=0°) corresponds to a configuration where tuning the angle θ_{h} only changes the phase bias, but not the modulation depth. (d) Case 2 (θ_{q}=45°) represents the other extreme, i.e. a setting where tuning the angle θ_{h} only changes the modulation depth, but not the phase bias. (e) Case 3 shows the effect of the second half-wave plate, which acts on the non-saturable/linear losses, i.e. the power obtained at the output port. The power at the rejection port represents the saturable losses, which are minimized in mode-locked operation. By adjusting the three angles θ_{h}, θ_{q} and θ_{o} independently, basically any desired combination of phase bias, modulation depth and output coupling ratio can be reached, thus enabling reliable and repeatable mode-locking for a large range of pump powers and dispersion parameters.

3.2.2 Cavity transmission function

In order to understand how the polarization evolution within the free-space sector affects the losses and thus the mode-locking behavior, it is useful to take a look at the total cavity roundtrip transmission function $\mathcal{T}$. Total transmission (i.e. $\mathcal{T} = 1$) corresponds to a situation where all the light stays within the cavity, while for $\mathcal{T} = 0$, the losses are at their maximum and hence no lasing occurs at all. As mentioned in the introduction, self-starting mode-locked operation is obtained when small deviations of the nonlinear phase shift difference $\Delta\phi_{\mathrm{nl}}$ from zero lead to a large decrease in the losses, i.e. when operating on the slope of the cavity transmission $\mathcal{T}$. The roundtrip transmission function $\mathcal{T}$ can be calculated by expressing the effect of each intracavity element in terms of appropriate Jones matrices [114]. The Jones matrices used in our case are listed in Table 3.2.

We define the nonlinear phase shift as $\Delta\phi_{\mathrm{nl}} := \phi_{\mathrm{nl},1} - \phi_{\mathrm{nl},2}$, where $\phi_{\mathrm{nl},1}$ is the nonlinear phase accumulated by wave 1 (port 1$\rightarrow$ port 2) and $\phi_{\mathrm{nl},2}$ by wave 2 (port 2$\rightarrow$ port 1). Since the gain fiber is placed closer to port 1, coupling the same amount of light into both ports will result in $\Delta\phi_{\mathrm{nl}} > 0$. Note, however, that it is possible to obtain $\Delta\phi_{\mathrm{nl}} < 0$ in case significantly less light is coupled into port 1 than into port 2. The smaller the geometrical asymmetry of the loop, the easier it is to flip the sign of $\Delta\phi_{\mathrm{nl}}$. The asymmetry is not only determined by the length ratio of the single-mode fibers on each side of the gain fiber, but also by the pump direction: the beam co-propagating with the pump will experience stronger amplification at the beginning of the gain fiber and will thus accumulate more nonlinear phase in the rest of the gain fiber than the counter-propagating beam. To calculate the exact "break even" point, i.e. the laser operation point at which the splitting ratio compensates a given geometrical asymmetry, one needs to take into account the gain level/gain saturation behavior, which is beyond the model discussed here. The splitting ratio itself, however, can be directly calculated using the Jones matrix formalism (see section 3.2.3).

The wave plate angles stated in this paper are given with respect to the x-axis, i.e. the horizontal axis (see Fig. 3.1(b)). Furthermore, the birefringent beam combiner element is aligned such that the polarization coupled into the loop at port 1 is parallel to the x-axis, which also corresponds to the polarization direction of the light transmitted through the PBC. The grating pair is oriented such that the light gets dispersed in the x-z-plane.

Table 3.2 – Jones matrices for the intracavity elements.

Component	Jones matrix
Half-wave plate	$M_{\lambda/2}(\theta) = e^{-\frac{i\pi}{2}} \begin{pmatrix} \cos^2\theta - \sin^2\theta & 2\cos\theta\sin\theta \\ 2\cos\theta\sin\theta & \sin^2\theta - \cos^2\theta \end{pmatrix}$
Quarter-wave plate	$M_{\lambda/4}(\theta) = e^{-\frac{i\pi}{4}} \begin{pmatrix} \cos^2\theta + i\sin^2\theta & (1-i)\cos\theta\sin\theta \\ (1-i)\cos\theta\sin\theta & i\cos^2\theta + \sin^2\theta \end{pmatrix}$
Faraday rotator	$M_{\mathrm{F}}(\theta) = \begin{pmatrix} \cos\theta & \sin\theta \\ -\sin\theta & \cos\theta \end{pmatrix}$
PBC (transmission/reflection)	$M_{\mathrm{PBC,trans}} = \begin{pmatrix} 1 & 0 \\ 0 & 0 \end{pmatrix}$, $M_{\mathrm{PBC,refl}} = \begin{pmatrix} 0 & 0 \\ 0 & 1 \end{pmatrix}$
End mirror	$M_{\mathrm{silver}} = \begin{pmatrix} -1 & 0 \\ 0 & -1 \end{pmatrix}$
Fiber loop (i.e. inverting the x-and y-components)	$M_{\mathrm{loop}} = \begin{pmatrix} 0 & 1 \\ 1 & 0 \end{pmatrix}$
Nonlinear phase shift	$M_{\mathrm{nl}}(\Delta\phi_{\mathrm{nl}}) = \begin{pmatrix} e^{i\Delta\phi_{\mathrm{nl}}} & 0 \\ 0 & 1 \end{pmatrix}$

In addition, we experimentally observed that - unless the incoming polarization was perfectly parallel (s-polarization) or perpendicular to the grating lines (p-polarization) - the light would be elliptically polarized after one pass through the grating pair. The gratings are designed by the manufacturer to provide the same diffraction efficiencies for both s- and p polarization (see Table 3.1), but no specifications were available with regards to the difference in phase shift for s- and p. Hence, we experimentally determined the polarization state after a single pass through the grating pair by using an auxiliary, linearly polarized laser beam. Power ratio measurements using a PBC after the grating pair confirmed the following: no change in polarization state for s- or p-polarization, a perfectly circularly polarized beam if the polarization impinges on the grating pair at a 45°-angle and elliptical polarization state otherwise. Hence, we modelled the effect of the grating pair on the polarization state by using the Jones matrix of a quarter-wave plate with its fast axis being parallel to the x-axis. The intracavity electric field after roundtrip $\vec{E}^{\mathrm{rt}}_{\mathrm{intra}}$ can thus be expressed as

$$\begin{aligned}\vec{E}^{\mathrm{rt}}_{\mathrm{intra}}(\theta_{\mathrm{q}},\theta_{\mathrm{h}},\theta_{\mathrm{o}},\Delta\phi_{\mathrm{nl}}) =& M_{\mathrm{PBC,trans}}M_{\lambda/2}(\theta_{\mathrm{o}})M_{\lambda/4(\mathrm{gratings})}M_{\mathrm{silver}}(0^\circ)M_{\lambda/4(\mathrm{gratings})}(0^\circ)\\ & M_{\lambda/2}(\theta_{\mathrm{o}})M_{\mathrm{PBC,trans}}M_{\lambda/2}(\theta_{\mathrm{h}})M_{\lambda/4}(\theta_{\mathrm{q}})M_{\mathrm{F}}(45^\circ)\\ & M_{\mathrm{loop}}M_{\mathrm{nl}}(\Delta\phi_{\mathrm{nl}})M_{\mathrm{F}}(45^\circ)M_{\lambda/4}(\theta_{\mathrm{q}})M_{\lambda/2}(\theta_{\mathrm{h}})\vec{e}_{\mathrm{x}} \qquad (3.1)\end{aligned}$$

where $\vec{e}_{\mathrm{x}} = (1,0)$ is the normalized field vector along the x-axis, i.e. corresponding to the polarization state of the light transmitted by the PBC. The field vectors of the light at the rejection ($\vec{E}^{\mathrm{rt}}_{\mathrm{rej}}$) and the output port ($\vec{E}^{\mathrm{rt}}_{\mathrm{out}}$) are given by similar expressions. The cavity roundtrip transmission $\mathcal{T}$ then simply corresponds to

$$\mathcal{T}(\theta_{\mathrm{q}},\theta_{\mathrm{h}},\theta_{\mathrm{o}},\Delta\phi_{\mathrm{nl}}) = \left|\vec{E}^{\mathrm{rt}}_{\mathrm{intra}}\right|^2, \text{ since } \left|\vec{E}^{\mathrm{rt}}_{\mathrm{intra}}\right|^2 + \left|\vec{E}^{\mathrm{rt}}_{\mathrm{rej}}\right|^2 + \left|\vec{E}^{\mathrm{rt}}_{\mathrm{out}}\right|^2 = 1 \qquad (3.2)$$

In Fig. 3.1(c)-(e), we show the roundtrip transmission $\mathcal{T}$ as a function of the nonlinear phase shift difference for three particularly relevant sets of wave plate angles:

- **Case 1: $\boldsymbol{\theta_{\mathrm{o}}}$ =0°, $\boldsymbol{\theta_{\mathrm{h}}}$ = variable, $\boldsymbol{\theta_{\mathrm{q}}}$ =0°:** In this configuration, changing the angle θ_{h} of the half-wave plate shifts the transmission function without affecting the modulation depth. In other terms, this configuration allows for continuous tuning of the phase bias only.

- **Case 2: $\boldsymbol{\theta_{\mathrm{o}}}$ =0°, $\boldsymbol{\theta_{\mathrm{h}}}$ = variable, $\boldsymbol{\theta_{\mathrm{q}}}$ =45°:** With the fast axis of the quarter-wave plate being at a 45°-degree angle, the half-wave plate now solely affects the modulation depth without changing the phase bias.

- **Case 3: θ_o = variable, θ_h =0° variable, θ_q =0°:** At any arbitrary laser operation point, the momentary total losses consist of saturable losses (the rejection port), as well as linear losses (the output port). The saturable losses are automatically minimized when mode-locked operation is achieved. The half-wave plate placed between the PBC and the gratings provides the freedom to adjust the output coupling ratio (i.e. the linear losses) without affecting the phase bias. Furthermore, it also allows for direct "sampling" of the intra-cavity light instead of only having access to the rejected optical spectrum. Note that replacing the output coupling half-wave plate by a quarter-wave plate would cap the linear losses at a maximum of 25% instead of 100% due to the fact that the grating pair already acts as a quarter-wave plate. In practice, the useful modulation range is of course determined by the amount of intracavity power that needs to be sent back into the fiber loop in order to maintain clean mode-locking at a given pump power.

3.2.3 Splitting ratio

In contrast to other implementations of the figure–9 concept that featured a fixed splitting ratio k at the loop entrance [56, 104, 106, 110], the splitting ratio in our case varies as a function of the wave plate positions. The normalized field vector at the entrance of the loop is

$$\vec{E}_{\text{loop entrance}} = M_{\text{F}}(45^\circ) M_{\lambda/4}(\theta_{\text{q}}) M_{\lambda/2}(\theta_{\text{h}}) \vec{e}_{\text{x}}. \tag{3.3}$$

We define k as the fraction of the light that is coupled into port 1 (polarization along the x-axis), i.e.

$$k = \left| \vec{E}_{\text{loop entrance, x}} \right|^2. \tag{3.4}$$

For case 1 mentioned above (i.e. full modulation depth, but varying phase bias) the splitting factor k is 0.5 for all values of the half-wave plate angle θ_{h}. This 50:50 splitting ratio is due to the fact that after passing through the quarter-wave plate on the way towards the collimator, the light will be elliptically polarized with the major axis of the ellipse being along the x-axis. The Faraday rotator then rotates this ellipse by 45°. Thus, regardless of the ellipticity, the same amount of light will be coupled into both fiber ports whose slow axes are aligned along x and y, respectively. Tuning the quarter-wave plate angle θ_{q} between 0° and 45° will vary k, while also changing the modulation depth. By tuning the splitting ratio k, the loop asymmetry (i.e. the value of $\Delta\phi_{\text{nl}}$) can be influenced without having to change the location of the gain fiber within the loop. Hence, achieving

self-starting mode-locked operation depends much less on the exact position of the gain fiber than in laser designs with a fixed splitting ratio.

3.2.4 Operating the laser

The overall laser cavity configuration as depicted in Fig. 3.1(a) provides access to a vast parameter space. Most degrees of freedom, such as the pump power, the angular position of the wave plates and the grating separation can be precisely set and are thus easily reproducible. The laser configuration presented here however also has a rather large alignment tolerance, i.e. lasing and even clean mode-locking can be obtained with slightly different angular positions of the end mirror. End mirror alignment can in turn have a significant impact on the center wavelength of the output spectrum: in certain mode-locking configurations, particularly in the negative dispersion regime, we have been able to obtain a center wavelength shift of ≈30 nm by slightly tilting the end mirror without losing mode-locked operation. In order to have a reference point for end mirror alignment, we thus have found it most useful to align it at low pump powers such that the lasing threshold is minimized. To find the lowest lasing threshold, it is recommendable to set the quarter-wave plate angle to $\theta_q = 0°$, the half-wave plate angle to $\theta_h = 22.5°$ and the output coupling wave plate angle such that only a small amount is exiting at the output port (i.e. $\mathcal{T} \approx 1$). Once lasing is obtained, the pump power can be ramped up while slowly tuning θ_h. This corresponds to changing the phase bias as depicted in Fig. 3.1(c) (case 1) and will reliably lead to mode-locked operation. Once the laser is mode-locked, fine-tuning can be done using the other wave plates. Since in practice, the phase shifts induced by the wave plates are wavelength-dependent, this fine-tuning can also be used to slightly change the position/shape of the spectra. Once an initial set of optimal parameters has been found, the wave plates do not need to be adjusted anymore and the laser can be mode-locked only by ramping up the pump power.

When the laser itself serves as the object of scientific interest - as it was the case in our study - damage may occur while trying to explore the limits of the parameter space. The pump current threshold value determined as described above can then be used as a fairly reliable indicator of potential damage. Although lasing may still be achieved at higher pump powers, if the lasing threshold cannot be lowered to the original value, mode-locking will usually not be achieved anymore. Damage can occur during the build-up of Q-switching pulses with uncontrollable peak powers. Such pulses are most likely to occur upon a sudden change of cavity losses at large pump powers; the most extreme example being physically blocking the cavity or misaligning the end mirror to the point where feedback of the light into the fiber

loop is momentarily interrupted. In this setup, the WDM was identified as the most vulnerable component. It is worthwhile however to emphasize that, although the fiber loop was re-spliced twice during the course of this study, the different mode-locking states and their performance (including the noise characteristics) were easy to recover even with a freshly spliced fiber loop.

3.3 Dispersion measurements

In this work, we specifically focused on characterizing operation points that lie within different intracavity dispersion regimes. The most straight-forward way to tune the intracavity dispersion in the type of Yb:fiber laser described here is the use of a grating compressor. A rough estimate of the intracavity dispersion can be obtained by summing up the contributions of the individual cavity elements using their respective data sheets. These data, however, often have large tolerances or may only be specified at particular wavelengths. Furthermore, data on the changes in dispersion values as a function of the inversion level in the active gain fiber is usually not available. Here, we explicitly measured the intracavity dispersion for different grating separation settings using a method proposed by Knox [115].

The method relies on inserting a slit in the section of the laser cavity where the optical frequencies are spread out in space, i.e. between the grating compressor and the end mirror (see inset in Fig. 3.2(a)). Once mode-locking has been achieved, the slit is laterally moved in small steps across the beam, thereby acting as a bandpass filter. At each step, the laser output spectrum is recorded using an optical spectrum analyzer (Ando AQ6315A) (Fig. 3.2(a)), while the value of the pulse repetition rate f_{rep} is measured by a photodiode connected to a microwave spectrum analyzer (Keysight PXA N9030B) with its resolution bandwidth set to 3 Hz. To eliminate the influence of small random drifts in repetition rate, the measurement of f_{rep} was repeated 25 times and averaged before moving to the next slit position. We then extract the wavelength/optical angular frequency ω_{c} corresponding to the center of mass of each spectrum and plot the corresponding values of $f_{\mathrm{rep}}(\omega_{\mathrm{c}})$ as shown in Fig. 3.2(b). The wavelength-dependent group delay $T(\omega_{\mathrm{c}})$ values are calculated according to

$$T(\omega_{\mathrm{c}}) = \frac{\partial \phi}{\partial \omega} = \frac{1}{f_{\mathrm{rep}}(\omega_{\mathrm{c}})} \tag{3.5}$$

and fitted with a second-order polynomial (solid black lines in Fig. 3.2(b)).

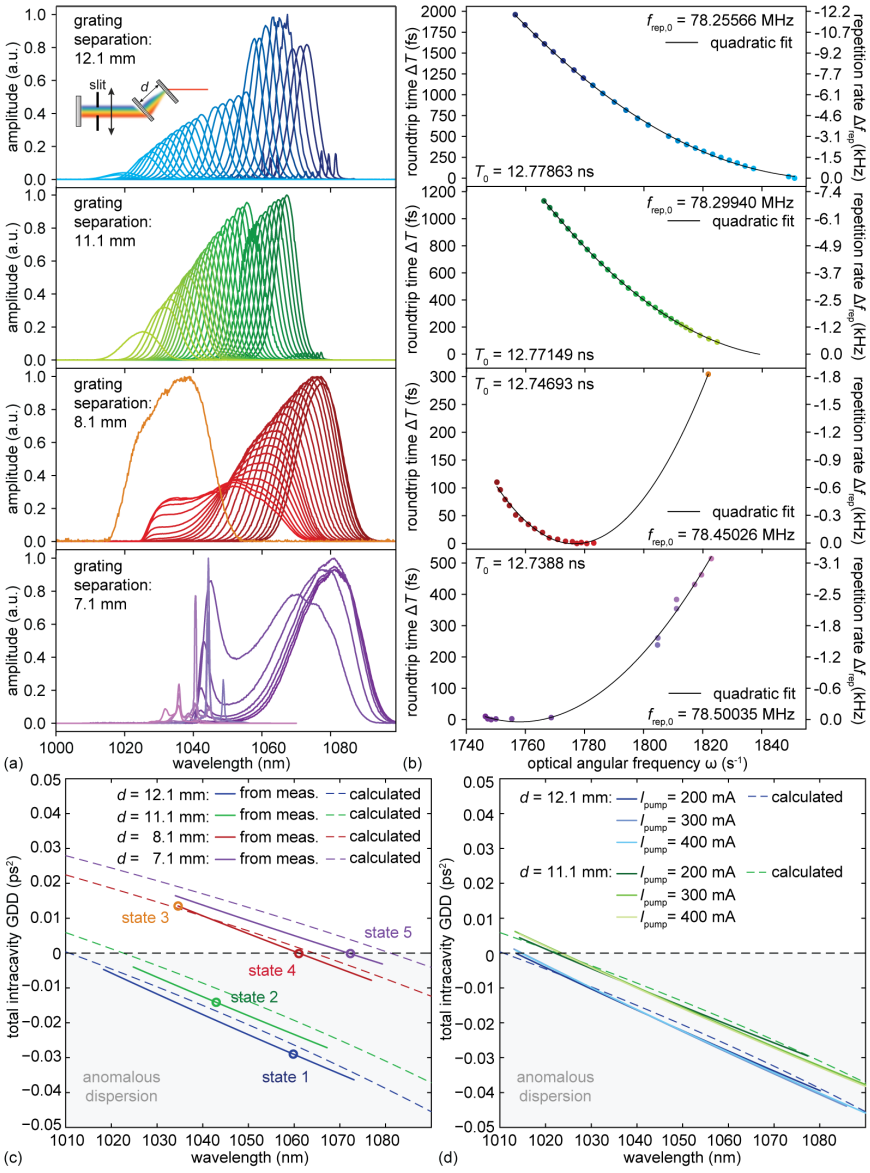

Figure 3.2 – (a) Mode-locked spectra recorded with an optical spectrum analyzer while translating the slit across the beam as shown in the inset. (b) Repetition rate frequency f_{rep} recorded with a microwave spectrum analyzer set to 3 Hz resolution bandwidth (right axis) and corresponding pulse round-trip time/group delay $T = T_0 + \Delta T = 1/f_{\mathrm{rep}}$. The offset values (arbitrarily chosen as the shortest round-trip time/highest repetition rate of the measurement series) have been subtracted for better readability and are stated as annotations in the figure. The black curves are second-order polynomial fits to the group delay values. (c) Solid lines: GDD curves obtained from taking the first derivative of the polynomial fit plotted over the wavelength range where mode-locked spectra were obtained. Dashed lines: calculated dispersion curves. (d) Additional measurement series, where the waveplate positions were kept constant, and only the grating separation was changed.

The first derivative of this fit then yields the GDD

$$\mathrm{GDD} = \frac{\partial^2 \phi}{\partial \omega^2} = \frac{\partial T}{\partial \omega}. \tag{3.6}$$

Note that using a second-order fit for $T(\omega_\mathrm{c})$ corresponds to taking into account second-order (GDD) and third-order (TOD) dispersion, but neglecting higher orders. The obtained GDD-curves are shown as solid lines in Fig. 3.2(c); the wavelength plotting range corresponds to the range over which mode-locking could be sustained during the measurement. For comparison, the dashed lines indicate the calculated GDD-curves obtained from adding the following contributions: gain fiber and the single-mode fiber (data provided by the vendors), Faraday rotator (20-mm long terbium gallium garnet (TGG) crystal, using Sellmeier equation from [116]) and the grating dispersion calculated according to the standard formula

$$\mathrm{GDD}_\mathrm{grating}(\lambda) = -\frac{\lambda^3 d}{\pi c^2 \Lambda_\mathrm{g}^2} \left(1 - \left(\frac{\lambda}{\Lambda_\mathrm{g}} - \sin(\alpha)\right)^2\right)^{-\frac{3}{2}}, \tag{3.7}$$

where d denotes the grating separation, α is the angle of incidence and $\Lambda_\mathrm{g} = 1\,\mu\mathrm{m}$ is the grating period.

Figure 3.2(c) and (d) show two different measurement series: (c) corresponds to the curves obtained using the data shown in (a) and (b). When changing the grating separation in the series shown in (a) and (b), the wave plate positions were changed as well to find the most stable mode-locking states. Furthermore, the measurement series performed at a grating separation of 8.1 mm also includes a state that was found after increasing the pump power and adapting the wave plate positions (orange curve), while keeping the same grating separation. For the data set shown in Fig. 3.2(d) however, only the grating separation was changed and the measurement was repeated at different pump powers (no changes in wave plate position). These data show that the pump power level does not noticeably change the intracavity GDD. Changing the total losses (and thus the inversion level) by adjusting the wave plate positions on the other hand does have an impact.

3.4 Mode-locking characterization

In the following, we will discuss five characteristic mode-locking states obtained at different values of intracavity dispersion (see states marked in Fig. 3.2(c)). The optical spectra are depicted in Fig. 3.3(a), while the microwave spectra of the fundamental repetition rate frequency and its higher harmonics are shown in Fig. 3.3(b) and (c), respectively.

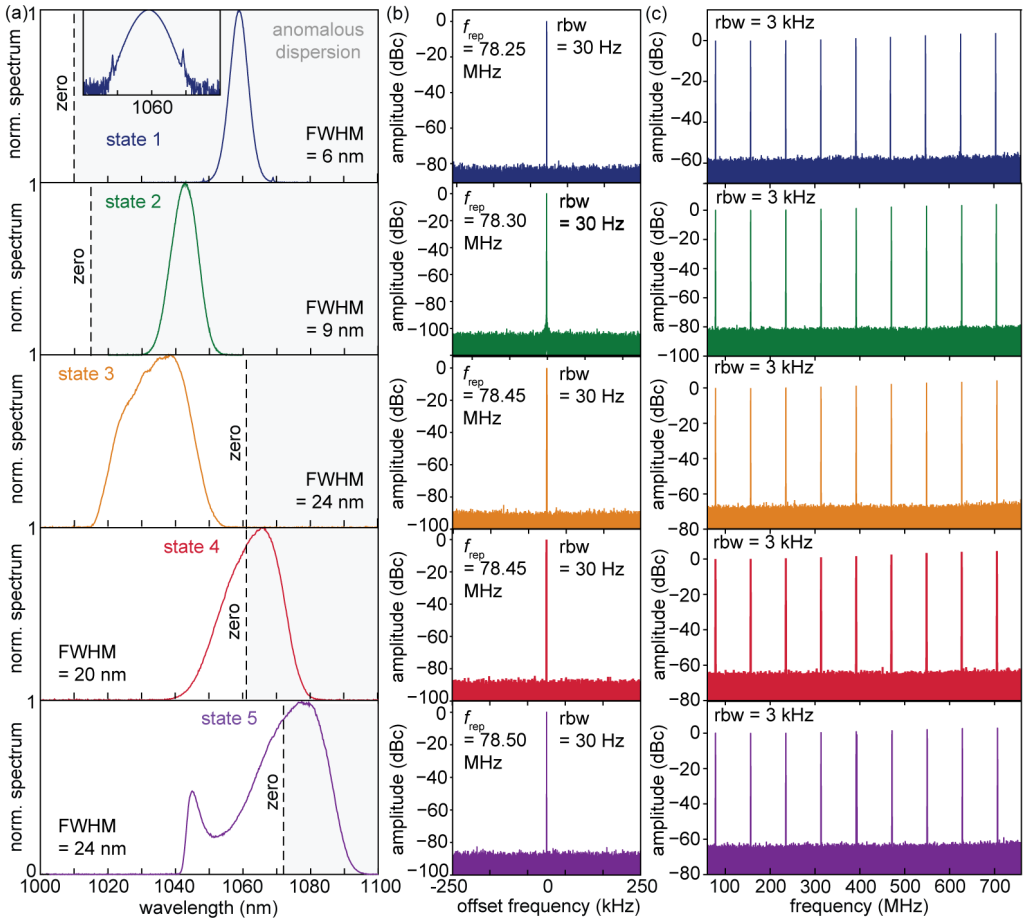

Figure 3.3 – (a) Mode-locking characterization of the 5 states indicated in Fig. 3.2(c). (a) Optical spectra recorded with an optical spectrum analyzer (Ando AQ6315A) using a resolution bandwidth of 0.5 nm. The gray shaded area indicates anomalous intracavity GDD, while the dashed line represents the wavelength at which the intracavity GDD is zero. (b) 500-kHz zoom into the repetition rate frequency f_{rep} recorded with a microwave spectrum analyzer at a resolution bandwidth of 30 Hz. (c) Wide span showing the higher harmonics of f_{rep}.

Table 3.3 – Typical pump power and output power levels for the mode-locking states 1-5.

State	1	2	3	4	5
Pump current	125 mA	130 mA	650 mA	205 mA	190 mA
Pump power	31 mW	34 mW	328 mW	77 mW	68 mW
Power at output port	4 mW	5 mW	120 mW	10 mW	10 mW
Power at rejection port	2 mW	1 mW	40 mW	7 mW	10 mW

Note that these mode-locking states were obtained without the slit used during the dispersion measurements. The pump power and waveplate positions for each state were optimized in order to obtain clean fundamental mode-locking (i.e. no multi-pulsing or cw-breakthroughs). Once an initial set of optimal parameters was found, the states could be easily reproduced at will. Table 3.3 summarizes typical pump power and output power levels for each state (note that the output power in each state is adjustable over a certain range while keeping clean mode-locking by fine-tuning the output coupling wave plate and the pump power level).

All states can be attributed to variations of the stretched-pulse mode-locking regime. In state 1 and 2 (i.e. net negative/anomalous cavity dispersion), solitonic effects limit the intracavity pulse energy, leading to the occurrence of double pulses at higher pump powers. This constraint is lifted for state 3, which is running in the normal dispersion regime around 1030 nm and is capable of delivering much higher output powers (>100 mW). State 4 can be found using the same grating separation as for state 3, however with slightly different wave plate positions, which results in operation around 1060 nm, hence close to zero-dispersion. By slightly reducing the grating separation, the zero-dispersion wavelength can be shifted even further away to ≈1075 nm, which is where state 5 operates.

3.5 Amplitude and phase noise measurements

3.5.1 Amplitude noise/RIN measurements

Figure 3.4(a) shows the amplitude noise/RIN of the five different laser states. Since the output of the pump diode is fiber-coupled and directly spliced to the NALM ring via the WDM for maximum mechanical robustness, the pump power can only be regulated by changing the pump diode's driving current. For the

pump diode used here (Thorlabs BLG976-PAG900), we noticed that the RIN is not constant over its operation range (see Appendix for details). We thus included the RIN of the pump measured at the pump current setting corresponding to the different mode-locking states in Fig. 3.4(a). In Fig. 3.4(b) we show the RIN of each state normalized by its corresponding pump RIN.

In order to obtain a meaningful data set over a large range of noise frequencies (1 Hz to 1 MHz), we used different measurement methods and combined them to circumvent limitations related to their respective measurement sensitivities. The methods were validated by cross-checking that the data indeed overlaps in regions where different methods were supposed to yield the same results. To minimize the amount of non-laser related noise sources, we omitted the use of external voltage amplifiers and instead used the direct photodiode outputs. The data traces shown in Fig. 3.4(a) were obtained as follows:

- For the **RIN characterization of the pump** light (976 nm) we used an InGaAs photodiode (Thorlabs PDA20CS, InGaAs, 5 MHz bandwidth, gain set to 0 dB) whose output was low-pass filtered at 1.9 MHz and recorded with an oscilloscope (LeCroy WavePro 760Zi). 100 time traces of 1 s duration (yielding a rbw of 1 Hz) and 100 traces of 10 ms duration (rbw=100 Hz) were recorded and directly averaged in the Fourier-domain using the instrument's internal FFT (rectangular window) and averaging function. The final RIN traces were obtained by subtracting the measurement background noise (traces recorded without laser light on the photodiode), normalizing by the corresponding rbw and DC-voltage level and stitching the traces together appropriately.

- The traces for **state 1 and state 2** were obtained by measuring the amplitude noise at the repetition rate frequency (photodiode: Thorlabs DET08 InGaAs bias detector, 5 GHz bandwidth, no amplifier) using a signal source analyzer (SSA, Keysight E5052B). The latter was set to its AM-measurement mode (number of averages: 16), which uses an internal phase-locked loop (PLL) to demodulate the carrier frequency and separate phase noise from amplitude noise.

- For the **states 3, 4 and 5** (which have less noise at low offset frequencies) the SSA's AM-measurement mode did not provide sufficient sensitivity in the range of 1-100 Hz. To cover this range, we instead used the SSA's baseband (BB) noise measurement in combination with the PDA20CS, which has less bandwidth, but a higher voltage output per optical input. At offset frequencies >10 kHz however, the noise level of the internal transimpedance

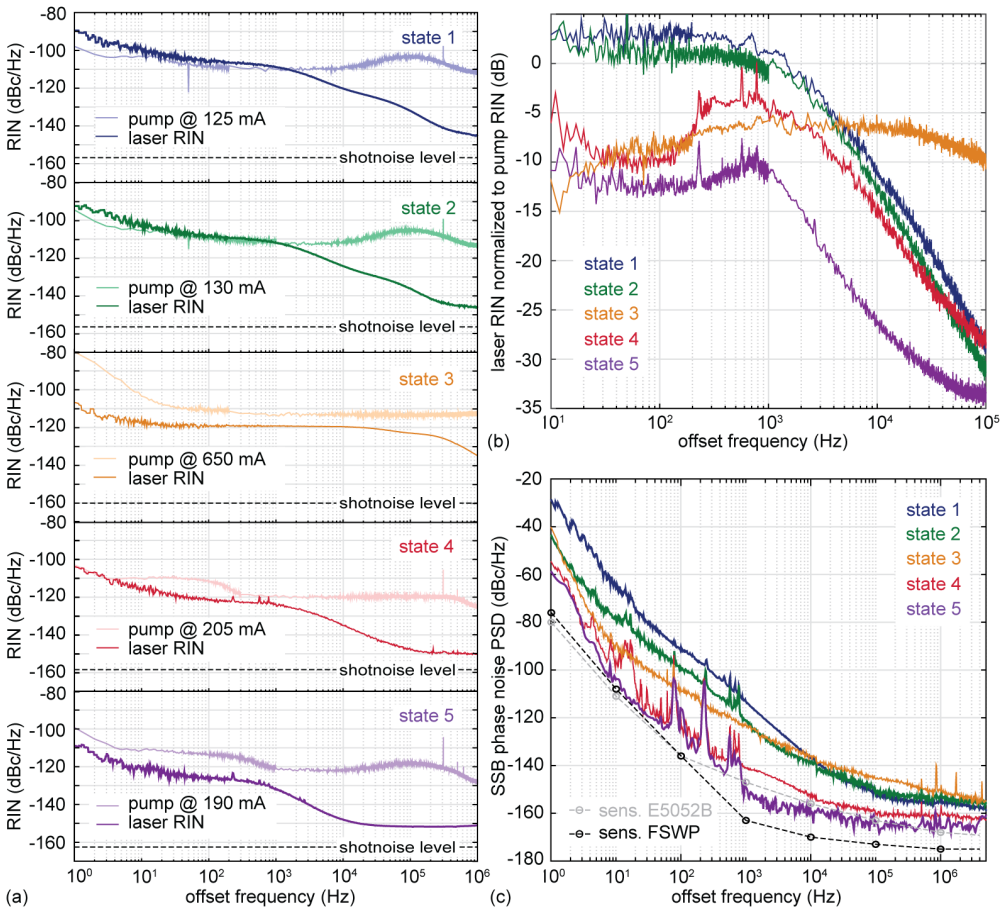

Figure 3.4 – (a) RIN of state 1-5 including the corresponding pump noise. Note that if the trace has been obtained by combining two different measurement methods (see text), the photodetector shot noise level marked here refers to the higher of the two. (b) Laser RIN curves shown in (a) normalized to their respective pump RIN curves. (c) Single-sideband (SSB) phase noise measurement of the repetition rate frequency performed using a signal source analyzer (state 1 4: Keysight E5052B, state 5: Rohde & Schwarz FSWP).

amplifier of the PDA20CS becomes comparable to the RIN of the laser, hence the measurements obtained with the SSA's AM-mode and the DET08 were used to complete the traces at offset frequencies >10 kHz.

The power spectral densities (PSDs) shown in Fig. 3.4(a) of both the pump and laser output noise have been integrated over two different offset frequency ranges, yielding the root-mean-square (rms) RIN values listed in Table 3.4.

Table 3.4 – Integrated rms RIN values for different integration intervals.

State	**1**	**2**	**3**	**4**	**5**
(1 Hz, 1 MHz)					
Laser:	0.028 %	0.019 %	0.048%	0.006%	**0.003 %**
Pump:	0.418 %	0.333 %	0.230 %	0.089 %	0.081 %
(10 Hz, 100 kHz)					
Laser:	0.027 %	0.018 %	0.028 %	0.005 %	**0.002 %**
Pump:	0.180 %	0.141 %	0.070 %	0.033 %	0.035 %

3.5.2 Discussion of the RIN behavior

Interesting differences can be observed between the 5 mode-locking states when looking at the normalized data in Fig. 3.4(b). In the states operating in the anomalous dispersion regime (state 1 and 2), the laser noise mainly follows the pump RIN level up to ≈1 kHz, before rolling off by ≈15 dB/decade. For state 4 and 5, we observe a similar roll-off, but in addition also a suppression of the pump noise at frequencies <1 kHz by 5 to 10 dB. State 3 operating in the normal dispersion regime also shows similar pump noise suppression at low offset frequencies, but with a roll-off that starts at much higher offset frequencies (>10 kHz) and has a flatter slope. The fact that the RIN rolls off at lower frequencies for mode-locking states in the negative dispersion regime and close to zero GDD than for states operating with positive intracavity dispersion has already been observed in the case of Yb:fiber lasers based on NPE-mode-locking [117, 118]. The noise properties of each state are governed by a complex balance of various effects that need to be taken into account when interpreting these measurements, as will be discussed in the rest of this paragraph.

The response properties of the gain medium alone can be separated from the oscillator dynamics by looking at the noise transfer function in amplifiers made of the same gain medium [119–121]. These references show how the effective roll-off (or corner) frequency of the pump-to-laser noise transfer function not only depends

on the fluorescence lifetime of the gain medium (which in the case of Yb would correspond to $f_{\mathrm{roll-off}} \approx 227$ Hz), but also on the absolute pump level. Putting the gain fiber into a resonator generally leads to relaxation oscillations, which in addition to the upper-state lifetime also depend on the resonator losses and length and are often clearly visible as strong peaks in the RIN of cw-lasers. Mode-locking operation however tends to suppress these strong relaxation frequency peaks [**Namiki1996**]. Both saturable and inverse saturable absorption have been shown to significantly influence the suppression behavior [122, 123]. In a NALM-mode-locked laser, inverse saturable absorption is an inherent effect and simply corresponds to the roll-over of the periodic cavity transmission curve. Low linear losses, i.e. a high cavity finesse is also generally known to support low-noise performance [124].

Depending on the pulse dynamics however, additional effects may come into play. Solitons exchange energy with the co-propagating dispersive wave, leading to Kelly sidebands (in our case, state 1 shows the onset of small Kelly sidebands when looking at the spectrum on a logarithmic scale, see inset in Fig. 3.3(a)). This exchange stabilizes the pulse energy, but also leads to RIN that is spectrally dependent; it was shown that most of the RIN is actually concentrated in the Kelly sidebands [125]. When the laser is mode-locked entirely in the positive/normal dispersion regime, other self-stabilization mechanisms are dominating. Wavelength filtering has shown to substantially reduce the RIN in these cases and is even necessary to achieve mode-locked operation for larger intra-cavity dispersion values [126]. Although our laser does not contain a fixed band-pass filter, the NALM effect itself is wavelength dependent. Hence, the rejection port can act as a wavelength filter, since the spectral wings of strongly chirped pulses will experience a different nonlinear phase shift in the loop than the pulse center. Another wavelength-dependent noise factor is amplified spontaneous emission (ASE), which is generally stronger around the maximum of the gain profile (i.e. ≈1030 in Yb:fibers).

A favorable combination of the effects stated above led to particularly low-noise operation in the case of state 5 (operating around 1075 nm close to zero dispersion). The integrated RIN values of 0.002 % in [10 Hz, 100 kHz] (0.003 % in [1 Hz, 1 MHz]) are among the best values achieved by free-running state-of-the-art lasers [43, 104, 127].

3.5.3 Phase noise/timing jitter measurements

In addition to the RIN measurements, we also determined the single-side band (SSB) phase noise of the repetition rate frequency for each of the 5 states us-

ing a fast photodetector (Thorlabs DET08 InGaAs) and a signal source analyzer (Keysight E5052B for state 1-4 and Rhode & Schwarz FSWP for state 5). The measurement traces are shown in Fig. 3.4(c) and the corresponding integrated timing jitter values are stated in Table 3.5 for different integrations bandwidths.

3.5.4 Discussion of the phase noise behavior

Within the framework of this study, the phase noise/timing jitter measurements were performed with a signal source analyzer as a quick method to compare the different fully free-running mode-locking states. The phase noise values at high offset frequencies and hence the timing jitter values obtained here are however limited by the photodiode + signal source analyzer method and cannot really be compared with the values achieved with state-of-the-art measurements performed using balanced optical cross-correlation (BOC) [56, 128, 129], optical heterodyning [130] or fiber-delay methods [131, 132]. Nevertheless, our measurements already allow us to compare the 5 different states and observe correlations between the phase and amplitude noise. Free-running phase noise at low offset frequencies (<1kHz) is often said to purely originate from mechanical vibrations and drift of the laser cavity. In our setup however, all 5 states were obtained from the same laser, i.e. without changing any of its mechanical components nor its environment (the laser was placed on an optical table inside a box covered with a lid to minimize air turbulences). The differences can be explained by the different RIN, which couples to timing jitter via self-steepening and the Kramers-Kronig phase change in the gain medium [133]. A more fundamental limitation comes from ASE, which couples to the timing jitter either directly or via the Gordon-Haus effect [134]. The latter denotes jitter that is caused by fluctuations of the center frequency, which then translates to fluctuations of the group velocity as a consequence of dispersion. It was predicted already in the 1990s that minimizing dispersion in stretched-pulse lasers would lead to a reduction in phase noise/timing jitter [135], which has been experimentally validated by other groups [118, 128] and is also consistent with what we observe here.

3.6 Carrier-envelope offset (CEO) detection

3.6.1 Self-referencing setup

To complete the characterization of our five mode-locking states, we have detected the CEO frequency using standard f-to-$2f$ interferometry. In order to reach sufficient peak power for octave-spanning spectral broadening in a PCF, we amplified

Table 3.5 – Integrated timing jitter values for different integration intervals (repetition rate f_{rep} = 78 MHz).

State	1	2	3	4	5
(1 Hz, 1 MHz)	71246 fs	10119 fs	11982 fs	3174 fs	2166 fs
(10 Hz, 1 MHz)	4014 fs	1208 fs	354 fs	255 fs	100 fs
(100 Hz, 1 MHz)	803 fs	351 fs	202 fs	81 fs	72 fs
(1 kHz, 1 MHz)	175 fs	103 fs	151 fs	31 fs	20 fs
(10 kHz, 1 MHz)	67 fs	76 fs	130 fs	28 fs	19 fs

the output pulses of the states 1,2,4 and 5 using a 70 cm long PM Yb-doped amplifier pumped/driven by the same type of diode/current controller as the laser. The maximum power available at the output port of the laser (see Table 3.3) was used in each of these cases as an input to the amplifier. State 3 already provided sufficient output power, hence the amplifier fiber was replaced by a passive PM single-mode fiber in that case in order to keep the rest of the setup as similar as possible. After the amplifier/single-mode fiber, the pulses were compressed using a grating pair (same gratings as used inside the laser, see Table 3.1) and ≈50-60 mW of average power were coupled into a 1-m long commercial highly nonlinear PCF (NKT NL-3.2-945) to generate a coherent octave-spanning supercontinuum. In the case of time-bandwidth-limited sech^2-pulses, the NKTNL-3.2-945 requires 5-6 kW of peak power in order to achieve an octave spanning supercontinuum after 1 m of fiber [62]. For each of the states shown here, we optimized the peak power "on-the-fly" by fine-tuning the grating compressor after the amplifier while observing the spectral broadening after the PCF on an optical spectrum analyzer. In the f-to-$2f$ interferometer, light around 1360 nm was frequency-doubled in a 1-mm long periodically poled lithium niobate (PPLN) crystal, before being temporally and spatially overlapped on a photodetector with the $2f$-component originating from the supercontinuum. The CEO beat notes were recorded using a microwave spectrum analyzer (Keysight PXA N9030B) and are shown in Fig. 3.5. Note that the amplifier/SCG/f-to-$2f$ setup was designed for versatility, i.e. to be compatible with all the mode-locking states, and is hence not optimized to provide the best signal-to-noise (SNR) ratio for each state. Nevertheless, the SNR obtained is sufficient for our current main goal: the comparison of the free-running CEO linewidths.

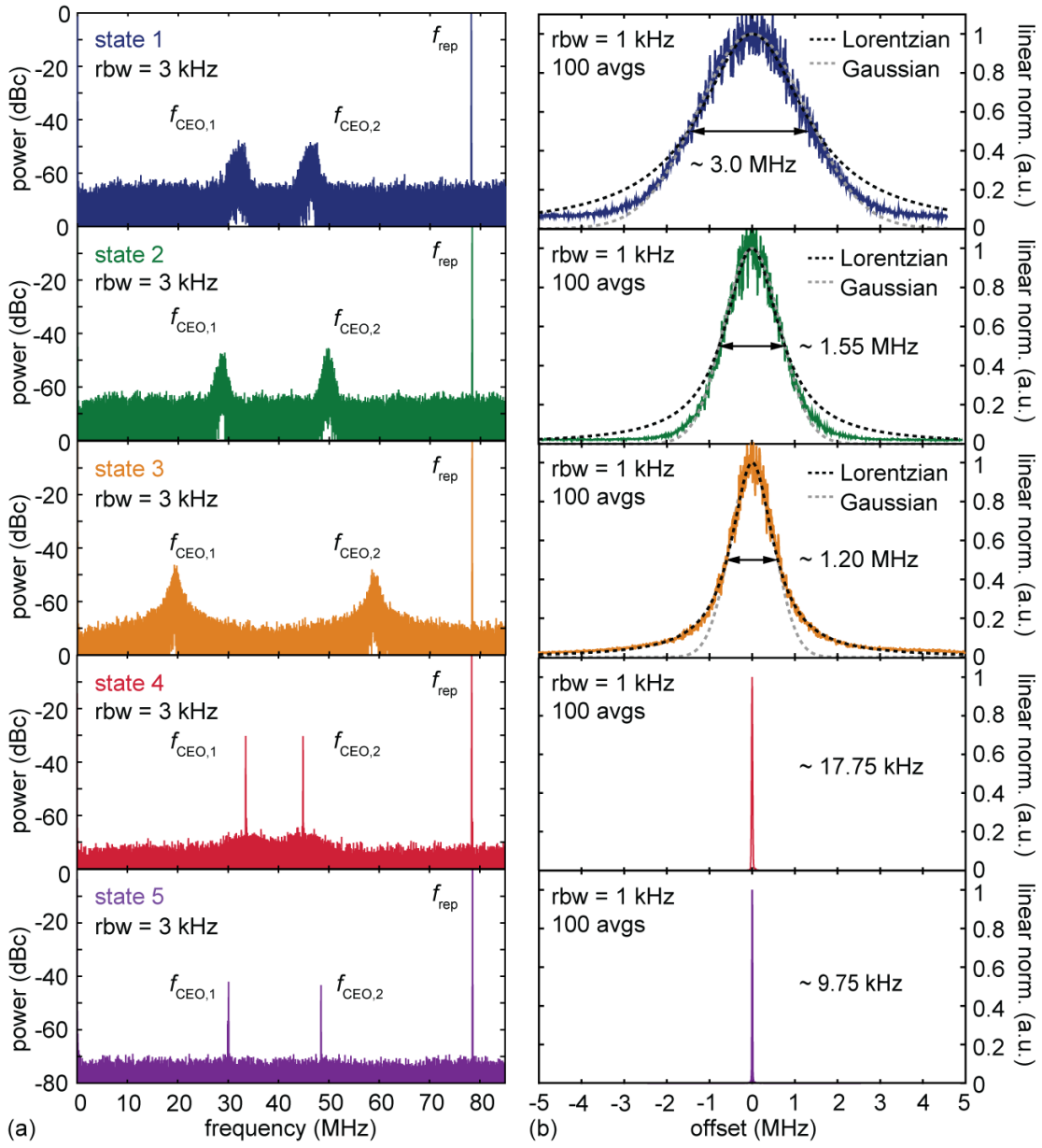

Figure 3.5 – (a) Carrier-envelope offset (CEO) frequency f_{CEO} recorded with a Keysight PXA N9030B microwave spectrum analyzer at a resolution bandwidth (rbw) of 3 kHz. (b) Zoom into f_{CEO} using an rbw of 1 kHz and averaging over 100 sweeps

3.6.2 Free-running frequency noise and linewidth analysis

For signals with small phase excursions, the linewidth is sometimes estimated by calculating the integrated phase noise as a function of the lower integration limit: the offset frequency at which the integrated phase noise reaches 1 rad^2 scorresponds to the half-width at half maximum (HWHM) of the signal [136, 137]. Signals exhibiting only small phase excursions can be expressed as a carrier signal with modulation sidebands, and an integrated phase noise of 1 rad^2 then corresponds to having ≈37 % of the total signal power in the carrier.

However, the free-running CEO signal is subjected to flicker noise (i.e. large drifts at close-in offset frequencies) and hence the small-phase-deviation assumption is not fulfilled. As a consequence, the linewidth has to be stated as a function of measurement time to allow for meaningful comparisons.

Using a sweeping microwave spectrum analyzer with fixed sweep time settings allows us to get a first quick comparison between the five different mode-locking states. In Fig. 3.5(b), we show the CEO signal of the five states on a linear scale at 1 kHz rbw in a 10 MHz span. The data was read out after averaging over 100 sweeps, which corresponds to a measurement time of ≈8 s. The FWHM linewidths vary by more than two orders of magnitude, ranging from 3 MHz (state 1) down to 9.75 kHz (state 5).

A more quantitatively precise method to determine the linewidth as a function of observation time consists of retrieving the lineshape via the frequency noise PSD $S_f^{\mathrm{CEO}}(f)$, whose lowest offset frequency corresponds to the inverse of the measurement time. The lineshape $P_{\mathrm{CEO}}(f)$ can be obtained by calculating the Fourier transform of the field autocorrelation function $\Gamma_{\mathrm{E}}(\tau)$, which can be expressed in terms of $S_f^{\mathrm{CEO}}(f)$ as described in [138]:

$$P_{\mathrm{CEO}}(f) = \mathcal{F}\left(\Gamma_{\mathrm{E}}(\tau)\right) = 2\int_{-\infty}^{\infty} e^{-i2\pi f\tau}\Gamma_{\mathrm{E}}(\tau)\mathrm{d}\tau = 2\int_{-\infty}^{\infty} e^{-i2\pi f\tau} e^{-2\int_0^{\infty} S_{f'}^{\mathrm{CEO}}(f')\frac{\sin^2(\pi f'\tau)}{f'^2}\mathrm{d}f'}\mathrm{d}\tau \tag{3.8}$$

For a frequency noise PSD that has a constant level, i.e. $S_f^{\mathrm{CEO}}(f) = h_0$ (Hz^2/Hz), eq. 3.8 can be analytically solved and yields a Lorentzian profile. A Gaussian profile on the other hand is obtained when modelling the frequency noise as constant below a certain cut-off frequency f_{c} and zero for offset frequencies $f > f_{\mathrm{c}}$ [138].

In Fig. 3.5(b), we added both a Gaussian and a Lorentzian line profile with the same full-width-at-half-maximum (FWHM) to the f_{CEO} measurements of state 1-3. For state 1 and 2, the Gaussian profile is a better fit, while for state 3, the Lorentzian fit is clearly more appropriate. The fact that the line profile of state 3 is closer to a Lorentzian can be traced back to the RIN: the predicted

CEO frequency noise PSD $S_f^{\mathrm{CEO,\,pump}}(f)$ caused by pump noise can be expressed according to [139] as

$$S_f^{\mathrm{CEO,\,pump}}(f) = \left(P_{\mathrm{pump}} \frac{\mathrm{d}f_{\mathrm{CEO}}}{\mathrm{d}P_{\mathrm{pump}}} \right)^2 \mathrm{RIN}_{\mathrm{laser}}(f) = \xi^2 \mathrm{RIN}_{\mathrm{laser}}(f) \tag{3.9}$$

where P_{pump} denotes the pump power and ξ^2 is the coupling factor. Since the laser RIN in state 3 exhibits a much higher roll-off frequency (Fig. 3.4(b)), the approximation of white frequency noise for $S_f^{\mathrm{CEO}}(f)$ is thus more appropriate than for state 1 and 2.

In the following, we will take a closer look at the CEO linewidths of state 4 and 5, which are significantly narrower than those of states 1-3. Since both state 4 and 5 operate in a similar pump power range, we set the pump diode current to the exact same value (220 mA) for all the measurements shown in Fig. 3.6 in order to allow for a straight-forward comparison of the two states. In Fig. 3.6(a) and (b), we show a 100-kHz zoom recorded with a 300-Hz resolution bandwidth, corresponding to a total measurement time of ≈9 s.

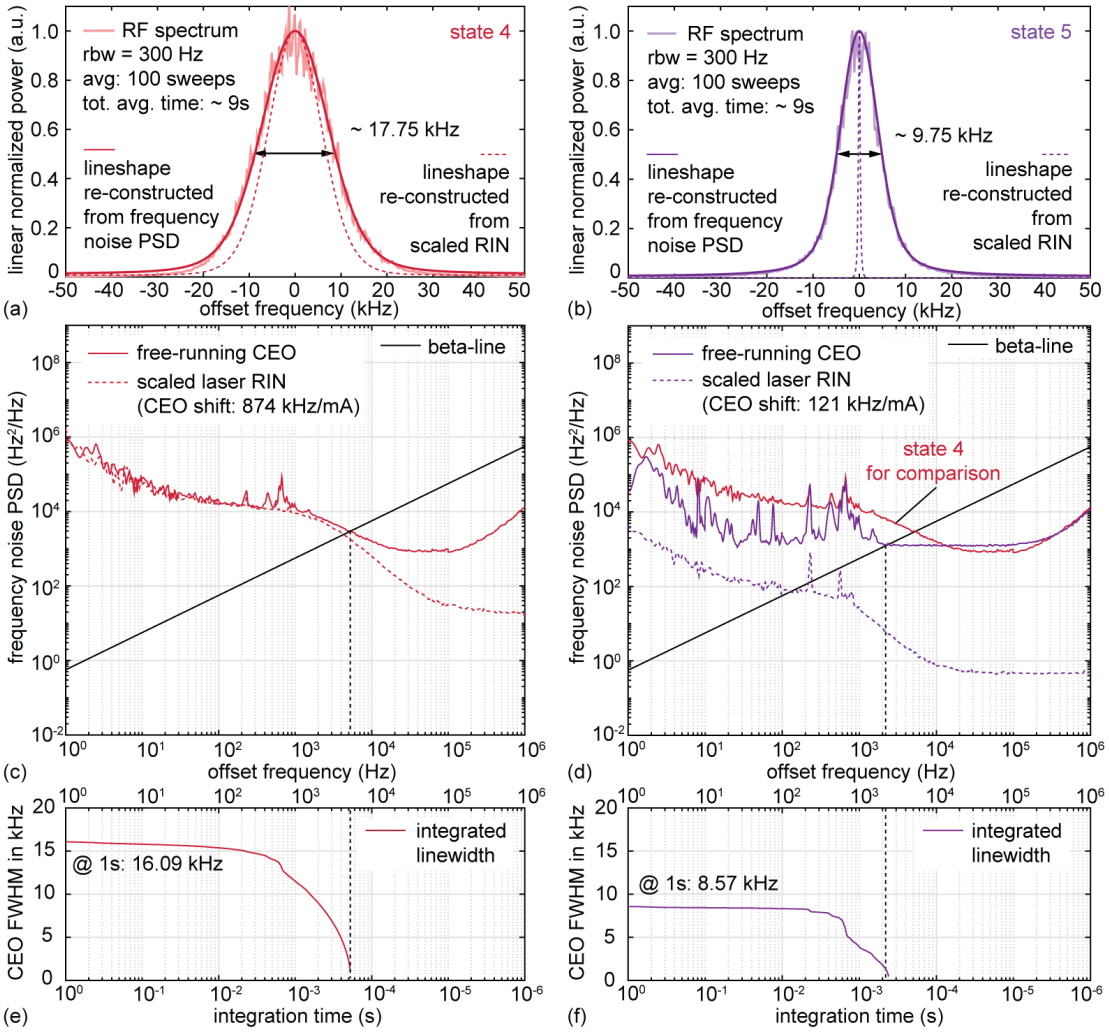

Figure 3.6 – (a),(b) Zoom into f_{CEO} of state 4 and 5 recorded with a Keysight PXA N9030B microwave spectrum analyzer at a resolution bandwidth (rbw) of 300 Hz and averaged over 100 sweeps (total averaging time ≈9 s). The solid lines are the lineshapes re-constructed from the frequency noise power spectral densities (PSDs) shown in (c) and (d). (c),(d) Frequency noise PSD $S_f^{\mathrm{CEO}}(f)$ measured for state 4 and 5 using the Rohde&Schwarz FSWP signal source analyzer. The "CEO shift" value indicates the shift of f_{CEO} for 1 mA change in pump driver current. The dashed curves are the PSDs $S_f^{\mathrm{CEO,\,pump}}(f)$ corresponding to the contribution of the pump-induced laser RIN to the total frequency noise PSD $S_f^{\mathrm{CEO}}(f)$. (e),(f) FWHM of f_{CEO} calculated as a function of integration time using the beta-separation line approach (see text for details).

In Figs. 3.6(c) and (d), we show the frequency noise PSD $S_f^{\mathrm{CEO}}(f)$ of the free-running CEO of state 4 and 5 measured with a Rohde&Schwarz FSWP signal source analyzer. Given this data, we numerically re-constructed the lineshapes according to eq. 3.8 using a lower integration limit of 1 Hz (corresponding to 1 s measurement time) and an upper limit of 1 MHz. As can be seen in Figs. 3.6(a) and (b), these calculated lineshapes overlap very well with the power spectra obtained by averaging 100 microwave spectrum analyzer sweeps and yield a FWHM of 17.75 kHz (state 4) and 9.75 kHz (state 5).

For comparison, we also calculated the FWHM linewidth as a function of integration time using the simple beta-separation line approximation described in [138, 140], which does not require the numerical implementation of eq. 3.8. This approach relies on integrating the area A under $S_f^{\mathrm{CEO}}(f)$ for $1/T_0 \leq f \leq f_{\mathrm{inter}}$, where T_0 is the integration time and f_{inter} is the offset frequency at which $S_f^{\mathrm{CEO}}(f)$ intersects the beta-line, which is defined as $S_f^{\mathrm{beta}}(f) = 8\ln(2)f/\pi^2$ (black line Fig. 3.6(c) and (d)). The FWHM of the CEO linewidth can then be calculated as

$$\mathrm{FWHM} = (8\ln(2)A)^{\frac{1}{2}} \tag{3.10}$$

For our data, this approach leads to a FWHM of 16.09 kHz (state 4) and 8.75 kHz (state 5) at 1s integration time (Fig. 3.6(e) and (f)).

As mentioned above, the pump current/power was the same for the CEO measurements of state 4 and 5. Hence the factor ≈2 in linewidth between state 4 and 5 cannot be explained by variations in pump noise, but is a direct consequence of the laser dynamics.

In order to determine the coupling between the laser RIN and the CEO frequency noise PSD as stated in eq. 3.9, we recorded the shift of f_{CEO} when modulating the pump current around its set value of 220 mA (corresponding to P_{pump}= 85.1 mW). For state 4, the shift amounts to 874 kHz/mA (coupling factor $\xi^2 = 172.68 \cdot 10^{14}$ Hz^2) while for state 5, f_{CEO} only shifts by 121 kHz/mA ($\xi^2 = 3.32 \cdot 10^{14}$Hz^2). We then measured the RIN of the laser output for both states and multiplied the curves by their respective coupling factor ξ^2, leading to the dashed curves in Fig. 3.6(c) and (d).

For state 4, the scaled RIN curve $S_f^{\mathrm{CEO,\,pump}}(f)$ lies only marginally below the measured PSD $S_f^{\mathrm{CEO}}(f)$ at low offset frequencies (at high offset frequencies, the measurement of $S_f^{\mathrm{CEO}}(f)$ is limited by the SNR of f_{CEO}). This observation suggests that the CEO frequency noise for state 4 is mainly dominated by the laser RIN, which in turn is dominated by pump noise.

For state 5 however, the frequency noise contribution originating from the laser RIN lies significantly below the measured PSD $S_f^{\mathrm{CEO}}(f)$. The laser thus operates

in a regime where - in contrast to states 1-4 - pump-induced RIN is not the main direct contributor to the f_{CEO} linewidth anymore. The re-constructed theoretical RIN-limited linewidth (dashed line in Fig. 3.6(b)) amounts to only 434 Hz. Hence, we suspect the 9.75-kHz-linewidth to be mainly determined by other potential noise sources having an impact on f_{CEO}, such as for instance vibrations of the gratings or the end mirror, which could be controlled in a future implementation by using appropriate piezo-actuators.

According to the beta-separation line approach [138], the minimum servo-loop bandwidth required to obtain a tight lock of f_{CEO} (i.e. where the frequency noise PSD does not exceed the beta-line anymore) corresponds to f_{inter}, which amounts to only $\approx$ 2.4 kHz for state 5 (dashed black line in Fig.3.2). To the best of our knowledge, the FWHM of 9.75 kHz at 1 s integration time corresponds to the narrowest free-running f_{CEO} linewidth reported to date for NALM-based fiber-lasers.

3.7 Conclusion

In summary, we have presented a versatile PM-NALM-based fiber laser design that offers access to a large parameter space of mode-locking states. The design was implemented in a 78-MHz Yb:fiber configuration using an intracavity grating pair for flexible dispersion control. We discussed the role of the different wave plates in tuning the modulation depth, output coupling ratio and phase bias, thus providing guidelines on how to achieve reliable self-starting mode-locking in this type of lasers. We furthermore presented five representative mode-locking states obtained at different values of intra-cavity dispersion. We characterized the RIN, phase noise and CEO noise in free-running operation to analyze the influence of the mode-locking regime on the overall noise performance of the different states.

We have shown that the coupling of pump noise to laser RIN and thus also to timing jitter and CEO noise can be substantially suppressed for the states operating around zero net intracavity dispersion. In the most extreme case, in addition to being close to zero-dispersion, by operating the laser around 1075 nm center wavelength (i.e. far from the spontaneous emission peak of Yb around 1030 nm), we obtained very low integrated laser RIN of 0.003 % [1Hz, 1 MHz] and a CEO linewidth below 10 kHz. By analyzing the residual contribution of the RIN to the free-running CEO linewidth, we showed that - unlike for most mode-locked lasers - the CEO linewidth in this case is actually not pump-RIN limited anymore.

Various approaches can be employed to actively suppress the RIN in a fiber laser and thus improve the general comb noise performance. However, passive

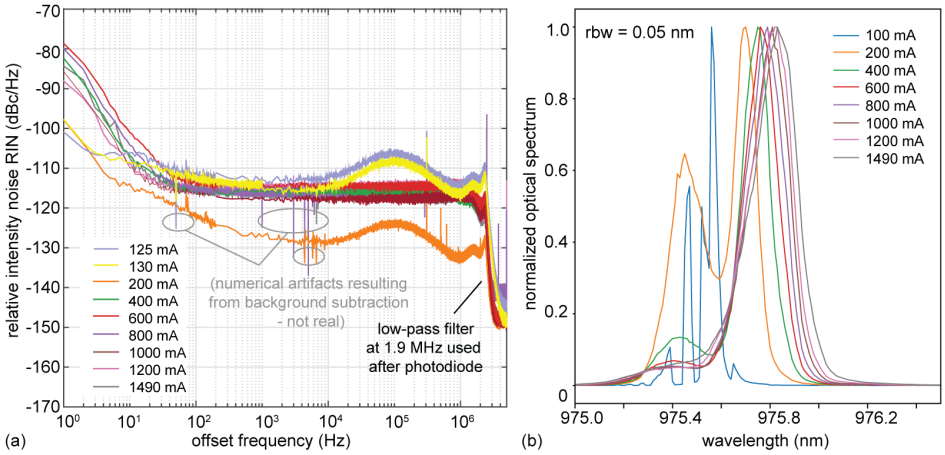

Figure 3.7 – RIN of the pump diode (Thorlabs BLG976-PAG900) at 25°C for different current values using a CLD1015 controller with its modulation input turned off. (b) Optical spectra of the pump diode output for different driver current values measured with an Ando AQ6315A.

optimization by finding low-noise mode-locking regimes will significantly reduce the requirements on the feedback loop bandwidths necessary for full comb stabilization and hence decrease the system complexity.

Due to its flexibility, robust PM-implementation and compatibility with standard Yb-based amplification schemes, we consider this Yb:fiber laser type to be a promising seed source in particular for low-noise high-power frequency comb applications.

Appendix A: Pump diode characterization

Upon closer investigation of the pump diode behavior, we observed a correlation between the optical output spectrum and the RIN-level: although the lasing threshold is situated at ≈100 mA, the FBG does not fully lock the optical spectrum until the current reaches >400 mA. For pump currents >400 mA the RIN exhibits a fairly constant white noise level for offset frequencies >100 Hz, but rather high low-frequency fluctuations. For pump currents <400 mA (which coincidentally happens to be the range used for most of our mode-locking states), the RIN level is lower in the 1-100 Hz-range, but exhibits a bump around 100 kHz. The overall pump RIN is highest directly above the diode's lasing threshold and seems to reach a minimum just before the proper onset of the FBG-feedback (i.e. pump currents around 200-300 mA). An in-depth analysis of the dynamics within the pump diode causing this type of behavior as well as any generalized statement regarding the applicability of these observations to other pump diodes is however

beyond the scope of this paper.

Funding
Austrian Federal Ministry for Digital and Economic Affairs; National Foundation for Research, Technology and Development; Austrian Science Fund (FWF) (M2561-N36).

Acknowledgment
The authors would like to thank Valentina Shumakova for helpful comments on the manuscript.

Disclosures
The authors declare no conflicts of interest.

3.8 Non-published supplementary material

Supercontinuum generation and f-to-2f interferometer

In this section, we provide more information on the setup for supercontinuum generation and f_{CEO}-detection, as these details were omitted in the paper.

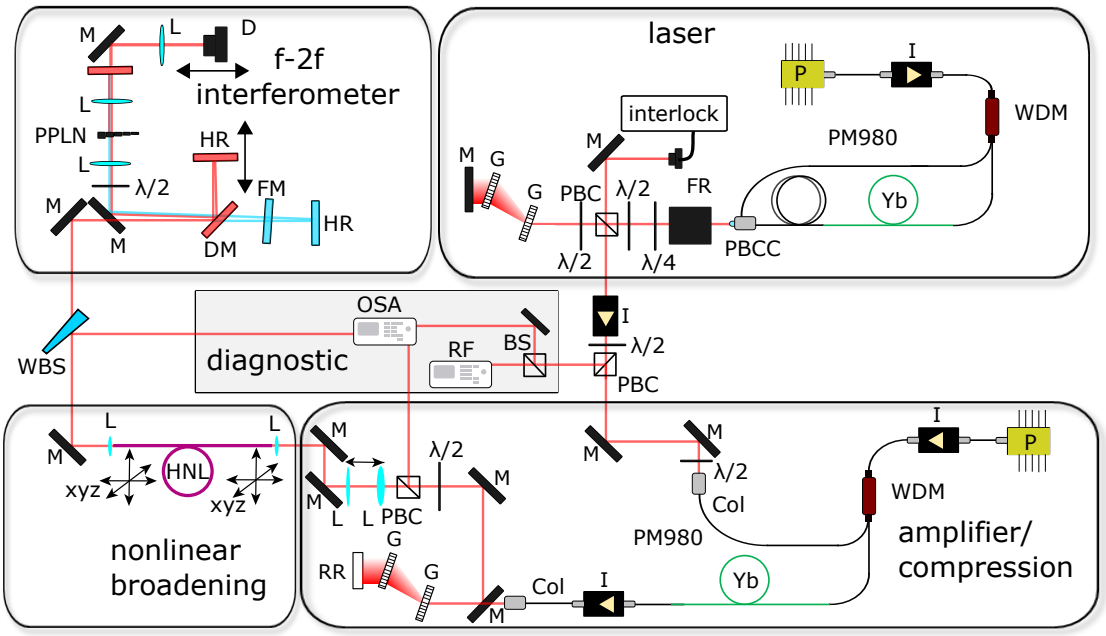

Figure 3.8 – Overview of the f-2f interferometer setup. The output of the figure-9 laser is amplified in an ytterbium-doped single-mode amplifier. After the amplification, the pulses are compressed in the temporal domain via a grating compressor. The compressed pulses are subsequently spectrally broadened in a highly nonlinear fiber. The beat note is generated in a quasi-common path interferometer. M: mirror, L:lens, $\lambda/2$: $\lambda/2$-waveplate, $\lambda/4$:$\lambda/4$-waveplate, FR: Faraday rotator, Yb: ytterbium-doped fiber, PBC: polarization beamsplitter cube, G: grating, PBCC: polarization beam combining collimator, Col: collimator, I: isolator, DM: dichroic mirror, FM: filter, HR: highly reflective mirror, D: photodiode, P: pump diode, WDM: wavelength division multiplexer, xyz: 3-axis stage, HNL: highly nonlinear fiber, OSA: optical spectrum analyzer, RF: radio frequency analyzer, BS: beam splitter, PPLN: periodically poled lithium niobate.

Figure 3.8 shows the complete setup. After the oscillator, we installed an isolator to avoid back-reflections (EOT-HP-05-I-1030). Using a $\lambda/2$-wave plate and a polarization beam splitter, we separated a fraction of the light for the laser diagnostics. However, after checking for clean modelocking operation, we usually minimized the power and this port and sent the full power to the amplifier. The free-space light was coupled into the amplifier using a fixed lens collimator (Thorlabs-F110APC-1064). We added a $\lambda/2$-wave plate in front of the collimator

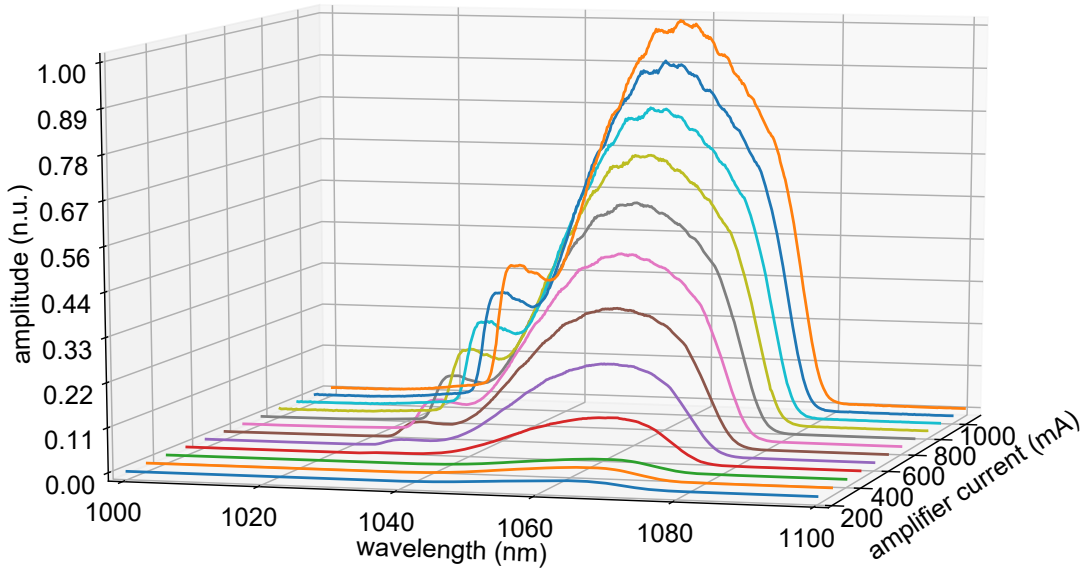

Figure 3.9 – Amplifier slope for state 4 in the paper. With an available pump power of 700 mW corresponding to 1400 mA pump current, we could reach a maximum output power of 350 mW.

to fine-tune the polarization. Controlling the polarization is important, since our amplifier is made of polarization-maintaining fiber: the two axes of the fiber feature slightly different refractive indices, hence, if the polarization of the coupled light is not strictly parallel to one of the two axes, a phase delay between the two axes occurs, which will lead to two slightly delayed pulses. The two slightly delayed pulses will lead to modulations in the optical spectrum. We ensured coupling to the slow axis of the fiber by optimizing the output power of the unpumped amplifier since the isolator at the end of the amplifier blocks the fast axis.

The pump and signal light were coupled into a 70-cm long PM Yb-doped gain fiber (CorActive Yb 401-PM) using a wavelength division multiplexer (AFR PMFWDM-9806-N-B-Q). Signal and pump were co-propagating inside the gain fiber. The signal was amplified to around ≈100 mW. An exemplary amplifier slope for state 4 in the paper is shown in Fig. 3.9.

At the output of the amplifier, the light was collimated using a high-end triplet-lens collimator (Thoralbs TC06APC-1064) to ensure high beam quality. This high beam quality is essential when coupling into highly nonlinear fibers later on, since the latter have a tiny core. After the amplifier, we compressed the light by using an additional grating compressor. An additional $\lambda/2$ wave plate and a polarization beam splitter cube was used for power regulation and to send light to the diagnostics section. We used a telescope to optimize the beam diameter for

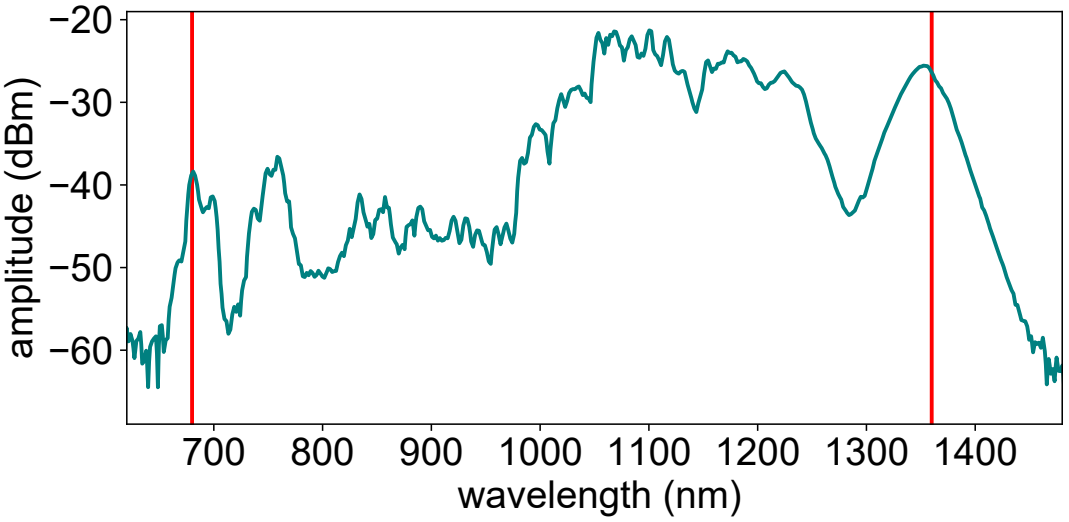

Figure 3.10 – Typical supercontinuum spectrum obtained at the output of the NKT NL-3.2-945 PCF. The red lines indicate the spectral sections used for f-to-$2f$ interferometry.

coupling into the nonlinear fiber. We used a 1-m long commercial highly nonlinear PCF (NKT NL-3.2-945) for the supercontinuum generation. Since we observed a polarization dependence of the supercontinuum generated in the nonlinear fiber, we added an additional $\lambda/2$ wave plate in front of the supercontinuum fiber. The light is coupled into the nonlinear fiber via a two silver mirrors. Additionally, we mounted the PCF and the in-coupling lens (ThorlabsC330TMD-B) on a three-axis fiber coupling stage (Thorlabs MAX313D/M). With this setup, we could reach fiber coupling efficiencies up to 85%.

The light was coupled out of the supercontinuum fiber using another three-axis stage (Thorlabs MBT602/M) and a collimation lens (Thorlabs C330TMD-C). A fraction of the output power was sent to a multimode fiber to measure the spectrum by using a wedge beam splitter (see Fig 3.10). The rest of the beam was sent to a quasi-common path interferometer. We split the light by using a dichroic mirror (Thorlabs DMLP1180) into the two arms of the interferometer. The light is reflected via highly reflective mirrors (Thorlabs: BB05-E04 for the 1280-1600 nm arm and BB05-E02 for the 400-750 nm arm.) The reflected beams are slightly shifted in height and picked up with a D-shaped mirror. Great care must be taken to both achieve spatial and temporal overlap. Temporal overlap is obtained by using a tunable delay stage in the short-wavelength arm of the interferometer. After the D-shaped mirror the light is focused into a 1-mm thick periodically poled lithium niobate crystal (PPLN) (Covesion MSHG1420-0.5-1) which is placed in-

side an oven (Covesion PV10) stabilized by a temperature controller (Covesion OC2). The poling periods of the PPLN range from 13.83 µm to 17.10 µm, which enables tuning of the wavelength for frequency-doubling from 1350 nm to 1490 nm by translating the crystal perpendicularly to the beam. An additional lens is used to collimate the beam after the PPLN. We used an optical bandpass filter (Thorlabs FB680-10) to select the wavelength region of interest and avoid saturation of the photodiode. An additional lens focuses the light on a standard biased silicon photodiode (Thorlabs DET10A2). The CEO beat notes were recorded using a microwave spectrum analyzer (Keysight PXA N9030B). The signal-to-noise ratio of the beat notes strongly depends on the coherence of the supercontinuum. We observed a strong influence of uncompensated third-order dispersion on the coherence of the supercontinuum: above a certain value of TOD, the beat notes would vanish, leaving only an elevated noise floor when tuning over the position where interference should occur using the delay stage in the short-wavelength arm. To mitigate this issue, all passive fiber of the amplifier was thus kept as short as possible.

Chapter 4

Tunable dual-comb from an all-polarization-maintaining single-cavity dual-color Yb:fiber laser

"How about a magic trick?"

The Joker, The Dark Knight

The publication presented in this chapter was authored by:

JAKOB FELLINGER[1] (laser design, experimental setup, measurements, data evaluation)

ALINE S. MAYER[1] (experimental measurements)

GEORG WINKLER[1] (data evaluation)

WILFRID GROSINGER[1] (Knox measurement)

GAR-WING TRUONG[2] (experimental measurements)

STEFAN DROSTE[3] (laser design)

CHEN LI[3] (laser design)

CHRISTOPH M. HEYL[3,4] (supervision)

INGMAR HARTL[3] (supervision)

OLIVER H. HECKL[1] (supervision)

[1] Christian Doppler Laboratory for Mid-IR Spectroscopy and Semiconductor Optics, Faculty Center for Nano Structure Research, Faculty of Physics, University of Vienna, Vienna, Austria

[2] Crystalline Mirror Solutions LLC, Santa Barbara, California 93101, USA

[3] Deutsches Elektronen-Synchrotron DESY, 22607 Hamburg, Germany

[4] Helmholtz-Institute Jena, 07743 Jena, Germany

and was published in Optics Express on 19 September 2019.
DOI: `https://doi.org/10.1364/OE.27.028062`

Preface to publication No. 3

The single-cavity dual-color laser results presented in paper 1 showed that it is possible to obtain two pulse trains with different repetition rates from the same laser cavity by using a mechanical spectral filter. Although these results were very promising, the implementation suffered from two drawbacks: the susceptibility of the NPR laser to environmental perturbations and the fact that the non-aliasing bandwidth was too low to perform meaningful spectroscopic experiments. In the following publication, we address these shortcomings by combining the concept of the the tunable mechanical spectral filter with the figure-9 laser design presented in publication 2. The versatility, but also the reliability of this mode-locking scheme enabled us to improve the self-starting behavior as well as to increase the repetition rate, which in turn allowed us to achieve a significantly larger non-aliasing bandwidth.

Publication No. 3: Tunable dual-comb from an all-polarization-maintaining single-cavity dual-color Yb:fiber laser

Abstract: We demonstrate dual-comb generation from an all-polarization- maintaining dual-color Yb fiber laser. Two pulse trains with center wavelengths at 1030 nm and 1060 nm respectively are generated within the same laser cavity with a repetition rate around 77 MHz. Dual-color operation is induced using a tunable mechanical spectral filter, which cuts the gain spectrum into two spectral regions that can be independently mode-locked. Spectral overlap of the two pulse trains is achieved outside the laser cavity by amplifying the 1030-nm pulses and broadening them in a nonlinear fiber. Spatially overlapping the two arms on a simple photodiode then generates a down-converted radio frequency comb. The difference in repetition rates between the two pulse trains and hence the line spacing of the down-converted comb can easily be tuned in this setup. This feature allows for a flexible adjustment of the tradeoff between non-aliasing bandwidth vs. measurement time in spectroscopy applications. Furthermore, we show that by fine-tuning the center-wavelengths of the two pulse trains, we are able to shift the down-converted frequency comb along the radio-frequency axis. The usability of this dual-comb setup is demonstrated by measuring the transmission of two different etalons while the laser is completely free-running.

4.1 Introduction

Dual-comb (DC) spectroscopy [14] has emerged as a versatile technique combining fast data acquisition, high-resolution and broadband spectral coverage [15]. Typically, DC systems involve two separate mode-locked lasers emitting pulse trains with slightly different pulse repetition rates. Those pulse trains correspond to two frequency combs with slightly different comb line spacings. Optical beating between the two combs leads to a down-conversion of the optical frequencies

into the radio-frequency range. Since this down-conversion takes place on a simple photodiode sensor, DC spectroscopy does not require complex spectrometer assemblies such as virtually imaged phase arrays [11] or Fourier transform spectrometers [10]. A critical aspect, however, is the mutual coherence between the two optical combs. When the combs originate from two independent lasers, active stabilization can quickly become a complex and difficult task. Different methods have already been presented to reduce the complexity of dual-comb setups, for example by phase-locking the two frequency combs to an external cavity diode laser [64] or using adaptive sampling techniques [65–68]. An additional simplification is the generation of two pulse trains using a single laser cavity: mutual coherence due to common-mode noise cancellation enables spectroscopy with a free-running laser [18]. Single-cavity dual-combs have been obtained using various mechanisms, e.g. by separating the two pulse trains using different travel directions [16, 70, 141], polarization [71, 142] or branched optical paths in a birefringent crystal [69, 143].

Here, we focus on a scheme that consists of using a single-cavity dual-color/dual-comb fiber laser, where a single laser cavity emits two pulse trains with different center wavelengths [81]. Non-zero intra-cavity dispersion leads to a difference in repetition rate for the two emitted pulse trains. Based on state-of-the-art fiber lasers, the dual-color/dual-comb approach [3, 17, 19, 72, 73, 76, 77, 79, 80, 144] shows great potential for spectroscopic measurements without the need for active stabilization of the comb parameters [17, 19, 73]. For instance, Zhao et al. described a carbon nanotube mode-locked dual-color erbium doped fiber laser [77], which then further evolved into a single-cavity dual-comb and enabled free-running spectroscopy [17]. Subsequently, Liao et al. demonstrated a thulium-doped NALM mode-locked dual-color dual-comb laser, pushing this technique towards the mid-infrared spectral region [73]. Furthermore, Li et al. focused on improving the stability of such systems to enable fieldable spectroscopy. They reported an all PM dual-wavelength mode-locked erbium fiber laser, using a Sagnac loop filter, reaching a repetition rate around 40 MHz with a difference in repetition rate (Δf_{rep}) of around 900 Hz, leading to a non-aliasing dual-comb bandwidth of 0.9 THz [25]. More recently, Chen et al. closed the spectral gap between the erbium and the thulium emission spectra using nonlinear broadening in a fiber [19].

In recent work, we have demonstrated the implementation of a mechanical spectral filter to generate a tunable dual-color laser [3]. The method was implemented in a NPR mode-locked Yb:fiber laser operating at 23 MHz. Our dual-color laser scheme offers two key features: dynamic adjustment of the spectral filter and tuning of the difference in repetition rates.

In this work, we combine these features with the benefits of an all-PM-NALM laser design. Implementing tunable spectral filtering inside a PM-laser instead of an NPE system leads to significantly higher stability and reliability. In addition, the tuning possibilities offer direct control over important dual-comb properties - the non-aliasing bandwidth and the acquisition rate. The latter is given directly by the difference in repetition rates Δf_{rep}, while the non-aliasing bandwidth $\Delta\nu$ - i.e. the maximally allowed optical overlap of the two combs before spectral aliasing occurs - must fulfill the following condition [14]:

$$\Delta\nu \leq \frac{f_{\mathrm{rep},1}^2}{2\Delta f_{\mathrm{rep}}}. \tag{4.1}$$

Furthermore, we increased the repetition rate by a factor of two compared to previously reported PM dual-color lasers system [79], which also helps to achieve a higher non-aliasing bandwidth (see Eq. 4.1). Since our laser is based on an ytterbium gain fiber, we reach a total output power of 9.2 mW, which is a factor of 5 higher than reported in previous PM dual-color lasers schemes based on erbium gain fibers. The power scaling potential of such Yb-based platforms makes them highly suitable for nonlinear wavelength conversion, which is a promising way to extend the wavelength coverage of dual-comb spectroscopy [19, 145].

4.2 Dual-comb setup

The mode-locking mechanism of our PM Yb:laser is based on the method described by Hänsel et al. [57], where a nonlinear amplifying loop mirror [53] is combined with a nonreciprocal phase shifter. NALM mode-locking has the important advantage that it does not rely on nonlinear polarization evolution, hence allowing the use of PM fibers. The PM fiber design decreases the sensitivity to environmental perturbations, leading to reliable, repeatable and self-starting mode-locked operation. The complete dual-comb setup is shown in Fig. 4.1. The laser consists of a fiber portion and a linear free-space arm. The fiber section includes a PM WDM, a 45-cm long PM-Yb:doped fiber (CorActive YB 401-PM) diode-pumped at 976 nm (BL976-PAG900) and a birefringent polarization beam combiner collimator (PBCC). The free-space arm involves a Faraday rotator (FR), two quarter wave plates (QWP), a half-wave plate (HWP), a polarization beam splitter cube (PBS) and a grating compressor (Wasatch Photonics, 800 lines/mm, angle-of-incidence 24.3° @ 1030 nm) GDD compensation. Spectral filtering is introduced in the grating compressor using a blade-shaped beam block [3]. In addition to the position, also the width of the spectral filter can be tuned by rotating the razor

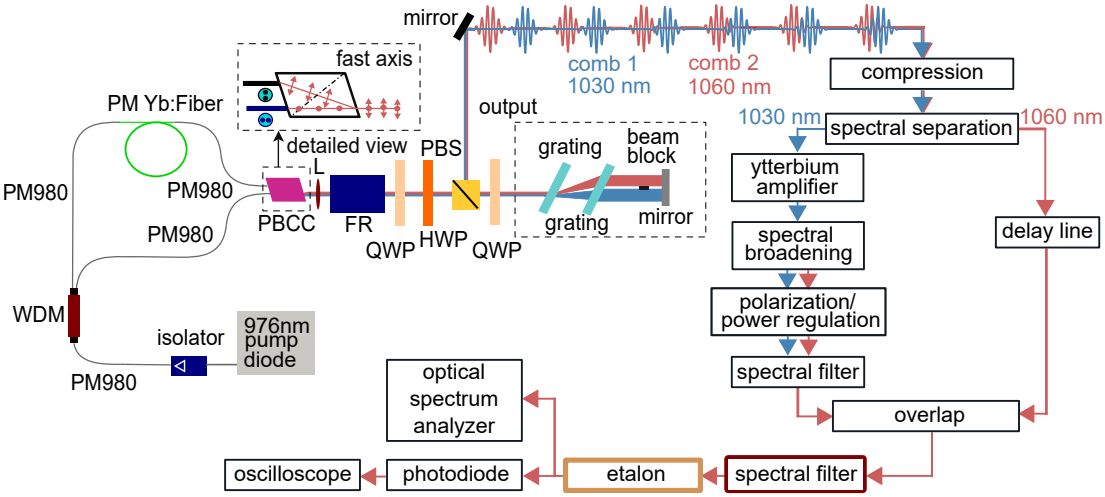

Figure 4.1 – Overview of the all-PM NALM mode-locked single-cavity dual-color/dual-comb setup. Due to the mechanical spectral filter, the laser oscillator emits two pulse trains with different repetition rates around 77 MHz and center wavelengths around 1030 nm and 1060 nm, respectively. The output of the dual-color laser is spectrally separated using a dichroic filter: The pulse centered around 1030 nm is amplified and nonlinearly broadened. The pulse centered around 1060 nm is delayed using a passive fiber. Subsequently, spatial overlapping in a 50:50 fiber splitter/combiner leads to the generation of a dual-comb interferogram. Bandpass filtering of the light is applied to avoid spectral aliasing. The feasibility of spectral measurement is demonstrated by measuring the transmission of different etalons. The light is detected by a simple photodiode and measured with an oscilloscope.

blade. The effective width of the beam block can be tuned in this manner from 0.075 mm and 2 mm.

By blocking the center part of the spatially dispersed light in the grating compressor, we force the laser to emit light in two separate regions of its gain spectrum. The operation point is initially found by rotating the wave plates and ramping up the pump power until both spectral regions mode-lock individually. Note that once the optimum wave plate position has been found, the wave plates can be clamped and no additional wave plate rotation is required when cycling the laser on and off. Dual-comb operation is initiated in a reproducible way, which does not take longer than 30 seconds: we shift the spectral filter to 1010 nm and ramp up the pump power until the laser mode-locks in single-comb operation. We then use the spectral filter to shift the center wavelength of the pulse to longer wavelengths until continuous wave lasing and finally also mode-locking occurs at the lower center wavelength on the other side of the beam block. We subsequently decrease the pump current until clean single-pulse operation is reached for each center wave-

length. The absence of parasitic multi-pulsing is then confirmed by checking that only one interferogram is visible on the oscilloscope within Δt=$1/\Delta f_{\mathrm{rep}}$. Once dual-comb operation has been initiated, it runs stably for days.

4.3 Dual-color operation regimes

Our all-PM dual-color laser emits two pulse trains with slightly different repetition rates (Δf_{rep} ≈1 kHz-10 kHz) around ≈77 MHz. Changing the grating separation leads to a change in the intra-cavity group delay and GDD, and hence enables us to tune the difference in repetition rates. Figure 4.2 shows the dual-comb operating at three different grating separations, i.e. with Δf_{rep} = 1.2 kHz, 2.6 kHz and 9 kHz kHz. At Δf_{rep} = 1.2 kHz, the non-aliasing bandwidth amounts to 2.4 THz, corresponding to about 10 nm at a center wavelength of 1060 nm, which is more than 2.5 times higher than reported for previous PM dual-color/dual-comb setups.

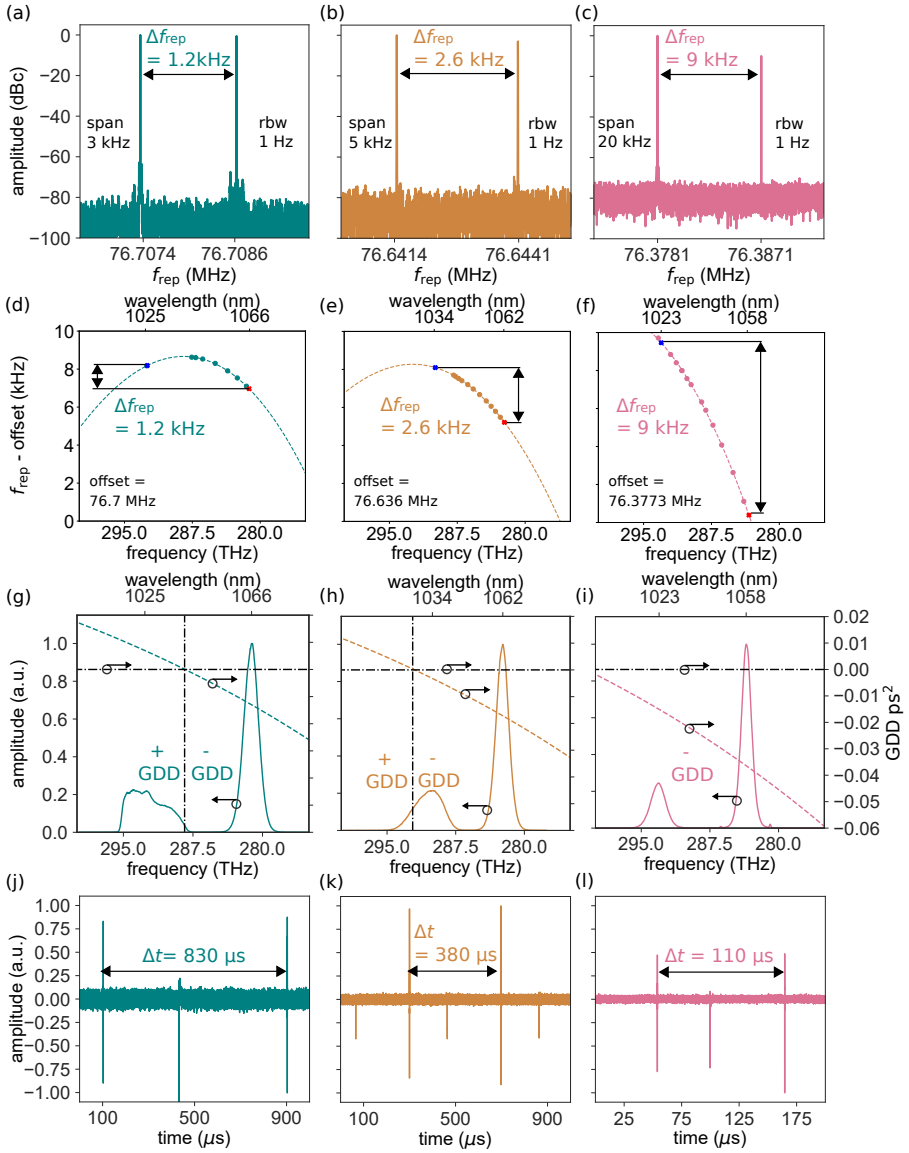

Figure 4.2 – Dual-comb setup operating with three different grating separations, i.e. different values of Δf_{rep}, resulting in either higher non-aliasing bandwidth or faster acquisition times. (a-c) Radio frequency trace of the laser outputs recorded with a Keysight PXA N9030B. (d-f) Wavelength-dependence of the repetition rate: the dots mark the measurement points, the dashed line shows the second-order polynomial fit. (g-i) Optical output spectra before spectral separation recorded with an optical spectrum analyzer (ANDO AQ6315A) and measured intra cavity dispersion. The dashed black lines show the zero-GDD crossing points. (j-l) Time trace recorded on an oscilloscope (LeCroy WavePro 760Zi) showing the interferograms that are separated in time by $\Delta t{=}1/\Delta f_{\mathrm{rep}}$. The spurious signals between the interferograms are the result of intra-cavity pulse collisions and is discussed in section 4.4.1.

We measured the intra-cavity dispersion using a technique described by Knox [82]. Since our laser cavity already contains a built-in spectral manipulator, we used it to shift the center wavelength λ_c of the laser (in single pulse/color mode) to different spectral positions within the laser gain bandwidth and recorded the repetition rate of the pulses using a spectrum analyzer with a resolution bandwidth of 1 Hz (see Fig. 4.2(d)-4.2(f)). We calculated the wavelength dependent group delay

$$\frac{\partial\phi}{\partial\omega} = T_{\mathrm{g}}(\lambda_{\mathrm{c}}) = \frac{1}{f_{\mathrm{rep}}(\lambda_{\mathrm{c}})}, \tag{4.2}$$

and fitted the data with a second-order polynomial. The first derivative of this fit then yields the corresponding GDD, i.e.

$$\frac{\partial^2\phi}{\partial\omega^2} = \frac{\partial T_{\mathrm{g}}}{\partial\omega} = \frac{\partial T_{\mathrm{g}}}{\partial\lambda}\frac{\partial\lambda}{\partial\omega} = -\frac{\lambda^2}{2\pi c}\frac{\partial T_{\mathrm{g}}}{\partial\lambda}, \tag{4.3}$$

where ω denotes the angular frequency, λ is the wavelength and c is the speed of light. Figures 4.2(g)-(i) show the intra-cavity GDD and the dual-color output spectra for the three operation points mentioned above. For the operation point with the largest grating separation (Fig. 4.2(i)), both pulses propagate in the negative (i.e. anomalous) dispersion regime and show soliton-like sech^2-shaped spectra. However, when reducing the grating distance, the intra-cavity dispersion crosses zero right between the two different spectra of the pulses. Consequently, while the pulse centered around 1060 nm is still running in the negative dispersion regime, the pulse centered around 1030 nm operates in the positive dispersion regime and is spectrally broader. The difference in repetition rates Δf_{rep} is given by the center wavelengths of the pulse trains and the dispersion profile of the laser. In the current laser configuration, we reached stable dual-color operation for a Δf_{rep} between 1 kHz and 10 kHz. While in theory, Δf_{rep} can be made arbitrarily small by engineering the dispersion profile and tuning the grating separation, the practical limitation will ultimately be given by gain competition of the two pulse trains inside the gain fiber.

4.4 Dual-comb characterization

In the following, we will focus on describing the dual-comb operation point at Δf_{rep} = 2.6 kHz (Fig. 4.2(b)), which provides a compromise between non-aliasing bandwidth and acquisition time. The two pulse trains are spectrally located around 1030 nm (comb 1, blue in Fig. 4.3 and subsequent figures) and 1060 nm (comb 2, red). The two pulses have a FWHM of ≈15 nm (pulse @ 1030 nm) and ≈7 nm

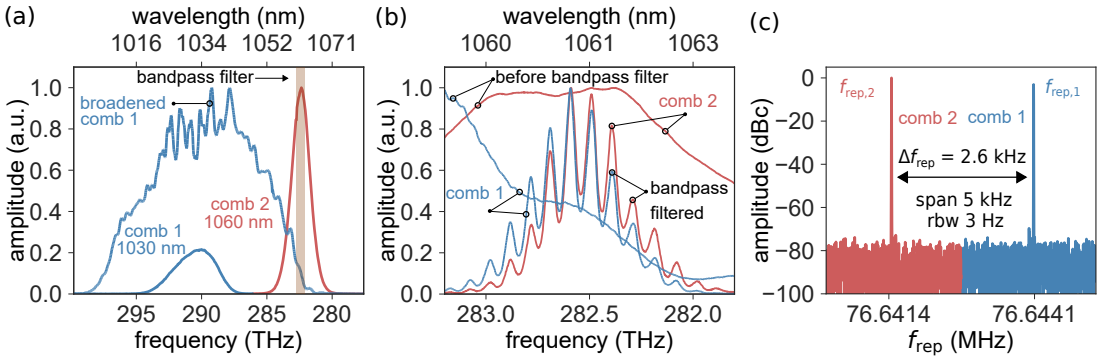

Figure 4.3 – (a) Output spectrum of the dual-color laser before spectral separation and spectrum of the broadened 1030-nm pulse recorded with an optical spectrum analyzer (ANDO AQ6315A). (b) Spatially overlapped dual-comb output after amplification and spectral broadening, before and after filtering the light using a 3-nm bandpass filter. The modulations on the spectrum are caused by the bandpass filter. (c) Radio frequency spectrum of the laser output. Note that the data shown represents one measurement and that the coloring is merely a guide to the eye.

(pulse @ 1060 nm), see Fig. 4.3(a). After the cavity, the two pulses are simultaneously compressed by a grating compressor. To avoid any crosstalk between the two pulse trains during amplification and nonlinear broadening, we separate the two pulses after the grating compressor using a short-pass filter with a cut-off wavelength of 1050 nm. The pulse centered around 1030 nm is amplified in a PM single-mode amplifier and spectrally broadened using a nonlinear fiber (NKT-SC-5.0-1040) directly spliced to the amplifier. The nonlinearly broadened spectrum is shown in Fig. 4.3(a). After spectral broadening, the light is coupled out into a free-space section. Since the nonlinear fiber is not PM, we use a quarter-wave plate, a half-wave plate and a PBS to linearly polarize the light. The half-wave plate in combination with the PBS is also used to attenuate the amplified and spectrally broadened light to optimize the contrast of the beating signal. To filter out the spectral components which are not overlapping with the pulse centered around 1060 nm we use an additional long pass filter with a cut-on wavelength of 1050 nm. The two now spectrally overlapped pulses are then spatially overlapped in a 50:50 fiber coupler. Nonlinear effects in the fiber coupler are not critical, since at this point in the setup we have an average power per pulse train of 1-2 mW and due to dispersion in the previous fiber section (amplifier and delay line), the pulses are not compressed anymore. With a nominal repetition rate $f_{\mathrm{rep},1}$ around 77 MHz, a difference between the two repetition rates of Δf_{rep} ≈2.6 kHz, the non-aliasing dual-comb spectral bandwidth is calculated to be ≈1.2 THz, which corresponds to ≈4 nm around a center wavelength of 1063 nm. To avoid aliasing, we bandpass-

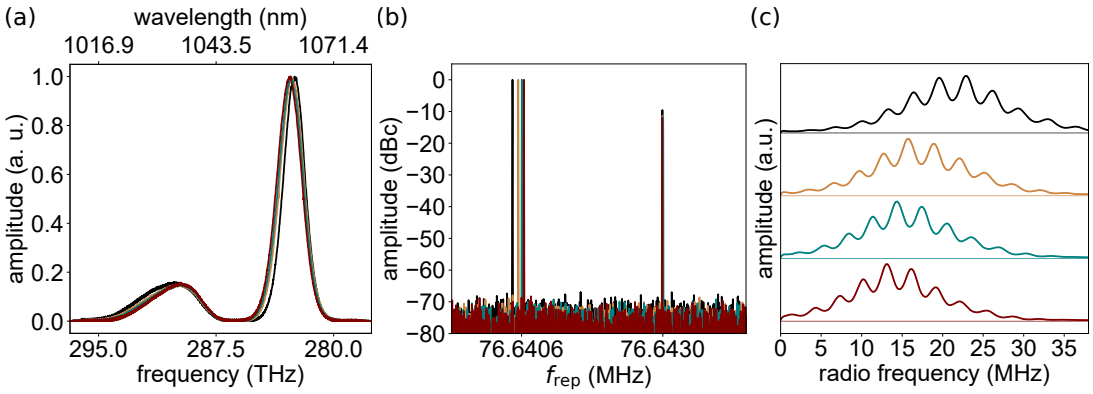

Figure 4.4 – (a) Spectral shift occurring when slightly changing the position of the beam block within the grating compressor using a micrometer screw. (b) Corresponding changes in the repetition rates due to the shift of the spectral filter. (c) Shift of the down-converted frequency comb along the radio-frequency axis.

filter the light around a center wavelength of 1063 nm with a FWHM of 3 nm. This filter imprints a modulation on the spectra of the two combs, see Fig. 4.2(c), which however does not impact the spectroscopy experiments as it cancels out when doing a baseline subtraction (see section 7). Finally, we measure the light using a simple photodiode (Thorlabs PDA05CF2), whose signal is then low-pass filtered (48 MHz) to remove the individual comb repetition rates $f_{\mathrm{rep},1}$ and $f_{\mathrm{rep},2}$ before being recorded on an oscilloscope (LeCroy WavePro 760Zi). Figure 4.2(h) shows an example of an oscilloscope time trace with the interferograms occurring with a periodicity of $\mathrm{T} = 1/\Delta f_{\mathrm{rep}} = 380\,\mu\mathrm{s}$. Note that the spurious signals appearing between the interferograms will be discussed in the next section below.

By performing a fast Fourier-transform on the single interferograms, we can retrieve the down-converted radio-frequency spectra. In order to exploit the full non-aliasing bandwidth in spectroscopy experiments, i.e. to avoid interference with higher-order down-converted frequency combs, the center of this down-converted radio frequency should ideally be located at $f_{\mathrm{rep}}/4$. The absolute position of the down-converted comb is related to the difference in CEO frequency of the two combs and is usually not an easily accessible parameter. In this setup however, the mechanical spectral filter can be exploited to tune the down-converted radio frequency comb. The mechanism can be explained as follows: slightly tuning the beam block position results in small changes of the center wavelength of the two pulses, (see Fig. 4.4(a)), as well as in their corresponding repetition rates (Fig. 4.4(b)). The shift is more pronounced for the 1060-nm pulse, which lies further from the cavity zero-dispersion point (see Fig. 4.2(h)). Although the wavelength shifts are small, they induce a relative change in the dispersion experienced

by the two pulses. As a consequence, the difference in CEO changes, which allows for the down-converted radio frequency comb to be shifted considerably along the radio frequency axis (Fig. 4.4(c)). This useful feature is an additional advantage of mechanical filtering and was exploited to make use of the full theoretical non-aliasing bandwidth in the dual-comb measurements that will be presented in section 4.5.

4.4.1 Intra-cavity cross-talk

Dual-color fiber lasers are known to show amplitude fluctuations, which are generated by cross-talk caused by collisions of the two pulses inside the laser cavity [85]. However, the pulses inside the laser cavity recover and only a small temporal portion of the laser output is affected by this phenomenon.

Figure 4.5(a) shows the time domain output of our dual-comb system. In addition to the interferograms generated by optical beating between the two combs (Fig.4.5(a) green section), spurious signals can be seen (Figure 4.5(a) red section). This spurious signal is present on both pulse trains individually and corresponds to a temporary modulation of the pulse amplitudes caused by the intra-cavity pulse collision. The position of the spurious signals relative to the interferogram depends on the extra-cavity path length difference between the 1030 nm and the 1060 nm-arms. If both arms have the same length, the interferogram and the spurious signals are overlapping. A path length difference of Δl introduces a temporal shift Δt_l between the two pulse trains, i.e.

$$\Delta t_\mathrm{l} = \frac{\Delta l}{c}. \tag{4.4}$$

Hence, the position of the spurious signal from pulse train 1 will be shifted by Δt_l on the temporal axis relative to the position of the spurious signal from pulse train 2. At the same time, the position of the center burst of the interferogram changes by

$$\Delta t_\mathrm{s} = \frac{\Delta t_\mathrm{l}}{\Delta t_\mathrm{c}} \frac{1}{f_\mathrm{rep,1}}, \tag{4.5}$$

where Δt_c corresponds to the round-trip time difference between the 1030 nm and the 1060 nm pulses, i.e.

$$\Delta t_\mathrm{c} = |T_1 - T_2| = \left| \frac{1}{f_\mathrm{rep,1}} - \frac{1}{f_\mathrm{rep,2}} \right| = \left| \frac{\Delta f_\mathrm{rep}}{f_\mathrm{rep,1} f_\mathrm{rep,2}} \right|. \tag{4.6}$$

For nominal repetition rates around 77 MHz, a Δf_rep on the order of several kHz and a path length difference of some meters, Δt_l amounts to less than 10 ns (and is thus not visible in Fig. 4.5), while Δt_s on the other hand is on the order of a few

hundred microseconds. Hence, by introducing an appropriate extra-cavity path length difference between the two pulse trains, we can maximize the non-disturbed time window Δt_{w} around a center burst. This is important to maximize the resolution $\Delta\nu_{\mathrm{RF}}$ of the current dual-comb setup, since the resolution $\Delta\nu_{\mathrm{RF}}$ directly corresponds to the inverse of the measured time window Δt_{w} as a consequence of the Fourier transform linking the time and frequency domain.

Since amplitude noise can have a significant influence on the achievable signal-to-noise (SNR) in dual-comb measurements [146], we investigated the relative intensity noise (RIN) of the laser output at different positions in the setup: right after the spectral separation (before amplification and nonlinear broadening, see Fig. 4.6(a)), and right after amplification and nonlinear broadening (1030 nm pulse train) and the delay line (1060 nm pulse train), see Fig 4.6(b). The measurements were done by sending the beams onto a photodiode (PDA36-EC), low-pass filtering the output at 1.9 MHz and recording 100 time traces on a LeCroy WavePro 760Zi oscilloscope. The Fourier-transforms of the individual traces were averaged, corrected for the system noise floor and normalized by the DC-voltage output of the photodiode to yield the RIN spectra shown in Fig. 4.6. The amplitude noise caused by the intra-cavity pulse collisions is clearly visible in the RIN spectrum in the form of sharp peaks located at Δf_{rep}= 2.6 kHz and its integer multiples. These side-peaks around -80 dBc are also visible when hooking up the photodiode output to a radio frequency analyzer (Keysight PXA N9030B) and zooming into the repetition rate signal, provided that the latter is displayed with an SNR $>$ 80 dB (Fig. 4.6(c)).

There is a lack of RIN data in the literature for this kind of NALM Yb:lasers, even for standard single color/comb operation. However, we can compare our laser with well-documented state-of-the-art NPE mode-locked Yb:fiber lasers involving a free-space grating compressor for dispersion compensation [117]. For frequencies below 10 Hz, the RIN is about 10 to 20 dBc/Hz higher than reported in [117]. However, the noise at low frequencies can be significantly improved by increasing the stability of the free-space section by appropriate mechanical design. For frequencies above 10 Hz, the RIN is on the same order as for the other reported Yb:fiber lasers. The noise of the amplified and spectrally broadened light for low frequencies (mechanical vibrations) is the same as the low-frequency noise of the laser output, which is expected since the all-PM-fiber-amplifier design should not be influenced by mechanical vibrations. Above 100 Hz and especially for the cross-talk noise signals, a rise of the noise level due to amplification and nonlinear broadening is noticeable. This increase is on the same order of magnitude than described in previous amplifier systems [84].

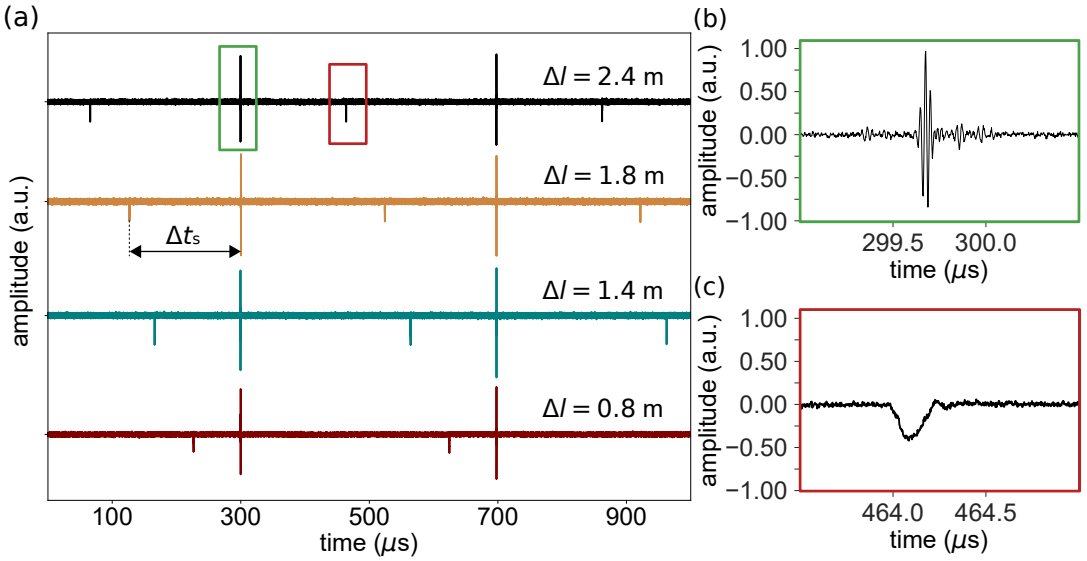

Figure 4.5 – (a) Time domain signal of the dual-comb recorded on an oscilloscope (LeCroy WavePro 760Zi). A linear interferogram can be seen (highlighted in green, zoom shown in (b)), as well as spurious signals caused by intra-cavity pulse collisions (highlighted in red, zoom shown in (c)). By changing the extra-cavity path length difference of the two arms (see setup in Fig. 4.1) the temporal position of the center burst can be shifted with respect to the position of the spurious signals.

4.4.2 Frequency stability

Another important property of the combs is their long-term frequency stability, in particular when the dual-comb system is meant to be used in a free-running state, i.e. without any active feedback. To characterize the long-term stability, we monitored the drift of the two repetition rates and their difference Δf_{rep} over a duration of 200 min, see Fig. 4.7(a). Although a drift in the individual repetition rates is recognizable (standard deviation $\sigma(f_{\mathrm{rep},1}) = 12\,\mathrm{Hz}$ and $\sigma(f_{\mathrm{rep},1}) = 13\,\mathrm{Hz}$), the drift of Δf_{rep} is nearly one order of magnitude smaller (standard deviation of $\sigma(\Delta f_{\mathrm{rep}}) = 1.7\,\mathrm{Hz}$, see Fig. 4.7(a)(b)). This remaining drift could be further reduced by increasing the mechanical stability of the free-space portion of the laser, but was already small enough to allow for first proof-of-principle experiments as presented in the next section.

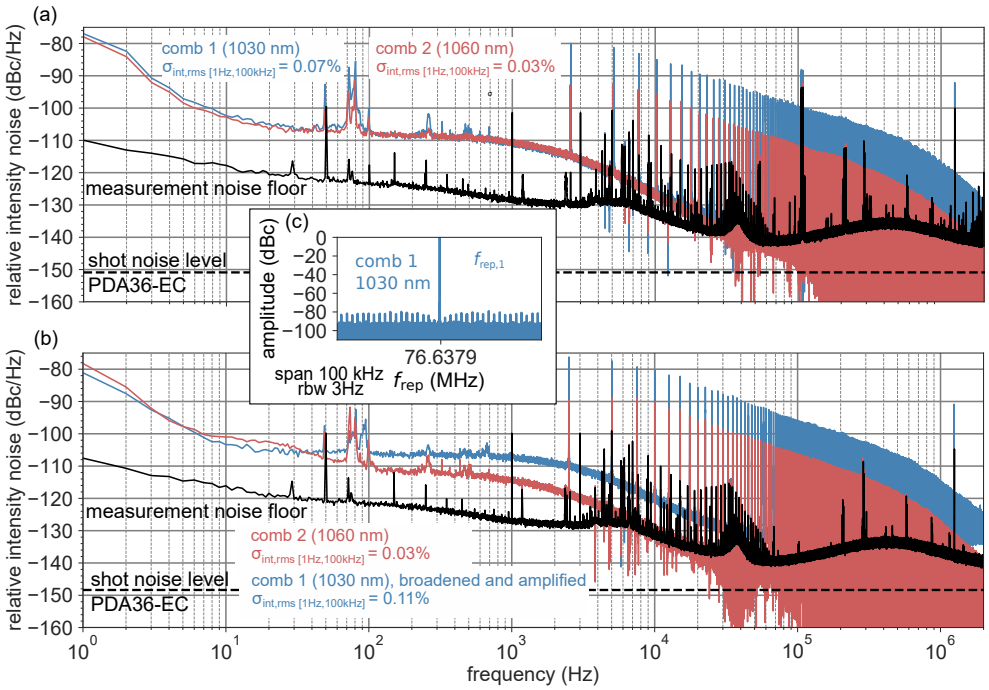

Figure 4.6 – (a) Relative intensity noise (RIN) of the spectrally separated combs measured before amplification including the root-means-quare (rms) RIN σint,rms integrated over the interval [1 Hz, 100 kHz]. (b) RIN of the spectrally separated laser output after amplification and broadening including the root-means-quare (rms) RIN σint,rms integrated over the interval [1 Hz, 100 kHz]. (c) Radio frequency spectrum of the broadened 1030 nm pulse train, showing a span of 100 kHz around the repetition rate signal with a resolution of 3 Hz.

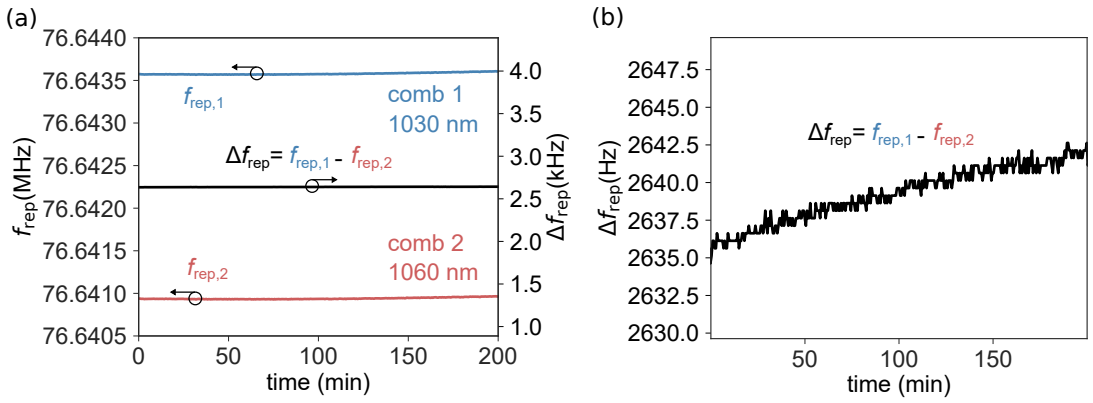

Figure 4.7 – (a) Drift of the individual repetition rate $f_{\mathrm{rep},1}$ and $f_{\mathrm{rep},2}$ as well as the difference Δf_{rep} over 200 min, measured with a radio frequency analyzer (Keysight N9030B PXA). (b) Zoom into the drift of Δf_{rep}.

4.5 Etalon transmission measurement

To demonstrate the viability of spectral measurements, we measured the transmission of two etalons: an uncoated 700-μm thick gallium arsenide (GaAs) wafer and a 5-mm thick zinc selenide (ZnSe) window. For these measurements, 100 single bursts were recorded with a window size of 10 µs (GaAs) and 200 µs (ZnSe). These time traces were Fourier-transformed and averaged in the spectral domain directly using the built-in Fast-Fourier-Transform (FFT) and averaging functions of the LeCroy WavePro 760Zi oscilloscope (Fig. 4.8(a) and 4.8(e) orange curve). The data was then background-corrected and divided by a reference measurement (same measurement but without the etalon, Fig. 4.8(a) brown curve). In Fig. 4.8(b), we show that the measured fringes are in good agreement with the theoretical transmission calculated for a 700-μm (GaAs) etalon (reflectivity $R = 0.30568$, refractive index $n = 3.4731$ at 1063 nm [147]). As a sanity check and to obtain an absolute wavelength calibration, we also recorded the spectra in parallel with a calibrated grating-based optical spectrum analyzer (ANDO AQ6315A) that has a maximum resolution of 0.05 nm (Fig. 4.8(c)). Already in the case of the 700-μm thick GaAs sample, the resolution of the spectrum analyzer is insufficient to fully resolve the etalon transmission, which then leads to a slight discrepancy between the theoretical etalon curve and the transmission measured by the spectrum analyzer (Fig. 4.8(d)). In the case of the much thicker ZnSe etalon, the transmission fringes are beyond the resolution of the spectrum analyzer. However, the fringes measured with the dual-comb are again in good agreement with the theoretical transmission calculated for a 5-mm ZnSe etalon (reflectivity $R = 0.178$, refractive index $n = 2.458$ at 1063 nm [148]) (Fig. 4.8(f)).The 200-μs window chosen to measure the ZnSe etalon implies a radio frequency resolution of 5 kHz. With a difference in repetition rate Δf_{rep} of 2.6 kHz and a nominal repetition rate f_{rep} of 77 MHz, this corresponds to an optical frequency resolution of 148 MHz. In order to obtain comb-line-limited resolution, the temporal window would need to be at least as long as $1/\Delta f_{\mathrm{rep}} = 384$ µs. Since the spurious signals would be included in that case, some manipulation of the time window would be required to eliminate their influence. However, a manipulation such as zero-padding the spurious signals may obscure important spectral details in more complex spectroscopy measurements. Hence, a cleaner path towards achieving true comb-tooth resolution with this system would be to eliminate the spurious signals in a balanced-detection scheme, where half of the dual-comb light is sent through the sample, while the other half simultaneously provides a baseline-signal.

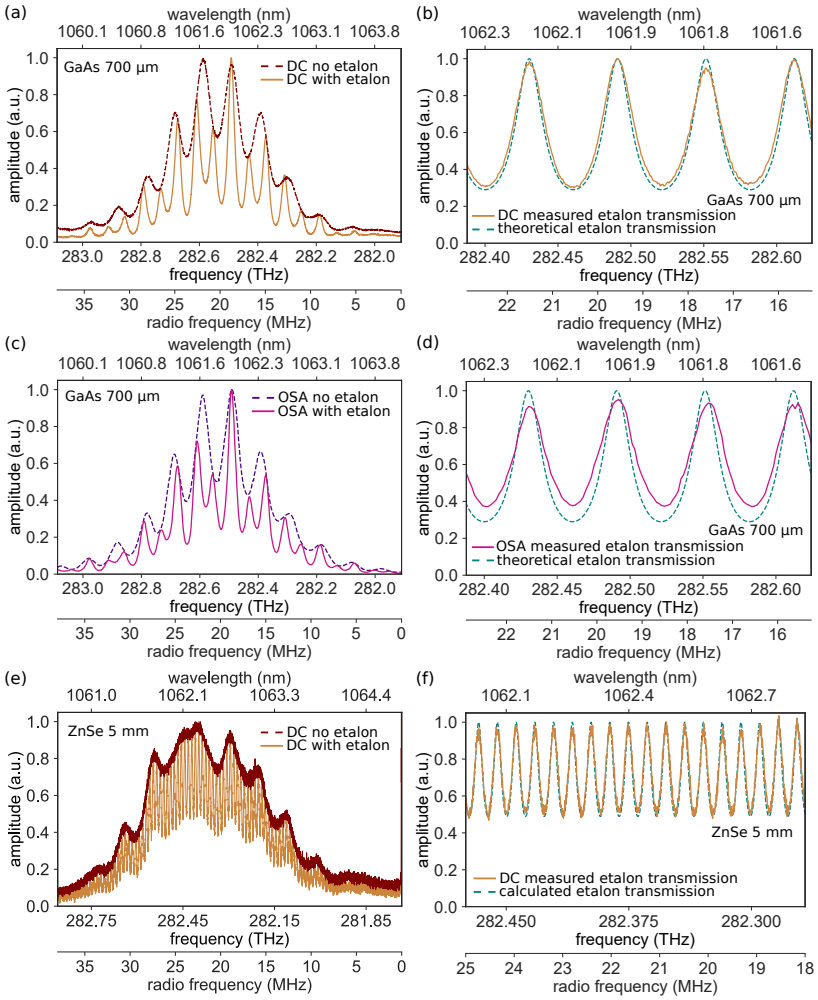

Figure 4.8 – Etalon transmission measurements. (a) Spectrum re-constructed from the dual-comb interferogram by averaging the FFTs of 100 single interferograms recorded in time windows of 10 µs each after a 3-nm band pass filter with and without a 700-μm GaAs etalon. (b) Measured transmission spectrum (orange, solid) obtained after background subtraction and division by the reference spectrum without the etalon, as well as theoretically calculated transmission function for a 700-μm GaAs wafer (turquoise, dashed). (c) Same measurement performed with an optical spectrum analyzer that has a maximum resolution of 0.05 nm (ANDO AQ6315A). This measurement was perfromed to obtain an absolute wavelength calibration for the spectra retrieved from the dual-comb data. Due to the limited resolution, the ANDO is not capable of fully resolving the fringes, as can be seen in (d). (e) Spectrum re-constructed from the dual-comb interferogram by averaging the FFTs of 100 single interferograms recorded in time windows of 200 µs each after a 3-nm band pass filter with and without a 5-mm ZnSe window. (d) Measured transmission spectrum (orange, solid) obtained after background subtraction and division by the reference spectrum without the etalon, as well as theoretically calculated transmission function for a 5-mm ZnSe window (turquoise, dashed).

4.6 Conclusion and outlook

In summary, we have presented a novel method to obtain dual-color/dual-comb operation from a single all-PM Yb:mode-locked fiber laser. The method is based on mechanical spectral filtering and offers two main features: easy tuning of the difference in repetition rates (and hence of the tradeoff between non-aliasing bandwidth and measurement time), as well as the possibility to shift the down-converted frequency comb on the radio frequency axis by slightly tuning the position of the mechanical filter. Compared to previous all-PM single-cavity dual-color lasers based on erbium, we increased the nonaliasing bandwith by a factor of 2.5. Furthermore, we reached a factor of 5 higher output power than reported previously due to the high gain achievable in ytterbium gain fibers.

The combination of a fiber section exhibiting positive dispersion at 1 μm with a grating compression providing tunable negative GDD offers the possibility to make this laser run in different dispersion regimes. The impact of the dispersion regime on amplitude and frequency noise has been studied for NPE mode-locked fiber lasers [117], however no such study has been carried out yet for NALM lasers (let alone dual-color NALM lasers) to the best of our knowledge.

Additionally, it is an open question whether and how the intra-cavity pulse collisions are influenced by the dispersion regime since pulse collisions have only been studied for dual-color solitons [85]. A detailed noise analysis for the different dispersion regimes of NALM lasers with nonreciprocal phase shifter in single- and dual-color mode has the potential to provide interesting insights. However, this is beyond the scope of this paper and will need to be addressed in future work.

The most straight-forward way to improve the non-aliasing bandwidth of our dual-comb setup would be to increase the repetition rate of our laser. The current setup was pump-power limited, i.e. to obtain the same peak power for stable mode-locking of the two pulse trains at higher repetition rates, more pump power would need to be provided in the future.

The viability of our current setup was demonstrated in a proof-of-principle experiment by resolving the transmission fringes of two etalons (700-μm thick GaAs and 5-mm thick ZnSe) without the need for active stabilization of the comb parameters. In combination with recent work on computational averaging techniques [149], we believe that free-running single-cavity dual-comb approaches such as the one presented here are a promising path towards robust and compact high-precision spectrometers.

Funding

Austrian Federal Ministry for Digital and Economic Affairs; National Foundation for Research, Technology and Development; Austrian Science Fund (FWF) (M2561-N36).

Acknowledgment

The authors would like to acknowledge Garrett Cole and Dominic Bachmann for fruitful discussions and helpful comments on the manuscript, as well as Nikolai Kiesel and Markus Aspelmeyer for supporting us with measurement equipment.

4.7 Non-published supplementary material

4.7.1 Increasing the non-aliasing bandwidth

To increase the non-aliasing bandwidth of our laser setup, we can turn two knobs (see Eq. 1.51): the nominal repetition rates of the two pulse trains, as well as the difference in repetition rate Δf_{rep}.

Increasing the repetition rate

In a first approach, we decided to increase the repetition rate of our dual-comb setup step-by-step. Due to the quadratic dependence of the non-aliasing bandwidth on the repetition rate, repetition rate scaling is a promising approach to increase the non-aliasing bandwidth. The updated setup containing a shorter fiber section than the laser presented in paper 3 and can be seen in Fig. 4.9 (a). This updated dual-color laser has a repetition rate of 92 MHz. This modification leads to an 40% increment of the non-aliasing bandwidth under the assumption of Δf_{rep}-values similar to publication 3.

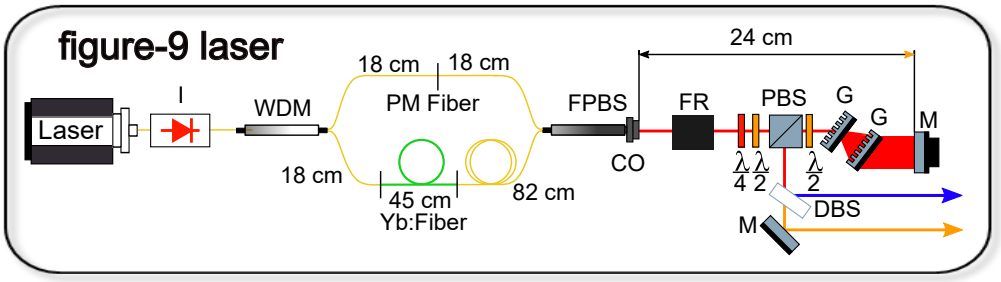

Figure 4.9 – 92-MHz figure-9 dual-color laser: (a) Setup with detailed length specifications of the resonator. WDM: wavelength division multiplexer, I: Isolator, FPBS: collimating beam combiner, FR: Faraday rotator, PBS: polarizing beam splitter, G: grating, M: mirror.

Decreasing Δf_{rep}

The difference in repetition rate of the dual-colour figure-9 laser is given by the center wavelengths of the individual pulse trains and the wavelength-dependent group delay inside the laser resonator. Different approaches can lead to a decrease in Δf_{rep}, see Fig 4.10.

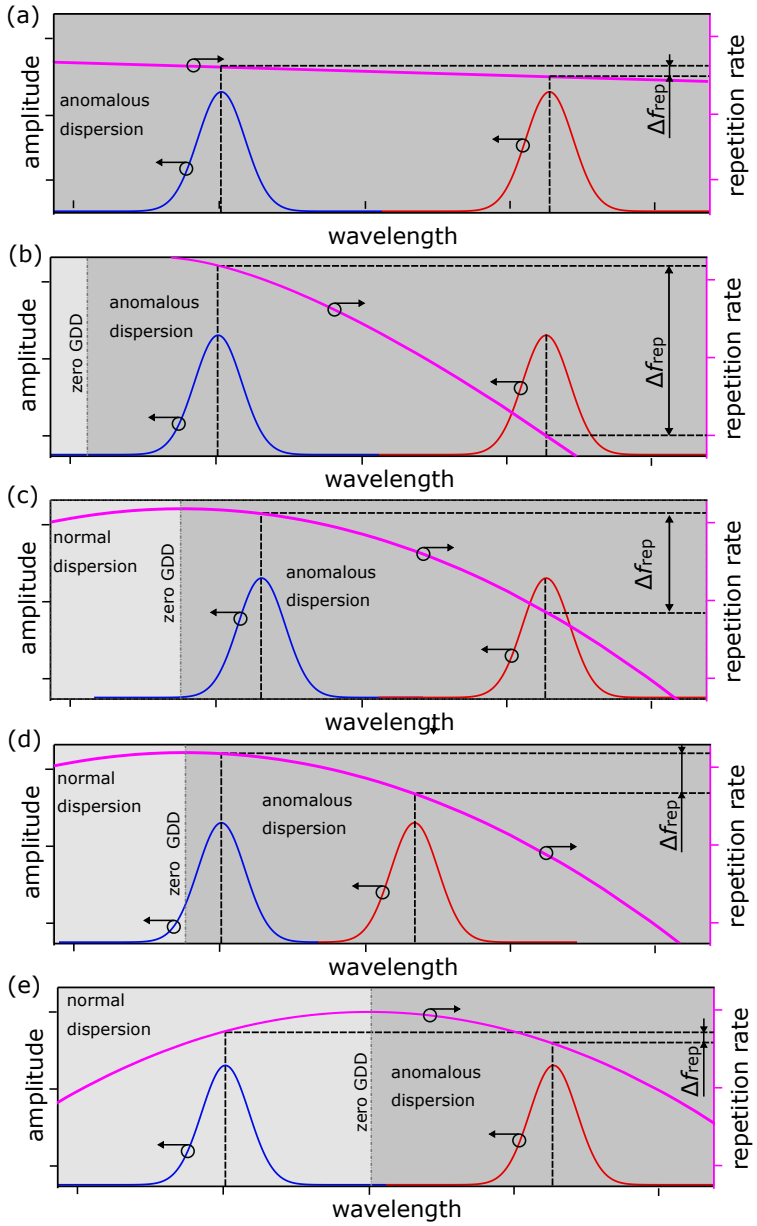

Figure 4.10 – Δf_{rep} tuning. (a) The ideal case for dual-color operation: the repetition rate has a slight wavelength dependence resulting in a small Δf_{rep}. (b) Actual case for anomalous dispersion in reality: typically, the repetition rate strongly depends on the wavelength, leading to a large difference in repetition rate. (c) Operation with the short-wavelength pulse close to zero-dispersion (still anomalous): due to the flattening of the wavelength dependency of the repetition rate, Δf_{rep} decreases when operating closer to zero dispersion. (d) If the two pulses operate in the same dispersion regime, Δf_{rep} can also be decreased by minimizing the wavelength separation of the two pulse trains. (e) The case where one of the pulse trains is operating in the anomalous dispersion regime while the second one is operating in the normal dispersion regime: theoretically, this operation regime would even enable zero Δf_{rep}. It is also the state that offered the smallest Δf_{rep} in our experiments.

In paper 3, we presented different operation points of our dual-color figure-9 laser. By tuning the grating distance of the intracavity grating compressor we could tune Δf_{rep} from 1.2 kHz to 9 kHz. At this point, we however did not investigate whether it was possible to decrease Δf_{rep} even further by optimizing all other handles of the laser. As discussed in chapter 2 and chapter 3 the laser design presented here offers several tuning possibilities:

- Intracavity dispersion
- Cavity losses
- Phase bias
- Modulation depth of the saturable-absorber
- Splitting ratio of the NALM
- Pump power
- Width of the spectral filter
- Position of the spectral filter

Anomalous dispersion operation state: As a first approach, we minimized Δf_{rep} for the operation point where both pulses are working in the anomalous dispersion regime (Fig. 4.10(b)). The dual-color laser could be mode-locked with a Δf_{rep} of around 2.3 kHz. When the grating separation was further slightly decreased (while the laser was off), mode-locked dual-color operation could not be achieved anymore. Also, decreasing the width of the spectral filter only led to a state where no dual-color operation could be obtained. However, when the laser was mode-locked in dual-color operation with a Δf_{rep} of around 2.3 kHz, "online" tuning allowed us to even further decrease Δf_{rep}; i.e. minimization could be achieved by changing the grating separation while the laser was running. This dispersion tuning not only changes the slope of the wavelength-dependence of the repetition rate, but also shifts the center wavelength of the shorter-wavelength-pulse towards longer wavelengths (Fig. 4.10(c)). We could observe this behaviour also in our single-comb laser; once the laser was mode-locked on one side of zero-dispersion the zero line acts as a "barrier" for the pulse. By shifting the zero-dispersion point to longer wavelengths, the center wavelength of the pulse can be pushed to longer wavelengths. This behavior can be exploited to achieve a smaller wavelength separation between the two pulses. Subsequently, we increased the cavity losses by rotating the output coupling wave plate. This wave plate rotation

forced the pulse operating at longer wavelengths to shift to shorter wavelengths, since Ytterbium offers more gain for this wavelength region, which in turn leads to a further decrease of the spectral separation and hence Δf_{rep} (Fig. 4.10(d)). With this optimization, we reached a minimum Δf_{rep} value of 1.4 kHz for this operation point, see Fig. 4.12.

The fact that the spectral separation can be tuned without changing the width of the mechanical filter suggests that the actual spectral filtering is the result of a complex interaction between the losses introduced by the mechanical filter and the laser dynamics. This behaviour may only be fully understood when performing an extensive numerical simulation.

Operating with both pulses in the anomalous dispersion regime has several drawbacks: due to the online tuning necessary to reach a small Δf_{rep}, the laser cannot be started in the configuration in which it is operating, resulting in an complex starting procedure. Additionally, due to the small wavelength separation, it is not straight forward to separate the two pulse trains, which is essential for further wavelength conversion and the generation of a dual-comb.

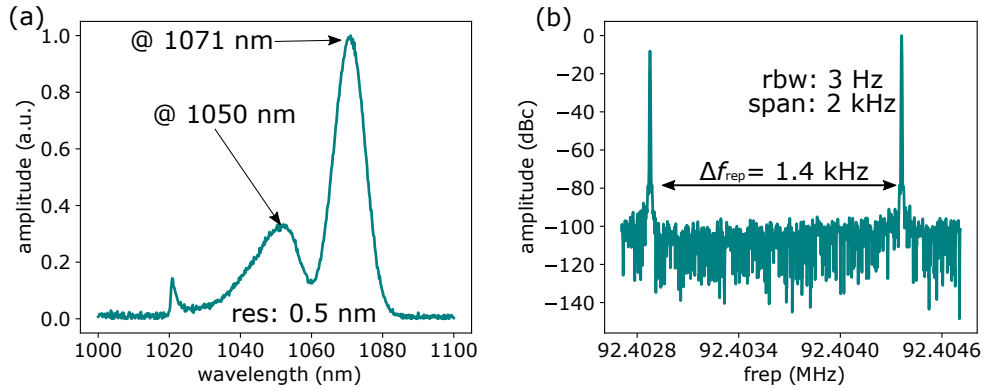

Figure 4.11 – 92-MHz figure-9 dual-color laser state with both pulses operating in the anomalous dispersion regime (a) Optical output spectrum. (b) Zoom into the repetition rates of the two pulse trains.

Anomalous and normal dispersion operation state: In this state, one of the pulse trains is operation in the positive dispersion regime while the other one is operating in the negative dispersion regime, as described in Fig. 4.10(e). In this state, Δf_{rep} can theoretically be set to zero. However, we observed that the smaller Δf_{rep} is set, the more sensitive the laser gets to environmental perturbations. We think that this higher sensitivity is caused by gain competition between the two pulse, which becomes more critical when the pulses co-propagate for a longer period of time inside the fiber section due to the smaller Δf_{rep}.

In this operation state we could decrease the difference in repetition rate down to 670 Hz. However, already with this Δf_{rep}, it was difficult to operate the laser in a stable manner without parasitic multi-pulses. An additional drawback of this state was that it offered only an output power of ≈ 0.2 mW for the laser pulse operation at longer wavelength (> 1070 nm). This combination of center wavelength and output power is challenging when it comes to further amplification.

To operate the laser in a reliable, easy-to-start operation point with higher output powers, we set Δf_{rep} to 1.5 kHz. In this configuration, one pulse train has a center wavelength of around 1010 nm (at normal dispersion), while the second one operates around 1085 nm (at anomalous dispersion), see Fig. 4.12. This operation point enables a clean separation of the two pulse trains using a dichroic mirror, due to the large wavelength separation. For the pulse operating around 1010 nm, we obtained an output power of ≈ 8 mW, while for the pulse operating around 1085 nm, we reached an output power of ≈ 2 mW.

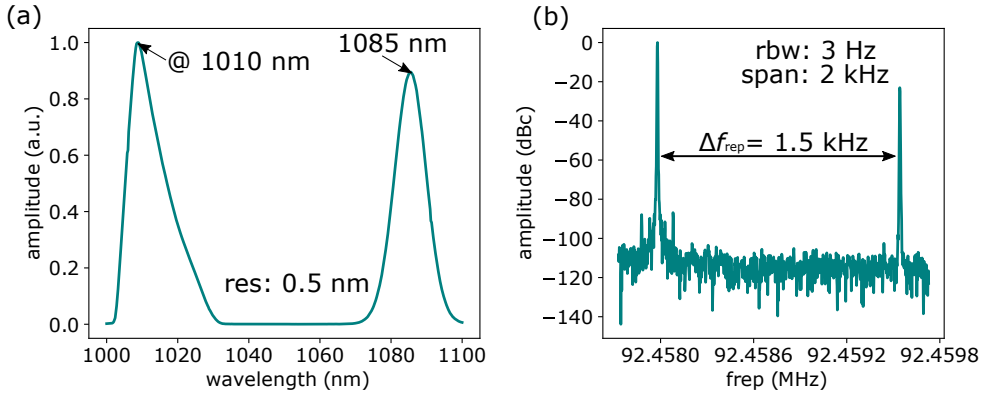

Figure 4.12 – 92-MHz figure-9 dual-color laser state with one pulses operating in the anomalous dispersion regime (centred around 1085 nm) and one pulse in the normal dispersion regime centred around 1010 nm. (a) Optical output spectrum. (b) Zoom into the repetition rates of the two pulse trains.

4.7.2 Increasing the spectral coverage

In publication 3, we performed nonlinear wavelength conversion to generate a dual-comb out of our single-cavity dual-color laser. We broadened one of the pulse trains to spectrally overlap with the second one. However, by nonlinear wavelength conversion of both pulse trains, the dual-comb can also be shifted to different wavelengths.

As a proof of principle experiment, we increased our dual-comb's spectral coverage by nonlinear wavelength conversion via Raman soliton self-frequency shift

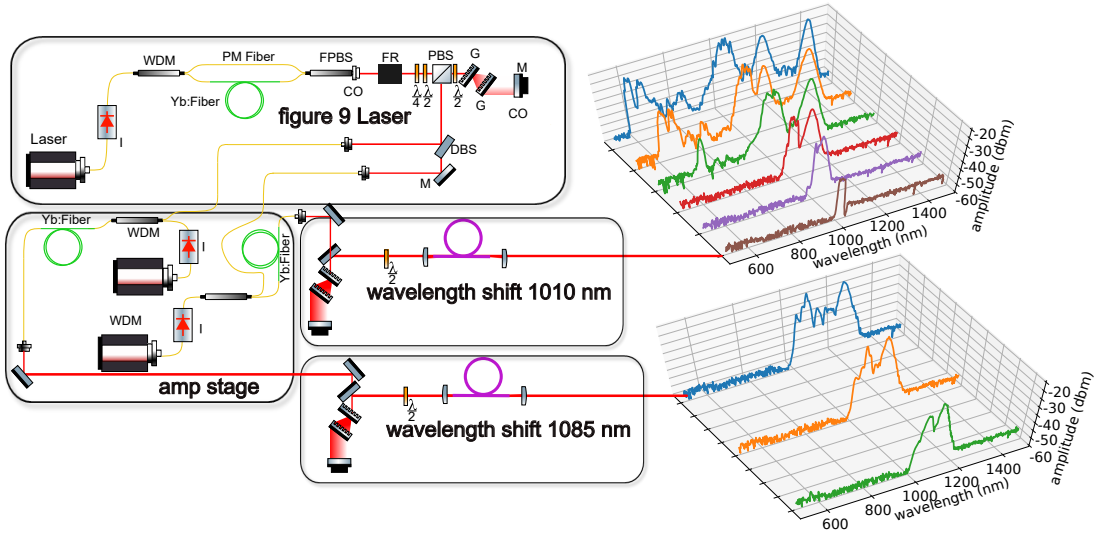

Figure 4.13 – Increasing the spectral coverage of the dual-comb setup. (a) Experimental setup: the output of the dual-color laser is separated via a dichroic mirror. The two pulse trains are amplified in an ytterbium-doped single-mode amplifier. The output of the amplifier is then coupled into a nonlinear PCF fiber. (b) Spectra of the nonlinearly broadened pulse with an initial center wavelength of 1010 nm. (c) Spectra of the nonlinearly broadened pulse with an initial center wavelength of 1085 nm.

inside a nonlinear fiber. The operation point is characterized in Fig. 4.11. We reached a non-aliasing bandwidth of around ≈ 3 THz with this configuration, corresponding to ≈ 12 nm at a center wavelength around 1085 nm. The nonlinear fiber was provided by Grzegorz Sobon (Wroclaw University, Poland); for more details see [150]. We separated the two pulse trains coupled out of the laser using a dichroic mirror to prepare for the wavelength conversion. Clean wavelength separation is of significant importance for further amplification: imperfect separation would lead to gain competition inside the amplifier. Each pulse train is amplified in an ytterbium-doped single-mode amplifier. However, due to the different input powers and the wavelength-dependent gain inside the amplifier, we reached different maximum power levels for the two different pulse trains. For the pulse train centered around 1010 nm we reached an output power of around 350 mW. For the pulse centered around 1085 mW we got a maximum output power of 130 mW. After amplification, we compressed the pulses using a grating compressor. The gratings used have an efficiency of around 94% for the 1010 nm pulses and of around 90% for the 1085 nm pulses. After compression, we coupled each pulse train into the nonlinear fiber with a coupling efficiency of around 50%. Hence, we had a maximum coupled power of 140 mW for the 1010-nm pulse train and 45 mW for the 1085-nm pulse train. With these input power levels, we could shift

the short-wavelength pulses up to a center wavelength 1420 nm, see Fig. 4.13 (b). Due to the lower power of the pulse train at longer wavelengths, the latter could only be shifted up to 1250 nm. However, using an additional amplification stage should enable to extend the spectral coverage to even longer wavelengths.

The results of this experiment represent the first step towards extending the spectral coverage of our dual-comb into the mid-IR using difference frequency generation [150].

Chapter 5

Conclusion and Outlook

"The end? No, the journey doesn't end here. Death is just another path, one that we all must take. The grey rain-curtain of this world rolls back, and all turns to silver glass, and then you see it."

Gandalf the White, The Lord of the Rings

5.1 Summary

In this thesis, I have presented our research on versatile and robust Yb:fiber lasers for single and dual-comb applications. In **publication 1**, we showed for the first time, that a mechanical spectral filter can be used to achieve dual-color operation in a single fiber laser cavity. We generated two pulse trains out of an ytterbium-doped NPR laser with slightly different repetition rates around a nominal repetition rate of 23 MHz. Each pulse train had a spectral width of around 10 nm. In contrast to previous demonstrations that used a fiber Bragg grating, our mechanical spectral filter can be tuned both in terms of the center wavelength as well as the width of the blocked spectrum, which enabled us to generate pulses with significantly broader spectral bandwidths. By tuning the interactivity dispersion, we could tune the difference of the repetition rates from 650 Hz to 3 kHz. These values correspond to a maximum non-aliasing bandwidth of around 0.4 THz. These first results were very encouraging, however, the non-aliasing bandwidth needed to be improved in order to enable meaningful spectroscopic measurements. In parallel, we wanted to improve the reproducibility and stability of the mode-locking output, which ultimately led us to investigate the so-called figure-9 laser scheme. We developed, based on the work of Hänsel et al. [57], a very flexible PM figure-9 laser. The laser had a repetition rate of 78 MHz. Our versatile design enabled us to tune many parameters: the interactivity dispersion via the grating separation, the non-reciprocal phase bias, the modulation depth of the saturation behavior of the NALM, and the intra-cavity losses via wave plate tuning.

In **publication 2**, we presented a full characterization of our home-built laser.

We analyzed five representative mode-locking states in terms of RIN, phase noise and free-running CEO frequency noise. We found an operation state operating at a longer wavelengths, i.e. centered around 1075 nm, and close to zero dispersion, which significantly suppressed the pump noise coupling to the laser noise. With this operation state, we achieved a laser RIN of 0.003 % integrated between 1 Hz and 1 MHz and a free-running CEO-frequency linewidth below 10 kHz at 1 s integration time. To the best of our knowledge, these values represent the best performance for free-running NALM-based fiber lasers published to date.

We then proceeded to developed a single-cavity dual-comb based on this new laser design. In **publication 3**, we demonstrated dual-color operation of our all-PM figure-9 laser by implementing our previously developed mechanical spectral filtering technique. With this new laser design, we reached a non-aliasing bandwidth up to 2.4 THz and significantly improved the reliability of the dual-color operation. Subsequently, we generated a dual-comb out of this dual-color laser via amplification and nonlinear wavelength conversion. We demonstrated that the common-mode noise cancellation inside our laser resonator causes the drift of the difference in repetition rate to be one order of magnitude smaller than the drift of the individual repetition rates. The feasibility of performing free-running spectroscopic measurements was demonstrated by measuring the transmission of different etalons.

The laser systems presented in these thesis were based on ytterbium, which makes them ideal light sources for further amplification and nonlinear wavelength conversion due to the power scaling capability of ytterbium.

5.2 Open research questions and outlook

Influence of the transmission function on the laser noise

In publication 2, we analyzed five representative mode-locking states and their noise behavior. By changing the grating separation, we were able to let the laser run in different intracavity dispersion regimes. As demonstrated for other types of mode-locking, we also obtained the lowest noise behavior close to zero dispersion. We furthermore also described in detail how to calculate the transmission function of the cavity as a function of the wave plate angles inside the laser resonator. The calculations show that it is possible to achieve an infinite number of different transmission curves. This flexibility was also the reason why mode-locking could easily be achieved for a large variety of intracavity dispersion values. However, the question of how the transmission function itself influences the noise behavior was

beyond the scope of the paper and still remains open. It would be an interesting study to analyze how the transmission function and the "mode-locking position" on the transmission curve influence the noise behavior of the laser. Edelmann et al. have recently started to investigate how the laser RIN depends on the transmission function [151]. Similar studies should be carried out for the phase noise and CEO noise. With this knowledge, it may be possible to even further decrease the free-running noise of NALM mode-locked fiber lasers.

Cross-correlation timing jitter measurements

The timing jitter measurements presented in publication 2 helped us compare the different operation points with respect to each other. However, the absolute timing jitter values were limited by the chosen measurement method. The noise measured at offset frequencies >10 kHz was dominated by the noise of the measurement setup, i.e. the noise of the photodiode and the internal noise of the signal source analyzer. This limitation can be overcome by using optical methods like optical cross-correlation [131]. This measurement would not only enable a better comparison of the different operation states, but also give a meaningful timing jitter trace at higher offset frequencies.

Cross-phase modulation

In publication 3, we demonstrated that we could separate the cross-phase modulation signal from the center burst by changing the extra-cavity path length difference between the two pulse trains. However, it still remains an open question whether it is possible to get rid of this jamming signal to achieve comb tooth resolution. Different approaches offer the possibility to remove the XPM signal from the time-trace.

Since we can shift the XPM signal with respect to the interferogram, one straightforward way would be to measure two time traces with shifted XPM signals and stitch the time traces together. This would generate a clean time trace without losing any information.

Another approach would be to remove the XPM signal in post-processing. The potential of computational data post-processing to achieved comb tooth resolution in free-running dual-comb spectroscopy has already been demonstrated by Sterczewski et al. [149]. This approach may offer an easy-to-implement method to remove the XPM signal since it does not require any adaptation of the laser setup.

The XPM-signal should also disappear if the two circulating pulses were to only

meet in the free-space section of the laser cavity. Theoretically, this could be the case if the nominal repetition rate is exactly an integer multiple of the difference in repetition rates, since the pulses would then always collide in the same point in space. How to influence the location of this collision point is however a question that we have not addressed yet.

Removing the XPM signal is however an important step to achieve comb-tooth resolution with single-cavity dual-color dual-combs.

Common-mode noise cancellation when locked to a cavity

In publication 3, we showed that the drift of Δf_{rep} is one order of magnitude smaller than the drift of the individual repetition rates. This effect may be exploited when locking the dual-comb to an enhancement cavity. It would be interesting to investigate whether the second combs follows when locking the first comb to a cavity. This intrinsic self-stabilization of the combs with respect to each other could drastically decrease the complexity of cavity-enhanced dual-comb spectroscopy.

5.3 Towards the mid-IR

Many molecules, which are important markers for environmental chemistry, medical applications, and many more research areas, have strong and very characteristic absorption features in the mid-infrared (mid-IR) spectral region [152].

Performing frequency comb spectroscopy on gases in the mid-IR region is a challenging task. In order to achieve broad spectral coverage and sufficient power, mid-IR OFCs can be generated by a multi-stage system comprising a near-IR seed laser, a power amplification and subsequently a nonlinear frequency conversion stage such as difference frequency generation or an optical parametric oscillator. For experiments requiring high (i.e. comb-tooth) resolution, these complex multi-stage setups set the highest demands on the individual steps and the overall stabilization. In particular, it is crucial for the seed laser system to already provide high passive stability. Hence, the knowledge acquired during this thesis work has enabled us to develop a customized and noise-optimized seed laser for such future endeavours.

Bibliography

[1] J. Fellinger, G. Winkler, A. S. Mayer, L. R. Steidle, and O. H. Heckl, "Tunable dual-color operation of Yb:fiber laser via mechanical spectral subdivision", *Optics Express*, vol. 27, no. 4, pp. 5478–5486, 2019. DOI: 10.1364/oe.27.005478.

[2] A. S. Mayer, W. Grosinger, J. Fellinger, G. Winkler, L. Perner, S. Droste, H. Salman, C. Li, C. Heyl, I. Hartl, and O. Heckl, "Flexible all-PM NALM Yb:fiber laser design for frequency comb applications: operation regimes and their noise properties", *Optics Express*, vol. 28, no. 13, pp. 18 946–18 968, 2020, ISSN: 1094-4087. DOI: 10.1364/oe.394543. arXiv: 2004.02852.

[3] J. Fellinger, A. S. Mayer, G. Winkler, W. Grosinger, G.-W. Truong, S. Droste, C. Li, C. M. Heyl, I. Hartl, and O. H. Heckl, "Tunable dual-comb from an all-polarization-maintaining single-cavity dual-color Yb:fiber laser", *Optics Express*, vol. 27, no. 20, pp. 28 062–28 074, 2019, ISSN: 10944087. DOI: 10.1364/OE.27.028062.

[4] H. R. Telle, G. Steinmeyer, A. E. Dunlop, J. Stenger, D. H. Sutter, and U. Keller, "Carrier-envelope offset phase control: A novel concept for absolute optical frequency measurement and ultrashort pulse generation", *Applied Physics B: Lasers and Optics*, vol. 69, no. 4, pp. 327–332, 1999, ISSN: 09462171. DOI: 10.1007/s003400050813.

[5] S. A. Diddams, D. J. Jones, J. Ye, S. T. Cundiff, J. L. Hall, J. K. Ranka, R. S. Windeler, R. Holzwarth, T. Udem, and T. W. Hänsch, "Direct link between microwave and optical frequencies with a 300 THz femtosecond laser comb", *Physical Review Letters*, vol. 84, no. 22, pp. 5102–5105, 2000, ISSN: 10797114. DOI: 10.1103/PhysRevLett.84.5102.

[6] T. Fortier and E. Baumann, "20 Years of Developments in Optical Frequency Comb Technology and Applications", *Communications Physics*, vol. 2, no. 1, pp. 1–16, 2019, ISSN: 23993650. DOI: 10.1038/s42005-019-0249-y. arXiv: 1909.05384.

[7] N. Picqué and T. W. Hänsch, "Frequency comb spectroscopy", *Nature Photonics*, vol. 13, no. 3, pp. 146–157, 2019, ISSN: 1749-4885. DOI: 10.1038/s41566-018-0347-5.

[8] G.-W. Truong, E. M. Waxman, K. C. Cossel, E. Baumann, A. Klose, F. R. Giorgetta, W. C. Swann, N. R. Newbury, and I. Coddington, "Accurate frequency referencing for fieldable dual-comb spectroscopy", *Optics Express*, no. 26, p. 30 495, ISSN: 1094-4087. DOI: 10.1364/oe.24.030495.

[9] M. Lezius, T. Wilken, C. Deutsch, *et al.*, "Space-borne frequency comb metrology", *Optica*, vol. 3, no. 12, p. 1381, 2016, ISSN: 2334-2536. DOI: 10.1364/OPTICA.3.001381.

[10] J. Bates, "Fourier transform infrared spectroscopy", *Science*, vol. 191, no. 4222, pp. 31–37, 1976, ISSN: 0036-8075. DOI: 10.1126/science.1246596.

[11] M. Shirasaki, "Large angular dispersion by a virtually imaged phased array and its application to a wavelength demultiplexer", *Optics Letters*, vol. 21, no. 5, pp. 366–368, 1996, ISSN: 0146-9592. DOI: 10.1364/ol.21.000366. eprint: 0706.1582.

[12] A. Foltynowicz, P. Masłowski, T. Ban, F. Adler, K. C. Cossel, T. C. Briles, and J. Ye, "Optical frequency comb spectroscopy", *Faraday Discussions*, vol. 150, p. 23, 2011, ISSN: 1359-6640. DOI: 10.1039/c1fd00005e.

[13] P. Maslowski, K. F. Lee, A. C. Johansson, A. Khodabakhsh, G. Kowzan, L. Rutkowski, A. A. Mills, C. Mohr, J. Jiang, M. E. Fermann, and A. Foltynowicz, "Surpassing the path-limited resolution of Fourier-transform spectrometry with frequency combs", *Physical Review A*, vol. 93, no. 2, p. 021 802, 2016, ISSN: 2469-9926. DOI: 10.1103/PhysRevA.93.021802. arXiv: 1505.07706.

[14] T. Ideguchi, "Dual-comb spectroscopy", *Optics & Photonics News*, vol. 28, no. 1, pp. 32–39, 2017. DOI: 10.1364/OPN.28.1.000032.

[15] I. Coddington, N. Newbury, and W. Swann, "Dual-comb spectroscopy", *Optica*, vol. 3, no. 4, pp. 414–426, 2016, ISSN: 2334-2536. DOI: 10.1364/optica.3.000414.

[16] T. Ideguchi, T. Nakamura, Y. Kobayashi, and K. Goda, "Kerr-lens mode-locked bidirectional dual-comb ring laser for broadband dual-comb spectroscopy", *Optica*, vol. 3, no. 7, pp. 748–753, 2016, ISSN: 2334-2536. DOI: 10.1364/optica.3.000748.

[17] X. Zhao, G. Hu, B. Zhao, C. Li, Y. Pan, Y. Liu, T. Yasui, and Z. Zheng, "Picometer-resolution dual-comb spectroscopy with a free-running fibre laser", *Optics Express*, vol. 24, no. 19, pp. 21 833–21 845, 2016, ISSN: 1094-4087. DOI: 10.1364/OE.24.021833. arXiv: 1602.07788.

[18] S. M. Link, D. J. H. C. Maas, D. Waldburger, and U. Keller, "Dual-comb spectroscopy of water vapor with a free-running semiconductor disk laser", *Science*, vol. 356, no. 6343, pp. 1164–1168, 2017, ISSN: 0036-8075. DOI: 10.1126/science.aam7424.

[19] J. Chen, X. Zhao, Z. Yao, T. Li, Q. Li, S. Xie, J. Liu, and Z. Zheng, "Dual-comb spectroscopy of methane based on a free-running Erbium-doped fiber laser", *Optics Express*, vol. 27, no. 8, p. 11 406, 2019, ISSN: 1094-4087. DOI: 10.1364/OE.27.011406.

[20] W. Sellmeier, "Ueber die durch die aetherschwingungen erregten mitschwingungen der körpertheilchen und deren rückwirkung auf die ersteren, besonders zur erklärung der dispersion und ihrer anomalien (ii. theil)", *Annalen der Physik und Chemie*, vol. 11, pp. 386–403, 1872, ISSN: 223. DOI: 10.1002/andp.18722231105.

[21] I. H. Malitson, "Interspecimen Comparison of the Refractive Index of Fused Silica*,â ", *Journal of the Optical Society of America*, vol. 55, no. 10, p. 1205, 1965, ISSN: 0030-3941. DOI: 10.1364/josa.55.001205.

[22] R. Paschotta, *Birefringence*. [Online]. Available: https://www.rp-photonics.com/birefringence.html (visited on 11/09/2019).

[23] R. Paschotta, *Waveplates*. [Online]. Available: https://www.rp-photonics.com/waveplates.html (visited on 06/11/2020).

[24] R. Paschotta, *Polarization-maintaining fibers*. [Online]. Available: https://www.rp-photonics.com/polarization_maintaining_fibers.html (visited on 06/11/2020).

[25] G. Agrawal, "Chapter 1 - introduction", in *Nonlinear Fiber Optics (Fifth Edition)*, ser. Optics and Photonics, G. Agrawal, Ed., Fifth Edition, Boston: Academic Press, 2013, pp. 1 –25. DOI: https://doi.org/10.1016/B978-0-12-397023-7.00001-2.

[26] R. Paschotta, *Phase matching*. [Online]. Available: https://www.rp-photonics.com/phase_matching.html (visited on 11/09/2019).

[27] R. W. Boyd, *Nonlinear Optics, Third Edition*, 3rd. USA: Academic Press, Inc., 2008, ISBN: 0123694701.

[28] R. Paschotta, *Chromatic dispersion*. [Online]. Available: https://www.rp-photonics.com/chirped_pulse_amplification.html (visited on 07/21/2019).

[29] R. Paschotta, *Gaussian beams*. [Online]. Available: https://www.rp-photonics.com/gaussian_beams.html (visited on 11/11/2019).

[30] R. Paschotta, *Photonic crystal fibers*. [Online]. Available: https://www.rp-photonics.com/photonic_crystal_fibers.html (visited on 11/10/2019).

[31] E. B. Treacy, "Optical Pulse Compression with Diffraction Gratings", *IEEE Journal of Quantum Electronics*, vol. 5, no. 9, pp. 454–458, 1969, ISSN: 15581713. DOI: 10.1109/JQE.1969.1076303.

[32] H. A. Haus, J. G. Fujimoto, and E. P. Ippen, "Structures for additive pulse mode locking", *J. Opt. Soc. Am. B*, vol. 8, no. 10, pp. 2068–2076, 1991. DOI: 10.1364/JOSAB.8.002068.

[33] H. A. Haus, "Theory of Mode Locking with a Slow Saturable Absorber", *IEEE Journal of Quantum Electronics*, vol. 11, no. 9, pp. 736–746, 1975, ISSN: 15581713. DOI: 10.1109/JQE.1975.1068922.

[34] F. X. Kärtner, U. Morgner, T. Schibli, R. Ell, H. A. Haus, J. G. Fujimoto, and E. P. Ippen, "Few-Cycle Pulses Directly from a Laser", in, vol. 136, 2004, pp. 73–136. DOI: 10.1007/978-3-540-39849-3_2.

[35] H. A. Haus, "Mode-locking of lasers", *IEEE Journal of Selected Topics in Quantum Electronics*, vol. 6, no. 6, pp. 1173–1185, 2000. DOI: 10.1109/2944.902165.

[36] R. Paschotta, *Mode locking*. [Online]. Available: https://www.rp-photonics.com/mode_locking.html (visited on 10/10/2019).

[37] C. M. Eigenwillig, W. Wieser, S. Todor, B. R. Biedermann, T. Klein, C. Jirauschek, and R. Huber, "Picosecond pulses from wavelength-swept continuous-wave Fourier domain mode-locked lasers", *Nature Communications*, vol. 4, no. May, 2013, ISSN: 20411723. DOI: 10.1038/ncomms2870.

[38] H. A. Haus, "Theory of Mode Locking with a Slow Saturable Absorber", *IEEE Journal of Quantum Electronics*, vol. 11, no. 9, pp. 736–746, 1975, ISSN: 15581713. DOI: 10.1109/JQE.1975.1068922.

[39] H. A. Haus, J. G. Fujimoto, and E. P. Ippen, "Structures for additive pulse mode locking", *Journal of the Optical Society of America B*, vol. 8, no. 10, p. 2068, 1991, ISSN: 0740-3224. DOI: 10.1364/JOSAB.8.002068.

[40] H. A. Haus and A. Mecozzi, "Noise of mode-locked lasers", *IEEE Journal of Quantum Electronics*, vol. 29, no. 3, pp. 983–996, 1993. DOI: 10.1109/3.206583.

[41] L. A. Jiang, M. E. Grein, H. A. Haus, and E. P. Ippen, "Noise of mode-locked semiconductor lasers", *IEEE Journal on Selected Topics in Quantum Electronics*, vol. 7, no. 2, pp. 159–167, 2001, ISSN: 1077260X. DOI: 10.1109/2944.954125.

[42] G. P. Agrawal, "Nonlinear fiber optics", in *Nonlinear Science at the Dawn of the 21st Century*, P. L. Christiansen, M. P. Sørensen, and A. C. Scott, Eds., Berlin, Heidelberg: Springer Berlin Heidelberg, 2000, pp. 195–211, ISBN: 978-3-540-46629-1.

[43] J. Kim and Y. Song, "Ultralow-noise mode-locked fiber lasers and frequency combs: principles, status, and applications", *Advances in Optics and Photonics*, vol. 8, no. 3, p. 465, 2016, ISSN: 1943-8206. DOI: 10.1364/aop.8.000465.

[44] J. Kim and Y. Song, "Ultralow-noise mode-locked fiber lasers and frequency combs: principles, status, and applications", *Advances in Optics and Photonics*, vol. 8, no. 3, p. 465, 2016, ISSN: 1943-8206. DOI: 10.1364/aop.8.000465.

[45] F. Ö Ilday, J. R. Buckley, W. G. Clark, and F. W. Wise, "Self-similar evolution of parabolic pulses in a laser", *Physical Review Letters*, vol. 92, no. 21, pp. 213 902–1, 2004, ISSN: 00319007. DOI: 10.1103/PhysRevLett.92.213902. arXiv: 0402013 [physics].

[46] P. Grelu and N. Akhmediev, "Dissipative solitons for mode-locked lasers", *Nature Photonics*, vol. 6, no. 2, pp. 84–92, 2012, ISSN: 1749-4885. DOI: 10.1038/nphoton.2011.345.

[47] U. Keller, K. J. Weingarten, F. X. Kärtner, D. Kopf, B. Braun, I. D. Jung, R. Fluck, C. Hönninger, N. Matuschek, and J. Aus Der Au, "Semiconductor saturable absorber mirrors (SESAM's) for femtosecond to nanosecond pulse generation in solid-state lasers", *IEEE Journal on Selected Topics in Quantum Electronics*, vol. 2, no. 3, pp. 435–451, 1996, ISSN: 1077260X. DOI: 10.1109/2944.571743.

[48] O. Okhotnikov, A. Grudinin, and M. Pessa, "Ultra-fast fibre laser systems based on SESAM technology: new horizons and applications", *New Journal of Physics*, vol. 6, pp. 177–177, 2004, ISSN: 1367-2630. DOI: 10.1088/1367-2630/6/1/177.

[49] M. Hofer, M. E. Fermann, F. Haberl, M. H. Ober, and A. J. Schmidt, "Mode locking with cross-phase and self-phase modulation", *Optics Letters*, vol. 16, no. 7, pp. 502–504, 1991, ISSN: 0146-9592. DOI: 10.1364/ol.16.000502.

[50] V. Matsas, T. Newson, D. Richardson, and D. Payne, "Self-starting, passively mode-locked fibre ring soliton laser exploiting non-linear polarisation rotation", *Electronics Letters*, vol. 28, no. 15, pp. 1391–1393, 1992. DOI: 10.1049/el:19920885.

[51] K. Tamura, H. Haus, and E. Ippen, "Self-starting additive pulse modelocked erbium fibre ring laser", *Electronics Letters*, vol. 28, no. 24, p. 2226, 1992, ISSN: 00135194. DOI: 10.1049/el:19921430.

[52] N. J. Doran and D. Wood, "Nonlinear-optical loop mirror", *Optics Letters*, vol. 13, no. 1, p. 56, 1988, ISSN: 0146-9592. DOI: 10.1364/OL.13.000056.

[53] M. E. Fermann, F. Haberl, M. Hofer, and H. Hochreiter, "Nonlinear amplifying loop mirror", *Optics Letters*, vol. 15, no. 13, p. 752, 1990, ISSN: 0146-9592. DOI: 10.1364/ol.15.000752.

[54] I. Duling, "Subpicosecond all-fibre erbium laser", *Electronics Letters*, vol. 27, no. 6, p. 544, 1991, ISSN: 00135194. DOI: 10.1049/el:19910342.

[55] H. Lin, D. Donald, and W. Sorin, "Optimizing polarization states in a figure-8 laser using a nonreciprocal phase shifter", *Journal of Lightwave Technology*, vol. 12, no. 7, pp. 1121–1128, 1994, ISSN: 07338724. DOI: 10.1109/50.301803.

[56] N. Kuse, J. Jiang, C.-C. Lee, T. R. Schibli, and M. Fermann, "All polarization-maintaining Er fiber-based optical frequency combs with nonlinear amplifying loop mirror", *Optics Express*, vol. 24, no. 3, p. 3095, 2016, ISSN: 1094-4087. DOI: 10.1364/OE.24.003095.

[57] W. Hänsel, H. Hoogland, M. Giunta, S. Schmid, T. Steinmetz, R. Doubek, P. Mayer, S. Dobner, C. Cleff, M. Fischer, and R. Holzwarth, "All polarization-maintaining fiber laser architecture for robust femtosecond pulse generation", *Applied Physics B*, vol. 123, p. 41, 2017, ISSN: 09462171. DOI: 10.1007/978-3-319-64346-5_18.

[58] R. Paschotta, *Frequency combs.* [Online]. Available: https://www.rp-photonics.com/frequency_combs.html (visited on 11/11/2019).

[59] A. Mayer, *Leveraging Novel Nonlinear Devices for Compact Gigahertz Frequency Combs*. 2018. DOI: https://doi.org/10.3929/ethz-b-000252745.

[60] N. R. Newbury and W. C. Swann, "Low-noise fiber-laser frequency combs (Invited)", *Journal of the Optical Society of America B*, vol. 24, no. 8, p. 1756, 2007, ISSN: 0740-3224. DOI: 10.1364/JOSAB.24.001756.

[61] S. Cundiff, T. Fortier, J. Ye, and J. Hall, "Carrier-envelope phase stabilization of femtosecond modelocked lasers and direct optical frequency synthesis", in *Technical Digest. Summaries of papers presented at the Conference on Lasers and Electro-Optics. Postconference Technical Digest (IEEE Cat. No.01CH37170)*, vol. 288, IEEE, 2001, p. 130, ISBN: 1-55752-662-1. DOI: 10.1109/CLEO.2001.947591.

[62] A. Klenner, S. Schilt, T. Südmeyer, and U. Keller, "Gigahertz frequency comb from a diode-pumped solid-state laser", *Optics Express*, vol. 22, no. 25, p. 31 008, 2014, ISSN: 1094-4087. DOI: 10.1364/oe.22.031008.

[63] M. E. Fermann and I. Hartl, "Ultrafast fibre lasers", *Nature Photonics*, vol. 7, no. 11, pp. 868–874, 2013, ISSN: 17494885. DOI: 10.1038/nphoton.2013.280.

[64] G.-W. Truong, E. M. Waxman, K. C. Cossel, E. Baumann, A. Klose, F. R. Giorgetta, W. C. Swann, N. R. Newbury, and I. Coddington, "Accurate frequency referencing for fieldable dual-comb spectroscopy", *Optics Express*, vol. 24, no. 26, pp. 30 495–30 504, 2016, ISSN: 1094-4087. DOI: 10.1364/oe.24.030495.

[65] P. Giaccari, J.-D. Deschênes, P. Saucier, J. Genest, and P. Tremblay, "Active Fourier-transform spectroscopy combining the direct RF beating of two fiber-based mode-locked lasers with a novel referencing method", *Optics Express*, vol. 16, no. 6, p. 4347, 2008, ISSN: 1094-4087. DOI: 10.1364/OE.16.004347.

[66] T. Ideguchi, A. Poisson, G. Guelachvili, T. W. Hänsch, and N. Picqué, "Adaptive dual-comb spectroscopy in the green region", *Optics Letters*, vol. 37, no. 23, pp. 4847–4849, 2012, ISSN: 0146-9592. DOI: 10.1364/ol.37.004847. arXiv: 2012arXiv1208.4454I.

[67] T. Ideguchi, A. Poisson, G. Guelachvili, N. Picqué, and T. W. Hänsch, "Adaptive real-time dual-comb spectroscopy", *Nature communications*, vol. 5, p. 3375, 2014, ISSN: 20411723. DOI: 10.1038/ncomms4375. arXiv: 1201.4177.

[68] M. Cassinerio, A. Gambetta, N. Coluccelli, P. Laporta, and G. Galzerano, "Absolute dual-comb spectroscopy at 1.55 μm by free-running Er:fiber lasers", *Applied Physics Letters*, vol. 104, no. 23, p. 231 102, 2014, ISSN: 00036951. DOI: 10.1063/1.4882862.

[69] S. M. Link, A. Klenner, M. Mangold, C. A. Zaugg, M. Golling, B. W. Tilma, and U. Keller, "Dual-comb modelocked laser", *Optics Express*, vol. 23, no. 5, p. 5521, 2015, ISSN: 1094-4087. DOI: 10.1364/OE.23.005521.

[70] I. Znakovskaya, E. Fill, N. Forget, P. Tournois, M. Seidel, O. Pronin, F. Krausz, and A. Apolonski, "Dual frequency comb spectroscopy with a single laser", *Optics Letters*, vol. 39, no. 19, p. 5471, 2014, ISSN: 0146-9592. DOI: 10.1364/OL.39.005471.

[71] A. E. Akosman and M. Y. Sander, "Dual comb generation from a mode-locked fiber laser with orthogonally polarized interlaced pulses", *Optics Express*, vol. 25, no. 16, p. 18 592, 2017, ISSN: 1094-4087. DOI: 10.1364/OE.25.018592.

[72] Y. Nakajima, Y. Hata, and K. Minoshima, "All-Polarization-Maintaining Dual-Comb Fiber Laser with Nonlinear Amplifying Loop Mirror", *Conference on Lasers and Electro-Optics*, vol. 1, STu4K.4, 2018. DOI: 10.1364/cleo_si.2018.stu4k.4.

[73] R. Liao, Y. Song, W. Liu, H. Shi, L. Chai, and M. Hu, "Dual-comb spectroscopy with a single free-running thulium-doped fiber laser", *Optics Express*, vol. 26, no. 8, p. 11 046, 2018, ISSN: 1094-4087. DOI: 10.1364/OE.26.011046.

[74] R. Wang, X. Zhao, W. Bai, J. Chen, Y. Pan, and Z. Zheng, "Polarization-maintaining, dual-wavelength, dual-comb mode-locked fiber laser", in *Conference on Lasers and Electro-Optics*, Washington, D.C.: OSA, 2018, JTh2A.139, ISBN: 978-1-943580-42-2. DOI: 10.1364/CLEO_AT.2018.JTh2A.139.

[75] M. Margalit, M. Orenstein, and G. Eisenstein, "Synchronized two-color operation of a passively mode-locked erbium-doped fiber laser by dual injection locking", *Opt. Lett.*, vol. 21, no. 19, pp. 1585–1587, 1996. DOI: 10.1364/OL.21.001585.

[76] H. Zhang, D. Y. Tang, X. Wu, and L. M. Zhao, "Multi-wavelength dissipative soliton operation of an erbium-doped fiber laser", *Optics Express*, vol. 17, no. 15, pp. 12 692–12 697, 2009, ISSN: 1094-4087. DOI: 10.1364/oe.17.012692. eprint: 0907.1782.

[77] X. Zhao, Z. Zheng, L. Liu, Y. Liu, Y. Jiang, X. Yang, and J. Zhu, "Switchable, dual-wavelength passively mode-locked ultrafast fiber laser based on a single-wall carbon nanotube modelocker and intracavity loss tuning", *Optics Express*, vol. 19, no. 2, pp. 1168–1173, 2011, ISSN: 1094-4087. DOI: 10.1364/oe.19.001168.

[78] L. Yun, X. Liu, and D. Mao, "Observation of dual-wavelength dissipative solitons in a figure-eight erbium-doped fiber laser", *Optics Express*, vol. 20, no. 19, p. 20 992, 2012, ISSN: 1094-4087. DOI: 10.1364/OE.20.020992.

[79] R. Li, H. Shi, H. Tian, Y. Li, B. Liu, Y. Song, and M. Hu, "All-polarization-maintaining dual-wavelength mode-locked fiber laser based on Sagnac loop filter", *Optics Express*, vol. 26, no. 22, p. 28 302, 2018, ISSN: 1094-4087. DOI: 10.1364/OE.26.028302.

[80] X. Liu, D. Han, Z. Sun, C. Zeng, H. Lu, D. Mao, Y. Cui, and F. Wang, "Versatile multi-wavelength ultrafast fiber laser mode-locked by carbon nanotubes", *Scientific Reports*, vol. 3, p. 2718, 2013, ISSN: 20452322. DOI: 10.1038/srep02718.

[81] J. M. Evans, D. E. Spence, D. Burns, and W. Sibbett, "Dual-wavelength self-mode-locked ti:sapphire laser", *Opt. Lett.*, vol. 18, no. 13, pp. 1074–1076, 1993. DOI: 10.1364/OL.18.001074.

[82] W. H. Knox, "In situ measurement of complete intracavity dispersion in an operating Ti:sapphire femtosecond laser", *Optics Letters*, vol. 17, no. 7, pp. 514–516, 1992, ISSN: 0146-9592. DOI: 10.1364/ol.17.000514.

[83] A. Chong, L. G. Wright, and F. W. Wise, "Ultrafast fiber lasers based on self-similar pulse evolution: a review of current progress", *Reports on Progress in Physics*, vol. 78, no. 11, p. 113 901, 2015, ISSN: 0034-4885. DOI: 10.1088/0034-4885/78/11/113901.

[84] X. Li, M. A. Reber, C. Corder, Y. Chen, P. Zhao, and T. K. Allison, "High-power ultrafast Yb:fiber laser frequency combs using commercially available components and basic fiber tools", *Review of Scientific Instruments*, vol. 87, no. 9, p. 093 114, 2016, ISSN: 10897623. DOI: 10.1063/1.4962867. arXiv: 1606.05234.

[85] Y. Wei, B. Li, X. Wei, Y. Yu, and K. K. Wong, "Ultrafast spectral dynamics of dual-color-soliton intracavity collision in a mode-locked fiber laser", *Applied Physics Letters*, vol. 112, no. 8, p. 081 104, 2018, ISSN: 00036951. DOI: 10.1063/1.5020821.

[86] Y. Wang, L. Zhang, Z. Zhuo, and S. Guo, "Cross-splicing method for compensating fiber birefringence in polarization-maintaining fiber ring laser mode locked by nonlinear polarization evolution", *Applied Optics*, vol. 55, no. 21, p. 5766, 2016, ISSN: 0003-6935. DOI: 10.1364/AO.55.005766.

[87] J. Szczepanek, T. M. Kardaś, C. Radzewicz, and Y. Stepanenko, "Ultrafast laser mode-locked using nonlinear polarization evolution in polarization maintaining fibers", *Optics Letters*, vol. 42, no. 3, pp. 575–578, 2017. DOI: 10.1364/CLEO_SI-2017-SM2I.5.

[88] J. Szczepanek, T. M. Kardaś, C. Radzewicz, and Y. Stepanenko, "Nonlinear polarization evolution of ultrashort pulses in polarization maintaining fibers", *Optics Express*, vol. 26, no. 10, pp. 13 590–13 604, 2018, ISSN: 1094-4087. DOI: 10.1364/OE.26.013590.

[89] W. Zhang, Y. Liu, C. Wang, Z. Zhu, D. Luo, C. Gu, and W. Li, "Ultrafast PM fiber ring laser mode-locked by nonlinear polarization evolution with short NPE section segments", *Optics Express*, vol. 26, no. 7, p. 7934, 2018, ISSN: 1094-4087. DOI: 10.1364/OE.26.007934.

[90] L. Zhou, Y. Liu, G. Xie, W. Zhang, Z. Zhu, C. Ouyang, C. Gu, and W. Li, "Generation of stretched pulses from an all-polarization-maintaining Er-doped mode-locked fiber laser using nonlinear polarization evolution", *Applied Physics Express*, vol. 12, no. 5, 2019, ISSN: 18820786. DOI: 10.7567/1882-0786/ab15c0.

[91] D. Popa, Z. Sun, F. Torrisi, T. Hasan, F. Wang, and A. C. Ferrari, "Sub 200 fs pulse generation from a graphene mode-locked fiber laser", *Applied Physics Letters*, vol. 97, no. 20, p. 203 106, 2010, ISSN: 0003-6951. DOI: 10.1063/1.3517251. eprint: 1010.1329.

[92] E. J. Lee, S. Y. Choi, H. Jeong, N. H. Park, W. Yim, M. H. Kim, J. K. Park, S. Son, S. Bae, S. J. Kim, K. Lee, Y. H. Ahn, K. J. Ahn, B. H. Hong, J. Y. Park, F. Rotermund, and D. I. Yeom, "Active control of all-fibre graphene devices with electrical gating", *Nature Communications*, vol. 6, pp. 1–6, 2015, ISSN: 20411723. DOI: 10.1038/ncomms7851.

[93] Y.-W. Song, S. Yamashita, C. S. Goh, and S. Y. Set, "Carbon nanotube mode lockers with enhanced nonlinearity via evanescent field interaction in D-shaped fibers", *Optics Letters*, vol. 32, no. 2, p. 148, 2007, ISSN: 0146-9592. DOI: 10.1364/ol.32.000148.

[94] K. Kieu and M. Mansuripur, "Femtosecond laser pulse generation with a fiber taper embedded in carbon nanotube/polymer composite", *Optics Letters*, vol. 32, no. 15, pp. 2242–2244, 2007, ISSN: 0146-9592. DOI: 10.1364/ol.32.002242.

[95] D. Popa, Z. Sun, T. Hasan, W. B. Cho, F. Wang, F. Torrisi, and A. C. Ferrari, "74-fs nanotube-mode-locked fiber laser", *Applied Physics Letters*, vol. 101, no. 15, p. 153 107, 2012, ISSN: 0003-6951. DOI: 10.1063/1.4757293.

[96] J. Sotor, G. Sobon, K. Grodecki, and K. M. Abramski, "Mode-locked erbium-doped fiber laser based on evanescent field interaction with Sb2Te3 topological insulator", *Applied Physics Letters*, vol. 104, no. 25, p. 251 112, 2014, ISSN: 0003-6951. DOI: 10.1063/1.4885371.

[97] J. Lee, J. Koo, Y. M. Jhon, and J. H. Lee, "A femtosecond pulse erbium fiber laser incorporating a saturable absorber based on bulk-structured Bi_2Te_3 topological insulator", *Optics Express*, vol. 22, no. 5, p. 6165, 2014, ISSN: 1094-4087. DOI: 10.1364/OE.22.006165.

[98] I. Duling, "Subpicosecond all-fibre erbium laser", *Electronics Letters*, vol. 27, no. 6, p. 544, 1991, ISSN: 00135194. DOI: 10.1049/el:19910342.

[99] D. J. Richardson, R. I. Laming, D. N. Payne, M. W. Phillips, and V. J. Matsas, "320 fs soliton generation with passively mode-locked erbium fibre laser", *Electronics Letters*, vol. 27, no. 9, p. 730, 1991, ISSN: 00135194. DOI: 10.1049/el:19910454.

[100] J. W. Nicholson and M. Andrejco, "A polarization maintaining, dispersion managed, femtosecond figure-eight fiber laser", *Optics Express*, vol. 14, no. 18, p. 8160, 2006, ISSN: 1094-4087. DOI: 10.1364/OE.14.008160.

[101] E. Baumann, F. R. Giorgetta, J. W. Nicholson, W. C. Swann, I. Coddington, and N. R. Newbury, "High-performance, vibration-immune, fiber-laser frequency comb", *Optics Letters*, vol. 34, no. 5, p. 638, 2009, ISSN: 0146-9592. DOI: 10.1364/OL.34.000638.

[102] J. Szczepanek, T. M. Kardaś, M. Michalska, C. Radzewicz, and Y. Stepanenko, "Simple all-PM-fiber laser mode-locked with a nonlinear loop mirror", *Optics Letters*, vol. 40, no. 15, p. 3500, 2015, ISSN: 0146-9592. DOI: 10.1364/OL.40.003500.

[103] T. Jiang, Y. Cui, P. Lu, C. Li, A. Wang, and Z. Zhang, "All PM Fiber Laser Mode Locked with a Compact Phase Biased Amplifier Loop Mirror", *IEEE Photonics Technology Letters*, vol. 28, no. 16, pp. 1786–1789, 2016, ISSN: 10411135. DOI: 10.1109/LPT.2016.2572167.

[104] D. Kim, D. Kwon, B. Lee, and J. Kim, "Polarization-maintaining nonlinear-amplifying-loop-mirror mode-locked fiber laser based on a 3 x 3 coupler", *Optics Letters*, vol. 44, no. 5, p. 1068, 2019, ISSN: 0146-9592. DOI: 10.1364/OL.44.001068.

[105] R. Liao, Y. Song, L. Chai, and M. Hu, "Pulse dynamics manipulation by the phase bias in a nonlinear fiber amplifying loop mirror", *Optics Express*, vol. 27, no. 10, p. 14 705, 2019, ISSN: 1094-4087. DOI: 10.1364/OE.27.014705.

[106] Z. Guo, Q. Hao, S. Yang, T. Liu, H. Hu, and H. Zeng, "Octave-Spanning Supercontinuum Generation From an NALM Mode-Locked Yb-Fiber Laser System", *IEEE Photonics Journal*, vol. 9, no. 1, pp. 1–7, 2017, ISSN: 1943-0655. DOI: 10.1109/JPHOT.2017.2655003.

[107] G. Liu, X. Jiang, A. Wang, G. Chang, F. Kaertner, and Z. Zhang, "Robust 700 MHz mode-locked Yb:fiber laser with a biased nonlinear amplifying loop mirror", *Optics Express*, vol. 26, no. 20, p. 26 003, 2018, ISSN: 1094-4087. DOI: 10.1364/oe.26.026003.

[108] W. Liu, H. Shi, J. Cui, C. Xie, Y. Song, C. Wang, and M. Hu, "Single-polarization large-mode-area fiber laser mode-locked with a nonlinear amplifying loop mirror", *Optics Letters*, vol. 43, no. 12, p. 2848, 2018, ISSN: 0146-9592. DOI: 10.1364/ol.43.002848.

[109] W. Hänsel, M. Giunta, M. Lezius, M. Fischer, and R. Holzwarth, "Electro-optic modulator for rapid control of the carrier-envelope offset frequency", in *Conference on Lasers and Electro-Optics*, Washington, D.C.: OSA, 2017, SF1C.5, ISBN: 978-1-943580-27-9. DOI: 10.1364/CLEO_SI.2017.SF1C.5.

[110] Y. Li, N. Kuse, A. Rolland, Y. Stepanenko, C. Radzewicz, and M. E. Fermann, "Low noise, self-referenced all polarization maintaining Ytterbium fiber laser frequency comb", *Optics Express*, vol. 25, no. 15, pp. 18 017–18 023, 2017. DOI: 10.1364/OE.25.018017.

[111] S. Salman, Y. Ma, K. Gürel, S. Schilt, C. Li, P. Pfäfflein, C. Mahnke, J. Fellinger, S. Droste, A. S. Mayer, O. H. Heckl, T. Südmeyer, C. M. Heyl, and I. Hartl, "Comparison of two low-noise cep stabilization methods for an environmentally stable yb:fiber oscillator", in *Laser Congress 2019 (ASSL, LAC, LS&C)*, Optical Society of America, 2019, JTu3A.17. DOI: 10.1364/ASSL.2019.JTu3A.17.

[112] M. C. Stumpf, S. Pekarek, A. E. Oehler, T. Südmeyer, J. M. Dudley, and U. Keller, "Self-referencable frequency comb from a 170-fs, 1.5-μm solid-state laser oscillator", *Applied Physics B: Lasers and Optics*, vol. 99, no. 3, pp. 401–408, 2010, ISSN: 09462171. DOI: 10.1007/s00340-009-3854-8.

[113] T. D. Shoji, W. Xie, K. L. Silverman, A. Feldman, T. Harvey, R. P. Mirin, and T. R. Schibli, "Ultra-low-noise monolithic mode-locked solid-state laser", *Optica*, vol. 3, no. 9, p. 995, 2016, ISSN: 2334-2536. DOI: 10.1364/OPTICA.3.000995.

[114] R. C. Jones, "A New Calculus for the Treatment of Optical SystemsI Description and Discussion of the Calculus", *Journal of the Optical Society of America*, vol. 31, no. 7, p. 488, 1941, ISSN: 0030-3941. DOI: 10.1364/JOSA.31.000488.

[115] W. H. Knox, "Dispersion measurements for femtosecond-pulse generation and applications", *Applied Physics B Laser and Optics*, vol. 58, no. 3, pp. 225–235, 1994, ISSN: 0946-2171. DOI: 10.1007/BF01081314.

[116] U. Schlarb and B. Sugg, "Refractive Index of Terbium Gallium Garnet", *physica status solidi (b)*, vol. 182, no. 2, K91–K93, 1994, ISSN: 03701972. DOI: 10.1002/pssb.2221820238.

[117] L. Nugent-Glandorf, T. A. Johnson, Y. Kobayashi, and S. A. Diddams, "Impact of dispersion on amplitude and frequency noise in a Yb-fiber laser comb", *Optics Letters*, vol. 36, no. 9, p. 1578, 2011, ISSN: 0146-9592. DOI: 10.1364/OL.36.001578.

[118] Y. Song, C. Kim, K. Jung, H. Kim, and J. Kim, "Timing jitter optimization of mode-locked Yb-fiber lasers toward the attosecond regime", *Optics Express*, vol. 19, no. 15, p. 14 518, 2011, ISSN: 1094-4087. DOI: 10.1364/OE.19.014518. arXiv: 1101.3613.

[119] S. Novak and A. Moesle, "Analytic model for gain modulation in EDFAs", *Journal of Lightwave Technology*, vol. 20, no. 6, pp. 975–985, 2002, ISSN: 0733-8724. DOI: 10.1109/JLT.2002.1018809.

[120] H. Tünnermann, J. Neumann, D. Kracht, and P. Weßels, "Gain dynamics and refractive index changes in fiber amplifiers: a frequency domain approach", *Optics Express*, vol. 20, no. 12, p. 13 539, 2012, ISSN: 1094-4087. DOI: 10.1364/OE.20.013539.

[121] J. Zhao, G. Guiraud, F. Floissat, B. Gouhier, S. Rota-Rodrigo, N. Traynor, and G. Santarelli, "Gain dynamics of clad-pumped yb-fiber amplifier and intensity noise control", *Opt. Express*, vol. 25, no. 1, pp. 357–366, 2017. DOI: 10.1364/OE.25.000357.

[122] L. Matos, O. D. Mücke, J. Chen, and F. X. Kärtner, "Carrier-envelope phase dynamics and noise analysis in octave-spanning Ti:sapphire lasers", *Optics Express*, vol. 14, no. 6, p. 2497, 2006, ISSN: 1094-4087. DOI: 10.1364/OE.14.002497.

[123] B. R. Washburn, W. C. Swann, and N. R Newbury, "Response dynamics of the frequency comb output from a femtosecond fiber laser", *Optics Express*, vol. 13, no. 26, p. 10 622, 2005, ISSN: 1094-4087. DOI: 10.1364/OPEX.13.010622.

[124] I. L. Budunoglu, C. Ülgüdür, B. Oktem, and F. Ö. Ilday, "Intensity noise of mode-locked fiber lasers", *Optics Letters*, vol. 34, no. 16, p. 2516, 2009, ISSN: 0146-9592. DOI: 10.1364/OL.34.002516.

[125] C. Wan, T. R. Schibli, P. Li, C. Bevilacqua, A. Ruehl, and I. Hartl, "Intensity noise coupling in soliton fiber oscillators", *Optics Letters*, vol. 42, no. 24, p. 5266, 2017, ISSN: 0146-9592. DOI: 10.1364/OL.42.005266.

[126] P. Qin, Y. Song, H. Kim, J. Shin, D. Kwon, M. Hu, C. Wang, and J. Kim, "Reduction of timing jitter and intensity noise in normal-dispersion passively mode-locked fiber lasers by narrow band-pass filtering", *Optics Express*, vol. 22, no. 23, p. 28 276, 2014, ISSN: 1094-4087. DOI: 10.1364/OE.22.028276.

[127] J. Chen, J. W. Sickler, E. P. Ippen, and F. X. Kärtner, "High repetition rate, low jitter, low intensity noise, fundamentally mode-locked 167 fs soliton Er-fiber laser", *Optics Letters*, vol. 32, no. 11, p. 1566, 2007, ISSN: 0146-9592. DOI: 10.1364/OL.32.001566.

[128] T. K. Kim, Y. Song, K. Jung, C. Kim, H. Kim, C. H. Nam, and J. Kim, "Sub-100-as timing jitter optical pulse trains from mode-locked Er-fiber lasers", *Optics Letters*, vol. 36, no. 22, p. 4443, 2011, ISSN: 0146-9592. DOI: 10.1364/OL.36.004443.

[129] K. Jung and J. Kim, "Characterization of timing jitter spectra in free-running mode-locked lasers with 340 dB dynamic range over 10 decades of Fourier frequency", *Optics Letters*, vol. 40, no. 3, p. 316, 2015, ISSN: 0146-9592. DOI: 10.1364/OL.40.000316.

[130] D. Hou, C.-C. Lee, Z. Yang, and T. R. Schibli, "Timing jitter characterization of mode-locked lasers with <1 zs/$\sqrt{\text{Hz}}$ resolution using a simple optical heterodyne technique, volume = 40, year = 2015", *Optics Letters*, no. 13, p. 2985, ISSN: 0146-9592. DOI: 10.1364/OL.40.002985.

[131] L. A. Jiang, S. T. Wong, M. E. Grein, E. P. Ippen, and H. A. Haus, "Measuring timing jitter with optical cross correlations", *IEEE Journal of Quantum Electronics*, vol. 38, no. 8, pp. 1047–1052, 2002, ISSN: 0018-9197. DOI: 10.1109/JQE.2002.800993.

[132] J. Kim, J. Chen, J. Cox, and F. X. Kärtner, "Attosecond-resolution timing jitter characterization of free-running mode-locked lasers", *Optics Letters*, vol. 32, no. 24, p. 3519, 2007, ISSN: 0146-9592. DOI: 10.1364/OL.32.003519.

[133] R. Paschotta, "Noise of mode-locked lasers (Part II): timing jitter and other fluctuations", *Applied Physics B*, vol. 79, no. 2, pp. 163–173, 2004, ISSN: 0946-2171. DOI: 10.1007/s00340-004-1548-9.

[134] J. P. Gordon, "Theory of the soliton self-frequency shift", *Optics Letters*, vol. 11, no. 10, p. 662, 1986, ISSN: 0146-9592. DOI: 10.1364/ol.11.000662.

[135] S. Namiki and H. A. Haus, "Noise of the stretched pulse fiber laser. I. Theory", *IEEE Journal of Quantum Electronics*, vol. 33, no. 5, pp. 649–659, 1997, ISSN: 00189197. DOI: 10.1109/3.572138.

[136] D. G. Matei, T. Legero, S. Häfner, C. Grebing, R. Weyrich, W. Zhang, L. Sonderhouse, J. M. Robinson, J. Ye, F. Riehle, and U. Sterr, "1.5 μm Lasers with sub 10 mHz Linewidth", *Physical Review Letters*, vol. 118, no. 26, p. 263 202, 2017, ISSN: 0031-9007. DOI: https://doi.org/10.1103/PhysRevLett.118.263202.

[137] J. L. Hall and M. Zhu, "An introduction to phase-stable optical sources", *Laser Manipulation of Atoms and Ions: Proceedings of the International School of Physics: Enrico Fermi Course 118, E. Arimondo, W. D. Phillips, and F. Strumia, eds. (Elsevier Science Publishers B.V., 1992)*, pp. 671–702,

[138] G. Di Domenico, S. Schilt, and P. Thomann, "Simple approach to the relation between laser frequency noise and laser line shape", *Applied Optics*, vol. 49, no. 25, p. 4801, 2010, ISSN: 0003-6935. DOI: 10.1364/AO.49.004801.

[139] J. J. McFerran, W. C. Swann, B. R. Washburn, and N. R. Newbury, "Suppression of pump-induced frequency noise in fiber-laser frequency combs leading to sub-radian f ceo phase excursions", *Applied Physics B*, vol. 86, no. 2, pp. 219–227, 2007, ISSN: 0946-2171. DOI: 10.1007/s00340-006-2426-4.

[140] N. Bucalovic, V. Dolgovskiy, C. Schori, P. Thomann, G. Di Domenico, and S. Schilt, "Experimental validation of a simple approximation to determine the linewidth of a laser from its frequency noise spectrum", *Applied Optics*, vol. 51, no. 20, p. 4582, 2012, ISSN: 1559-128X. DOI: 10.1364/AO.51.004582.

[141] N. Abdukerim, M. I. Kayes, A. Rekik, and M. Rochette, "Bidirectional mode-locked thulium-doped fiber laser", *Applied Optics*, vol. 57, no. 25, p. 7198, 2018, ISSN: 1559-128X. DOI: 10.1364/AO.57.007198.

[142] Y. Nakajima, Y. Hata, and K. Minoshima, "All-polarization-maintaining, polarization-multiplexed, dual-comb fiber laser with a nonlinear amplifying loop mirror", *Optics Express*, vol. 27, no. 10, pp. 14 648–14 656, 2019. DOI: 10.1364/oe.27.014648.

[143] J. Nürnberg, C. G. E. Alfieri, Z. Chen, D. Waldburger, N. Picqué, and U. Keller, "An unstabilized femtosecond semiconductor laser for dual-comb spectroscopy of acetylene", *Optics Express*, vol. 27, no. 3, p. 3190, 2019, ISSN: 1094-4087. DOI: 10.1364/OE.27.003190.

[144] X. Luo, T. H. Tuan, T. S. Saini, H. P. T. Nguyen, T. Suzuki, and Y. Ohishi, "Tunable and switchable all-fiber dual-wavelength mode locked laser based on Lyot filtering effect", *Optics Express*, vol. 27, no. 10, pp. 14 635–14 647, 2019, ISSN: 1094-4087. DOI: 10.1364/OE.27.014635.

[145] E. Baumann, E. V. Hoenig, E. F. Perez, G. M. Colacion, F. R. Giorgetta, K. C. Cossel, G. Ycas, D. R. Carlson, D. D. Hickstein, K. Srinivasan, S. B. Papp, N. R. Newbury, and I. Coddington, "Dual-comb spectroscopy with tailored spectral broadening in Si 3 N 4 nanophotonics", *Optics Express*, vol. 27, no. 8, p. 11 869, 2019, ISSN: 1094-4087. DOI: 10.1364/OE.27.011869. arXiv: 1811.05906.

[146] N. R. Newbury, I. Coddington, and W. Swann, "Sensitivity of coherent dual-comb spectroscopy", *Optics Express*, vol. 18, no. 8, p. 7929, 2010. DOI: 10.1364/oe.18.007929.

[147] T. Skauli, P. S. Kuo, K. L. Vodopyanov, T. J. Pinguet, O. Levi, L. A. Eyres, J. S. Harris, M. M. Fejer, B. Gerard, L. Becouarn, and E. Lallier, "Improved dispersion relations for GaAs and applications to nonlinear optics", *Journal of Applied Physics*, vol. 94, no. 10, pp. 6447–6455, 2003, ISSN: 0021-8979. DOI: 10.1063/1.1621740.

[148] M. Querry, "Optical Constants of Minerals and Other Materials from the Millimeter to the Ultraviolet", *Contract. Rep.*, p. 71, 1987.

[149] Ł. A. Sterczewski, A. Przewłoka, and W. Kaszub, "Computational Doppler-limited dual-comb spectroscopy with a free-running all-fiber laser", *arXiv:1905.04647 [physics.ins-det]*, pp. 1–15, 2019.

[150] G. Soboń, T. Martynkien, P. Mergo, L. Rutkowski, and A. Foltynowicz, "High-power frequency comb source tunable from 2.7 to 4.2 μm based on difference frequency generation pumped by an Yb-doped fiber laser", *Optics Letters*, vol. 42, no. 9, pp. 1748–1751, 2017. DOI: 10.1364/OL.42.001748.

[151] M. Edelmann, Y. Hua, K. Åžafak, and F. X. Kärtner, "Amplitude-noise Suppressing Mechanism in Fiber Lasers Mode-locked with Nonlinear Amplifying Loop Mirror", pp. 1–4, 2020. arXiv: 2010.13824.

[152] K. C. Cossel, E. M. Waxman, I. A. Finneran, G. A. Blake, J. Ye, and N. R. Newbury, "Gas-phase broadband spectroscopy using active sources: progress, status, and applications [Invited]", *Journal of the Optical Society of America B*, vol. 34, no. 1, p. 104, 2017, ISSN: 0740-3224. DOI: 10.1364/JOSAB.34.000104.

List of abbreviations

ASE amplified spontaneous emission 81
CEO carrier-envelope-offset 62
CW continuous-wave 9
DESY German Electron Synchrotron 61
DC dual-comb 2
FTS Fourier transform spectrometer 41
FWHM full width at half maximum 9
GDD group delay dispersion 11
HWP half-wave plate 52
mid-IR mid-infrared 125
NALM nonlinear amplifying loop mirror 27
NOLM nonlinear loop mirror 26
NPR nonlinear polarization rotation 25
OFC optical frequency comb 1
PBS polarization beam splitter cube 52
PCF photonic crystal fiber 14
PM polarization-maintaining 5
PPLN periodically poled lithium niobate 83
PSD power spectral densitie 80
QWP quarter-waveplate 52
rbw resolution bandwidth 55
RF radio frequency 50
RIN relative intensity noise xii
rms root-mean-square 80
SESAM semiconductor saturable absorber mirror 24
SMF single mode fiber 52
SNR signal-to-noise 83

SPM self-phase modulation 8

SSB single-side band 81

TOD third-order dispersion 11

WDM wavelength division multiplexer 52

XPM cross-phase modulation 8

Yb ytterbium 51

List of Figures

List of Tables

Acknowledgements

"It's a dangerous business, Frodo, going out your door. You step onto the road, and if you don't keep your feet, there's no knowing where you might be swept off to."

Gandalf the Gray, The Lord of the Rings

Step by step, it has been a very long journey so far. When I look back at all the obstacles I have overcome, I often wonder how that was possible. The answer to this question is: with a lot of help and support. Therefore, I would like to thank all those who have accompanied me through my life, moreover carried and sometimes dragged me through.

I would like to thank Oliver Heckl, who he gave me the chance to become a member of his group as a Ph.D. student and for putting all the trust and support into me. The path from an empty space without a floor to the functional laboratory, which publishes Q1 publications was exhausting and challenging but, above all, instructive. Dear Oliver, thank you for giving me the chance to be part of that journey.

At this point, I would like to thank Georg Winkler in particular. Thank you for introducing me to the world of laser physics and for looking after me with such a pleasant, courteous manner and overwhelming competence during my master's thesis. Thank you for all your efforts and the time you have spent with me.

Many thanks to the colleagues from DESY, Stefan Droste, Chen Li, Sarper Salman, Christoph Heyl, Ingmar Hartl; it was a pleasure to work with you. And of course, thanks to the entire team of the Christian Doppler Laboratory and the Faculty Center for Nanostructure Research.

I particularly would like to thank Aline Mayer for supporting my strengths and helping me to overcome my weaknesses. Thank you for sharing your superpower: "writing" with me. Thank you for your feedback and support on my thesis. It was a pleasure to discuss my thesis with you, and thank you for sharing your competence and achievements in the field with me.

Many thanks to Andreas, Philip, and Lukas for accompanying me throughout my studies. Thank you, Thomas, for being not only the best electron of all time but for the numerous help during my studies that you simply take for granted.

Many thanks to Johannes; you have been a driving force for me during my studies, and thank you for all the skiing turns we shared. Please excuse me for

making you have to go to the hospital that one time.

Thank you, Willi, for sharing plenty of climbing journeys with me, which prevented me from going crazy, and thank you for always having an open ear for me.

And there was Max! I will never forget the first beers we shared in our first lecture. Thank you for all the inspiring discussions about physics at the Karls-Brunnen. Thank you for pushing me through my bachelor and master studies, and most of all, thank you for having my back all these years.

My deepest gratitude, of course, belongs to my family, my parents Elisabeth and Franz, and my brother Daniel. Thank you for protecting and supporting me and forming my unbreakable safety net for all these years.

Many thanks to Manfred, Michaela, Marina, Oma, and Opa Berthold for welcoming me so warmly into your family; it is a great enrichment to have you in my life.

Finally, I would like to thank the love of my life, Melanie. Thank you for keeping the Hulk under control! There are no words to express how happy and thankful I am for having you in my life. I am looking forward to all the journeys to come with you.